

Grassy-ELM^(a) regime with edge resonant magnetic perturbations in fully noninductive plasmas in the DIII-D tokamak

R. Nazikian¹, C.C. Petty², A. Bortolon¹, Xi Chen², D. Eldon², T.E. Evans², B.A. Grierson¹, N.M. Ferraro¹, S.R. Haskey¹, M. Knolker³, C. Lasnier⁵, N.C. Logan¹, R.A. Moyer⁶, D. Orlov⁶, T.H. Osborne², C. Paz-Soldan², F. Turco⁷, H.Q. Wang⁸, D.B. Weisberg²

¹ Princeton Plasma Physics Laboratory, Princeton NJ 08543-0451, USA

² General Atomics, PO Box 85608, San Diego, CA 92186-5608, USA

³ Ludwig Maximilians Universitaet, München, Germany

⁴ Mechanical and Aerospace Engineering, Princeton University, Princeton NJ 08540, USA

⁵ Lawrence Livermore National Laboratory, 7000 East Ave, Livermore, CA 94550, USA

⁶ University of California San Diego, 9500 Gilman Dr., La Jolla, CA 92093, USA

⁷ Columbia University, 2960 Broadway, New York, NY 10027-6900, USA

⁸ Oak Ridge Associated Universities, Oak Ridge, Tennessee, USA

^a Edge-localized-mode

E-mail: rnazikia@pppl.gov

Abstract

Resonant magnetic perturbations ($n=3$ RMPs) are used to suppress large amplitude ELMs and mitigate naturally occurring "grassy"-ELMs in DIII-D plasmas relevant to the ITER steady-state mission. Fully non-inductive discharges in the ITER shape and pedestal collisionality ($\nu^*_e \approx 0.05-0.15$) are routinely achieved in DIII-D with RMP suppression of the Type-I ELMs. The residual grassy-ELMs deliver a low peak heat flux to the divertor as low as 1.2x the inter-ELM heat flux in plasmas with sustained high H-factor ($H_{98y2} \approx 1.2$). The operating window for the RMP grassy-ELM regime is $q_{95}=5.3-7.1$ and external torque in the range 9 - 0.7 Nm in the co-Ip direction, which is in the range required for a steady-state tokamak reactor. The RMP grassy-ELM regime is associated with a two-step pedestal, with strong flattening of the density around the zero crossing in the ExB shear. The edge magnetic response of the plasma to the $n=3$ RMP is found to be $\approx 2-3x$ larger than for comparable ITER baseline plasmas ($\beta_N \approx 1.8$, $q_{95} \approx 3.1$). The amplification of the RMP is consistent with the weak magnetic perturbation level ($\delta B/B \approx 1 \times 10^{-4}$) required for effectively Type-I ELM suppression. Cyclic variations in the pedestal pressure, width, and toroidal rotation are observed in these plasmas, correlated with cyclic variations in the strength and frequency of the grassy-ELMs. Extended MHD analysis and magnetic measurements indicate that these pedestal pulsations are driven by cyclic variations in the resonant field strength at the top of the pedestal. These pedestal pulsations reveal that the grassy-ELMs are correlated with the proximity of the pedestal to the low- n PBMs (Peeling-Ballooning Modes) stability boundary. The use of low amplitude magnetic fields to access grassy-ELM conditions free of Type-I ELMs in high beta poloidal plasmas ($\beta_p \approx 1.5-2.0$) opens the possibility for the further optimization of the steady-state tokamak by use of edge resonant magnetic perturbations.

Keywords: Resonant-magnetic-perturbations, edge-localized-modes, pedestal stability

1. Introduction

Achieving effective edge-localized-mode control in high confinement steady-state fusion reactors is a key goal for fusion research with practical near-term implications for the operation of ITER and the design of next step steady-state tokamak reactors [1]. ITER has (at least) two important programmatic goals: first to achieve $Q_{DT}=10$ in the so-called ITER baseline scenario with $I/aB \approx 1.4$ ($q_{95} \approx 3.1$ in the ITER shape), while the second is long-pulse (and hopefully fully steady-state operation) with $Q_{DT} \approx 4-5$ at reduced current ($q_{95} \approx 5-7$) [2]. In both these ITER operating regimes, the effective screening of metal impurities by the edge plasma and the preservation of the integrity of the divertor are essential. It is now understood that the control of so-called type-I ELMs is an important requirement for achieving these goals, both because of the cumulative and acute effects of such instabilities on impurity influx and accumulation, and divertor performance [3].

ELM suppression by 3D magnetic perturbations has been pursued vigorously since the discovery of the effect and the demonstration of its relevance to ITER baseline plasmas conditions (ITER shape, $\beta_N \approx 1.8$, $q_{95} \approx 3.1-3.5$) [4,5]. However, the method has had difficulties extending to low external neutral beam torque (i.e., low toroidal rotation) of great importance to ITER [6], with the exception of low beta helium plasmas ($\beta_N < 1$) [7]. The current understanding of the cause of this difficulty is that the $V \times B$ contribution to the electric field needs to be comparable in magnitude, but of opposite sign, to the pressure gradient contribution in order to allow for external non-axisymmetric fields to penetrate at low order rational surfaces in high-temperature fusion plasma [8,9].

Given the challenges of ELM suppression in the ITER baseline, it is a welcome surprise to discover that RMPs provide access to a new and highly reproducible grassy-ELM regime, free from the large variation of the peak heat flux associated with such plasmas without RMPs. Grassy-ELMs were first identified in DIII-D [10] in high β_p plasmas and later in JT60-U as a small high-frequency ELM regime occurring at low plasma collisionality and elevated poloidal beta [11,12]. These small ELM-like events were attributed to high- n ballooning modes, distinct from the low- n kink-peeling structure associated with large amplitude ELMs at low collisionality. The excitement about the grassy-ELM regime is that the parameters for its occurrence are in principle consistent with the requirement for steady-state tokamak operation. The main drawback of the grassy-ELM regime without use of RMPs is that, in practice, it is generally a mixture of type-I and grassy-ELMs, henceforth called a mixed-ELM regime. There are two issues with the mixed-ELM regime. First, even if only a small fraction of the ELMs are type-I ELMs, the peak heat flux to the divertor is not reduced, with consequent divertor erosion and impurity influxes. Second, there is as yet no clear understanding of the conditions for the complete avoidance of the mixed-ELMs in strongly shaped low collisionality plasmas relevant to ITER and future steady-state reactors. Therefore it is unclear what techniques are necessary to produce pure grassy-ELM behavior rather than the mixed-ELMs in future reactors [12].

In this paper we show that the addition of modest amplitude RMPs (in our case $n=3$ RMP with vacuum $\delta B_{vac}/B \approx 1 \times 10^{-4}$ in the plasma) effectively suppresses the Type-I ELMs and also mitigates the grassy-ELMs in ITER relevant steady-state conditions in the DIII-D tokamak with $\beta_N \approx 3$, $\beta_p = 1.5-2.0$, and $q_{95} = 5.3-7.1$. The effective elimination of mixed-ELMs represents an improved grassy-ELM regime that is reliably accessed using edge-resonant magnetic perturbations. The additional mitigation of the grassy-ELMs leads to very favorable properties of the peak heat flux to the divertor. We show that this RMP grassy-ELM regime can be achieved for a wide range of magnetic safety factor ($q_{95} \approx 5.3-7.1$) and neutral

beam torque ($\approx 9 - 0.7$ Nm) in plasma with high confinement factor ($H_{98y2} \approx 1.2-1.3$), $\beta_N \approx 3$ and $\beta_P \approx 1.5 - 2.0$ in the ITER shape and pedestal collisionality ($\nu_e^* \approx 0.05 - 0.15$). As such, the regime is quite promising not just for ITER steady-state operation but also for the design of future steady-state reactors where strong shaping is essential.

New physics understanding is also being developed in this enhanced grassy-ELM regime. We find that the grassy-ELMs are associated with a naturally wide pedestal, approximately twice the pedestal width and pressure of ITER baseline plasmas with comparable stored energy $W_{\text{dia}} \approx 1$ MJ, toroidal field $B_T \approx 1.95$ T and ITER shape $\delta \approx 0.55$. These plasmas differ principally in the plasma current ($I_p \approx 1$ MA in the grassy-ELM regime vs. 1.5 MA in the ITER baseline). The enhanced pedestal pressure in the grassy-ELM plasmas result in a stronger amplification of the applied RMP relative to ITER baseline plasmas [13], typically 2-3x the vacuum RMP level with only a weak effect on global confinement and stability. The pedestal temperature increases during density "pumpout" so that the overall confinement is not significantly degraded. The pedestal width in these grassy-ELM plasmas remain near 10% of the poloidal minor radius with the applied RMP, which exceeds the EPED model prediction of the pedestal width by up to 50% [14].

New insight is also obtained on the underlying physics of the grassy-ELMs from naturally occurring pedestal pulsations at the low q_{95} range of these RMP plasmas. These pulsations are characterized by a periodic rise and fall in the edge toroidal rotation and pedestal width. The pulsations are consistent with recent theoretical predictions of limit cycle behavior of magnetic island growth and damping due to the competing influence of resonant field braking and flow screening [15,16]. The grassy-ELM amplitude can be strongly mitigated and sometimes fully suppressed during a specific phase of the pedestal cycle. The grassy-ELMs are strongest in that part of the cycle when the pedestal is closest to the low- n PBM stability boundary calculated using the ELITE code [17], and are weakest or fully suppressed when the pedestal is most stable to low- n PBMs.

This paper is organized as follows. Section 2 presents an overview of the experimental results, the plasma condition for grassy-ELM, the ELM characteristics and the operating window for the RMP grassy-ELM regime. Section 3 presents stability analysis during the suppression of the Type-I ELMs. Section 4 discusses the amplification of the vacuum RMP by the edge plasma and the consistency of the measured and calculated plasma response using the ideal-MHD version of the GPEC (generalized perturbative equilibrium code) code [18]. Section 5 discusses pedestal pulsations and their correlation with the screening and penetration of edge resonant magnetic perturbations using the linear single-fluid MHD stability code M3D-C¹ [19]. The section also discusses the correlation of the grassy-ELM activity with the pedestal width and peeling-ballooning-mode stability. Section 6 discusses the weak effect of rotation on the grassy-ELM regime. Section 7 discusses similarities in the phenomenology of grassy-ELMs with weak ELMs observed elsewhere at low collisionality and identifies areas for further research. The summary is presented in section 8.

2. Experimental overview

Sustaining future tokamak reactors in steady state conditions will require well-controlled plasma-wall interactions, including the elimination or strong ($>10x$) mitigation of Type-I ELMs. On DIII-D we achieve robust access to a grassy-ELM regime with the application of $n=3$ edge resonant magnetic perturbations in plasmas with the ITER shape, pedestal collisionality and with full noninductive current drive. [Figure 1](#) shows two well-matched discharges in DIII-D, one with an odd-parity $n=3$ RMP (blue) and the other

without the RMP (red). The RMP is applied using internal coils in DIII-D. The DIII-D tokamak has two rows of six picture-frame coils inside the vacuum vessel, called the I-coils (see Fig. 2(a) for the poloidal location of the two rows of I-coils). The two rows of six toroidally spaced coils can produce an $n=3$ perturbation with either odd or even parity, where the odd parity configuration corresponds to the opposite phasing of currents in the upper and lower rows of coils (see Fig. 1 in [20]). The even parity configuration corresponds to the same phasing between the currents in the upper and lower coils (see Fig. 1 in [21]). For these steady-state relevant plasmas, the odd parity configuration is chosen in order to apply an edge resonant field for magnetic safety factors in the range $q_{95} \approx 5-7$. In comparison the ITER-baseline plasmas with $q_{95} \approx 3.1-3.5$ require an $n=3$ even parity configuration for achieving edge resonance. Here we use the term ITER baseline generically on DIII-D to denote plasmas with the approximate ITER shape (LSN, $\delta \approx 0.55$), collisionality range $\nu_e^* \approx 0.1-0.2$, $\beta_N \approx 1.8$ and $q_{95} \approx 3.0-3.5$.

With the application of the $n=3$ RMP, the plasma edge transitions from a mixed ELM regime [11] to a mitigated grassy-ELM regime by the elimination of the Type-I ELMs. The plasmas in Fig. 1 are fully noninductive with and without the RMP (see surface voltage in Fig. 1(e)) and are very well matched as indicated by the evolution of the plasma parameters. The plasma and machine parameters in this paper are: $I_p = 0.95-1.25$ MA, $B_T = 1.7$ T, LSN with triangularity $\delta \approx 0.55$, noninductive fraction $f_{NI} = 80-100\%$, pedestal collisionality $\nu_e^* \approx 0.05-0.15$, $\beta_N \approx 2.5-3$, $\beta_P \approx 1.5-2.0$, neutral beam power $P_{NBI} \approx 6.0$ MW, electron cyclotron heating power $P_{EC} \approx 3$ MW, and confinement factor $H_{98y2} \approx 1.2-1.3$. The beam power is adjusted using beta feedback to maintain constant β_N ; the power typically increases by $<10\%$ with the applied RMP. A thorough discussion of the core transport properties of these fully noninductive plasmas and their extrapolation to ITER steady-state relevant conditions, along with MHD induced energetic particle transport and global stability limits is contained in a recent paper [22]. The plasma shape and core profiles for the discharges in Fig. 1 are shown in Fig. 2 during the stationary phase of the discharge near 4000 ms. The profiles are very similar for the two cases with (blue) and without RMP (red).

The energy loss due to the grassy ELMs can be substantially less than for Type-I ELMs (typically 10x less). This difference can reach 40-50x on DIII-D with the application of the $n=3$ RMP. For the type-I ELMs in the no-RMP plasma (red) in Fig. 1(b), the energy loss inferred from diamagnetic loop measurements is $\approx 7\%$ of the plasma stored-energy. Infrared measurements detect about 50% of the energy loss as heat flux to the divertor. With the elimination of the type-I ELMs and the mitigation of the grassy-ELMs by the RMP (Fig. 1(a)), the energy loss can drop to less than 0.1% per grassy-ELM in DIII-D. At this level the loss is not detectable from magnetic or profile measurements of the plasma and is instead inferred from the heat flux to the divertor.

With the elimination of the Type-I ELMs and the mitigation of the grassy-ELMs, the $n=3$ RMP produces a substantial reduction in the peak heat flux to the divertor. The infrared IR camera measurement of the peak heat flux at the inner strike point P_{ISP} (see Fig. 2(a)) for the plasmas without and with the RMP in Fig. 1 is shown in Fig. 3(a), (b), respectively. Mixed ELMs without the RMP are seen in Fig. 1(b) and Fig. 3(a) whereas mitigated grassy-ELMs are seen with the $n=3$ RMP in Fig. 1(a) and Fig. 3(b). The presence of mixed ELMs (a combination of Type-I and grassy-ELMs) shown in Fig. 3(a) is expected to be detrimental to divertor operation in a fusion reactor because the peak heat flux does not decrease substantially even if the frequency of the Type-I ELM is greatly reduced. In contrast, the heat flux for the RMP plasma in Fig. 3(b) shows highly mitigated grassy-ELMs leading to a small ($\approx 20\%$) modulation of the peak heat flux and a high frequency (≈ 500 Hz) of small ELMs. A similar small variation in the peak heat flux is seen at the outer strike point, however IR measurements are less available from that region of the divertor due to the shadowing of the IR camera view (see Fig. 2(a)). We will return to discuss the outer

strike point heat flux later in Sec. 2.

Profile analysis reveals that the pedestal width is wider when grassy-ELMs are present. Figure 3(c), (d) shows the edge Thomson scattering measurement of the electron temperature and density profiles, respectively, in the intervals indicated by the vertical dashed lines in Fig. 3(a), (b). For the no-RMP case, (Fig. 3(a)) there is considerable intermittency in the grassy-ELM activity early in the discharge. Two intervals are selected, one during an ELM free period at ≈ 2510 ms (black dashed line) and the other during a grassy ELM period at ≈ 2580 ms (red dashed line). The profiles are shown for the two times in red (≈ 2510 ms) and black (≈ 2580 ms) in Fig. 3(c), (d). The pedestal width for the density and electron temperature is significantly larger in the grassy-ELM interval (≈ 0.12) compared to the ELM free interval (≈ 0.08) in normalized minor radius. For the discharge with the $n=3$ RMP, the grassy-ELMs are no longer intermittent and the width of the pedestal is similar to the grassy-ELM phase without RMP (blue curves in Fig. 3(c), (d) taken at ≈ 5000 ms in Fig. 3(b)). Figure 4 shows a comparison of the pedestal width in units of normalized poloidal flux for the two discharges in Fig. 1 compared to the EPED model prediction. The EPED model uses a critical gradient kinetic-ballooning-mode model [23], which yields a pedestal width $W_{\text{EPED}} \approx C_{\text{EPED}} \beta_{\text{p,ped}}^{1/2}$ where $\beta_{\text{p,ped}}$ is the measured pedestal poloidal beta and C_{EPED} is a coefficient of order 0.1 (here set to 0.09 to match the pedestal width in the early Type-I ELMing phase of the discharge at ≈ 2000 ms). The pedestal width for the RMP (blue) and no-RMP (red) case is obtained using a Tanh fit to the electron temperature profile and is compared to the model prediction of the pedestal width (black). The pedestal width for the RMP case is comparable to the case without the RMP in the stationary phase of the discharge, indicating the weak effect of the RMP on the pedestal width for these plasmas. We note that there is a rapid increase in the pedestal width in the no-RMP case (red) in Fig. 4 around 3000 ms, coincident with a transition from regular to infrequency Type-I ELMs (Fig. 1(b)), which also coincides with the increase in the plasma beta and poloidal beta seen in Fig. 1(d). We will return to the correlation of the wide pedestal with the grassy-ELM activity in Sec. 5.3.

The elimination of mixed ELMs and mitigation of the grassy-ELMs using the $n=3$ RMP is encouraging for steady-state tokamak operation, however a number of challenges must be resolved in order to validate the compatibility of this regime with future steady-state reactors. One issue is whether impurity control can be maintained with the elimination of the Type-I ELMs. It has been shown elsewhere that $n=2$ RMPs with central electron cyclotron heating ECH can prevent the accumulation of tungsten in the core of the AUG tokamak during Type-I ELM suppression [24]. The introduction of short bursts of non-recycling fluorine also confirms the effectiveness of intermediate-Z impurity exhaust in DIII-D ELM suppressed plasmas in ITER baseline conditions [25]. These studies have been extended to the RMP grassy-ELM regime using non-recycling chlorine gas. Figure 5(a) shows the spectroscopic measurement of the chlorine +15 line intensity at 1002.1 Å (helium-like chlorine) in the plasma core for a discharge similar to the RMP plasma of Fig. 1 with the same $n=3$ RMP ($n=3$, 2.5 kA I-coil current and odd parity). The exponential decay rate of the chlorine signal reveals a particle confinement time $\tau_p \approx 180$ ms during RMP suppression of Type-I ELMs, which is within 2-3x the energy confinement time ($\tau_E \approx 70$ -80 ms) in these plasmas. The compatibility of the grassy-ELM regime with tungsten-coated divertor tiles was also studied during the DIII-D metal ring campaign. The experiments revealed no detectible concentration of tungsten in the plasma core using X-ray spectroscopic measurement tuned to the W45+ line (62.34 Å) with the outer strike point riding on the tungsten tiles (Fig. 22 in [26]). Overall, the combination of large amplitude ELM suppression and grassy-ELM mitigation using $n=3$ RMPs, together with the effective exhaust of impurities, is very encouraging for the further exploration of this regime for steady-state tokamaks.

2.1 Operational window

We can access the RMP grassy-ELM regime in DIII-D over a wide range of plasma parameters relevant to the ITER steady-state mission and to future steady-state reactors, with magnetic safety factor $q_{95} \approx 5.3-7.5$ and neutral beam torque $T_{\text{NBI}} \approx 6 \text{ Nm} - 0.7 \text{ Nm}$. This range of access is quite surprising considering the narrower windows of rotation and q_{95} required for ELM suppression in the ITER baseline [6,27]. Figure 6 shows the D_e trace from the inner strike point (radius $R_{\text{ISP}} \approx 1.01 \text{ m}$ in Fig. 2(a)) for six similar discharges, differing mainly in the plasma current. The H-factor and β_N for all plasmas is similar, $H_{98y2} \approx 1.2-1.3$, $\beta_N \approx 3.0$. The normalized electron collisionality at the top of the pedestal is also in the range $v_e^* \approx 0.05-0.15$ for all these plasmas, similar to the range expected in ITER and future reactors [5]. We note here that the H-factors take into account the decreased absorption of neutral beam power due to MHD induced fast ion loss, which accounts for the increase in beam power (Fig. 1(f)) required to maintain constant beta. Without this correction we get $H_{98y2} \approx 1.1$. The effect of MHD activity on the absorbed power is discussed more fully elsewhere [22]. The data in Fig. 6 indicates that the RMP is effective in eliminating the mixed ELMs over a contiguous range of q_{95} relevant to steady-state tokamak operation.

The enhanced grassy-ELM regime is also compatible with low neutral beam torque. Low beam torque in DIII-D is obtained using counter-current neutral beam injection. We use counter beam injection in order to access the low rotation conditions anticipated in ITER. Figure 7 shows a torque ramp in an RMP grassy-ELM plasma from $T_{\text{NBI}} \approx 3 \text{ Nm}$ to $\approx 0.7 \text{ Nm}$, obtained by applying a 2 MW counter neutral beam at 2.5 s. The grassy-ELM regime appears quite compatible with low beam torque. The infrared camera measurement of the grassy-ELM induced heat flux at the inner strike point P_{ISP} shown in Fig. 7(a) (red) indicates, if anything, a decrease at low torque. The toroidal rotation from carbon VI spectroscopic measurements is shown in Fig. 7(b) at the core and edge of the plasma. The sustainment of grassy-ELMs down to $\approx 0.7 \text{ Nm}$ is encouraging for the relevance of the RMP grassy-ELM regime to ITER and future steady-state tokamaks. In comparison, the initial torque of $\approx 3 \text{ Nm}$ at $\approx 2450 \text{ ms}$ is near the lower limit for achieving ELM suppression in the ITER baseline [6]. The major issue when approaching zero torque is the onset of locked modes, due to the appearance of $m/n=2/1$ island at the $q=2$ rational surface and subsequent mode locking. A locked mode appears in the discharge in Fig. 7, but not before sustained grassy-ELMs are observed at reduced torque and rotation. Future studies must address the locked mode issue by further optimizing the error field correction and by exploring low torque operation with $q_{\text{min}} > 2$. Other small ELM or ELM suppressed regimes are also being explored for compatibility with low torque operation such as the wide-pedestal QH mode in DIII-D [28]. The extension of the grassy-ELM regime to low beam torque ($< 1 \text{ Nm}$) is quite positive, however further development is needed to establish stationary low torque operation.

2.2 Grassy-ELM mitigation

The mitigating effect of the RMP on grassy ELMs is revealed in a statistical analysis of the two discharges in Fig. 1. Figure 8(b) shows the distribution of the grassy-ELMs plotted against the peak heat flux and the interval between ELMs for the no-RMP plasma (red) and the RMP grassy-ELM plasma (blue) during the stationary phase of the discharge from 4.2-5.2 s. The histogram reveals a significant reduction in the peak heat flux, but not a significant increase in the grassy ELM frequency going from the no-RMP plasma to the RMP plasma. Instead, there is a narrowing of the distribution in both amplitude (Fig. 8(c)) and the

interval between ELMs (Fig. 8(a)), indicating that the RMP effectively regulates the grassy-ELMs. While the median interval between ELMs is the same in the two cases (≈ 2 ms), the spread narrows significantly leading to enhanced regulation of the grassy-ELMs. The peak heat flux also transitions from a broad distribution to a narrow distribution from Fig. 8(c). The general understanding is that the interval between ELMs is determined by the time it takes for the pedestal to recover after the loss of energy produced by the ELM. Given that the RMP reduces the spread in the amplitude of the ELMs (Fig. 8(c)) we should expect a corresponding reduction in the spread of the interval between ELMs, as is seen in Fig. 8(a). We point out that the RMP tends generally to mitigate the grassy-ELMs in these plasmas.

The heat flux of a Type-I ELM and an RMP mitigated grassy-ELM at the inner strike point is shown in Fig. 9 for a plasma with similar parameters indicated in the figure caption. Figure 9(a) shows the peak heat flux to the inner strike point (radius $R_{ISP} \approx 1.01$ m, Fig. 2(a)) during a Type-I ELM before the RMP is applied (red) compared to a grassy-ELM during the RMP phase (blue). The infrared camera frame rate is limited to 0.08 ms (≈ 12 kHz), which is marginal for catching the rise time and peak heat flux associated with Type-I ELMs. Nonetheless, two qualitatively important features can be discerned from the comparison. The spatial distribution of the heat flux during the ELM, and 1 ms before the ELM, is shown in Fig. 9(b), (c) for the RMP grassy-ELM and for the Type-I, respectively. The first important observation is that the inter-ELM heat flux (dashed line) increases for the RMP (blue) vs. no-RMP (red) phase. This is consistent with enhanced inter-ELM thermal transport to the divertor induced by the RMP. The second observation is that the peak heat flux during the grassy-ELM is within 50% of the inter-ELM peak heat flux and the footprint or wetted area of the grassy-ELM is similar to the wetted area of the inter-ELM heat flux in Fig. 9(b). A similar behavior is also observed at the outer strike point when data is available. In contrast, the peak heat flux during the Type-I ELM can be 10x or higher than the inter-ELM phase in the case without RMP (Fig. 9(c)). In addition the heat flux spreading is substantial during the Type-I ELM, about 4-5x the width of the inter-ELM heat flux on the inner wall. This spreading is beneficial for reducing the peak heat flux but it can have adverse effects on erosion and material migration in the far SOL.

From Fig. 9 we see that the wetted area strongly decreases for the grassy-ELMs relative to the Type-I ELMs and is of the order of the inter-ELM width. For ITER, we need to get an ELM energy deposition of <0.5 MJ/m² to avoid melting of the divertor (including macrobrush edges but excluding W surface degradation over a large number of ELMs) and this corresponds to 0.7 MJ ELMs if the ELM wetted area is similar to the inter-ELM wetted area. We expect to have 20-30 MJ uncontrolled ELMs in ITER and thus a 20-30x reduction is required in the peak heat flux [29]. Generally, grassy-ELMs have about 10x less energy loss from the plasma than Type-I ELMs. This is good news but it does not guarantee protection of the divertor against edge melting or long-term erosion. With the RMP grassy-ELMs we have observed greater than 20x mitigation relative to the Type-I ELMs (see Fig. 3), which will improve protection of the divertor and may be sufficient to prevent reattachment during ELMs.

An important question is whether the regulation of grassy-ELMs is the result of $n=0$ profile changes due to RMP induced transport or whether the $n=3$ perturbed equilibrium has a linear or nonlinear effect on the grassy-ELMs. While we cannot directly measure the full magnetic spectrum of the grassy ELMs, we can analyze the low- n magnetic response of the plasma during grassy-ELMs on arrays of magnetic probes with locations indicated in Fig. 2(a). Figure 10 shows the $n=1$ component of the magnetic perturbations associated with grassy-ELMs measured at location 66M on the outboard midplane in a 5 ms interval for the plasmas from Fig. 1 with and without the $n=3$ RMP. For the no-RMP case in Fig. 10(a), the $n=1$ component of the grassy-ELMs rotate in the electron diamagnetic drift direction (i.e., counter to the direction of the plasma current). This is commonly observed for small ELMs in DIII-D and is consistent

with the toroidal rotation of the ELM magnetic perturbation in the counter current direction due to the negative radial electric field in and at the pedestal top. We point out that the radial electric field remains negative at the top of the pedestal for the RMP discharge in Fig. 1 (see Fig. 35 for typical E_r profile), however the $n=1$ component of the grassy ELMs is locked to the lab frame as shown in Fig. 10(b); there is no mode rotation. The $n=2$ and $n=3$ components of the grassy-ELMs in the RMP discharge are also locked in the lab frame (not shown). The phase locking of the $n=1,2,3$ components of the grassy-ELMs in a region with significant radial electric field suggests some level of mode coupling with the $n=3$ perturbed equilibrium. Such coupling may also lead to the mitigation of the grassy-ELM. The peak amplitude of the grassy-ELM in the no-RMP plasma is ≈ 8 Gauss, about twice the amplitude of the RMP grassy-ELM at the outboard midplane. There is also a similar difference in the peak heat flux due to the grassy ELMs in the two cases (not shown). This phase locking to the lab frame suggests a mitigating effect of the RMP on the grassy-ELM due to a linear or nonlinear interaction with the $n=3$ perturbed equilibrium.

Recent theoretical studies have shown that nonlinear mode mixing can mitigate the amplitude of ELMs by reducing the coherence of the fastest growing (dominant) mode [30]. While the work did not discuss the role of RMPs, it is plausible that a strong magnetic perturbation could cause decorrelation of the fastest growing mode by inducing mode coupling to sidebands $n \pm kN$, where n is the toroidal mode number of the dominant mode, N is the mode number of the RMP and $k=0,1,2,\dots$ is an integer. Nonlinear simulations using the JOEK code [31] for RMP ELM interactions have reveal ELM mitigation by the nonlinear generation of multiple MHD sidebands together with the phase locking of the ELMs to the static RMP as observed in experiment [32,33]. Of course, there are significant challenges in rigorously validating such a nonlinear interpretation for the mitigation of the grassy-ELMs in DIII-D. First it will be necessary to measure the dominant toroidal mode number of the grassy-ELM. Such a direct measurement would require careful analysis of pedestal fluctuations (beyond the scope of this paper) or the use of plunging magnetic probes that can be inserted close to the separatrix in order to measure the dominant toroidal harmonic, assumed to be low to intermediate- n ($n < 20$) Peeling-Ballooning-Modes (PBMs).

Recent studies using infinite- n ideal ballooning theory suggest that the underlying linear instability for small ELM-like events can also be affected by the 3D perturbed equilibrium, leading to localization of the mode and its destabilization [34]. However, global kinetic ballooning mode (KBM) studies of ITER baseline plasmas indicate that the effect of the perturbed equilibrium on linear stability is negligible in DIII-D conditions [35], while experimental studies have yet to reveal a clear identification of linear destabilization by the RMP. While the nonlinear interaction and resulting mitigation of the grassy-ELM by the RMP is likely from the data and simulations, much remains to be done to isolate the effect of 3D fields on the linear stability of the grassy-ELMs in DIII-D.

2.3 Role of plasma density in Type-I ELM suppression

Plasma density appears to play a role in the transition from mixed-ELMs to grassy-ELMs in DIII-D. For similar global plasma parameters, a decrease in the pedestal density (corresponding to a decrease in the edge collisionality) appears beneficial for the suppression of the Type-I ELMs and the mitigation of the grassy-ELMs. Figure 11(a) shows the peak heat flux to the inner strike point for an RMP grassy-ELM discharge with the pedestal density shown in Fig. 11(b). The data shows a strong dip in the density due to pumpout and the suppression of Type-I ELMs by the RMP. Gas injection raises the density later in the discharge, leading to a return of Type-I ELMs.

The observation of Type-I ELM suppression with decreasing density is similar to observations in ITER-baseline plasmas with RMPs where the pedestal density needs to go below a certain threshold for Type-I ELM suppression. This similarity suggests a common factor for Type-I ELM suppression in the grassy-ELM and ITER-baseline plasmas involving the conditions required for resonant field penetration. By penetration, we mean that the external field drives a resonant radial magnetic field at the rational surface leading to magnetic island formation [8,9,36]. Analogous to locked mode physics [15], decreasing density can decrease plasma viscosity in the pedestal, enabling resonant fields to penetrate provided the ExB velocity is sufficiently small at edge rational surfaces. We also observe a trend of decreasing grassy-ELM amplitude as the density (and collisionality) decrease in the pedestal, similar to observations in JT60-U [12]. This can best be seen by comparing the grassy-ELM amplitude at $t=2800$ ms and $t=3400$ ms in Fig. 11(a), (b). We return to the role of resonant field penetration in Type-I ELM suppression and grassy-ELM mitigation in Sec. 5 when discussing pedestal pulsations.

The IR camera data presented thus far were all taken from the inner strike point due to the outer strike point (OSP) being obscured from the camera's view by the lower shelf, shown in Fig. 2(a). However, there are a few discharges where the OSP is visible to the IR camera. In these cases, we find that the OSP IR data is consistent with trends found at the ISP. Figure 12 is taken from a discharge where IR camera data is available at the outer and inner strike point for an RMP grassy-ELM discharge with similar parameters to the RMP plasma in Fig. 1(a). In Fig. 12(a) the integrated heat flux to the inner divertor (blue) and outer divertor (red) is shown together with their sum (in MW). The total injected power from neutral beams and ECH is also shown (dashed line). The ohmic current and hence ohmic heating is negligible in these plasmas. The total heat flux to the divertor from the IR data is comparable to the total injected power. We should be cautious to claim that all the heating power goes to the divertor as there are calibration uncertainties in the IR measurement that could account for up to 30% uncertainty. Nonetheless, the data clearly shows that the grassy-ELMs contribute only a small ($\approx 20\%$) increase in the thermal power reaching the divertor relative to the inter-ELM level. Figure 12(b) shows the peak heat flux (in MW/m^2) at the ISP (blue) and OSP (red) in the same interval. The data from the OSP shows even a smaller fractional increase in the peak heat flux during the grassy-ELMs relative to the inter-ELM period than for the ISP data. However, it is safer to say that there is no significant difference in the ratio of the peak to inter-ELM heat flux to the OSP and ISP. Based on these observations, we are confident that the trends observed at the ISP are indicative of the effect of the RMP on the heat flux at the OSP, with the main difference that the peak heat flux to the outer strike point is $\approx 2x$ higher than for the ISP.

3. Pedestal stability and Type-I ELM suppression

The suppression of the Type-I ELMs soon after the application of the RMP is consistent with the change in the stability of Peeling-Ballooning Modes (PBMs) for these plasmas. Generally the effect of the RMP is difficult to detect on the pedestal profiles during the late stationary phase of the discharge, (i.e., compare the profiles in Fig. 2). However, in the early phase of the discharge the RMP induces a momentary dip in the pedestal pressure that is large enough to detect as a change in PBM stability. This change is in the direction of stabilizing the PBM. Figure 13(a) shows a transition from large amplitude ELMs to grassy ELMs as the I-coil current (red line) is increased around 2200 ms. A single row of $n=3$ upper I-coils with 4.5 kA current is used in this discharge, with plasma parameters $q_{95} \approx 5.25$, $\beta_N \approx 2.5$, $\beta_p \approx 1.5$ and an ITER-relevant pedestal collisionality, $\nu_{*e} \approx 0.05$. This single row I-coil configuration is still edge resonant, as will

be shown in Sec. 4. The reduction in the pedestal density with the RMP shown in Fig. 13(b) is commensurate with an increase in the pedestal temperature from ≈ 1 keV to ≈ 1.7 keV.

The transition from mixed ELMs prior to the RMP to grassy-ELMs corresponds to a reduction in the pedestal pressure and density, as shown in Fig. 14. The reduction in the electron pressure comes predominantly through the density pumpout (Fig. 14(b)) and is partially compensated by the increase in the pedestal temperature (Fig. 14(a)). The ion temperature (not shown) is close to the electron temperature. The effect of these changes is shown in the stability analysis in Fig. 15. There is a shift in pedestal stability from the unstable region (red) to the stable region (blue) for low- n PBMs, however, the shift is relatively small when compared to the experimental uncertainties. It is more important to point out that the pedestal remains very close to the PBM stability boundary even after the complete suppression of the Type-I ELMs. The mixed ELM pedestal (red) before the RMP is PBM unstable with dominant toroidal mode number $n \approx 10$, whereas the grassy-ELM pedestal (blue) during the RMP resides in the PBM stable region.

As noted earlier, the reduction in the pedestal pressure is typically transient and recovers soon after the application of the RMP. However the Type-I ELMs continue to remain suppressed. Stability analysis during the stationary phase of the discharge shows that the pedestal remains very close to the PBM stability boundary during the grassy-ELMs or mixed ELMs. The small difference in the profiles with and without RMP makes it difficult to discern a systematic difference in the stability during the stationary phase of the discharge. However, the proximity of the pedestal to the low collisionality (low- n) PBM stability boundary when Type-I ELMs are completely suppressed, suggests that the grassy-ELM is a modified form of the low- n peeling-ballooning mode. We could test this hypothesis by devising a method to transiently force the pedestal deeper into the stable region of PBM stability. Fortunately, it turns out that the plasma does this spontaneously during pedestal pulsations (Sec. 5), which allows us to confirm that the grassy-ELMs indeed occur when the pedestal is close to the low- n PBM stability boundary.

The similarity in the stability threshold of the Type-I ELM and the grassy-ELM reveals the challenge of suppressing the Type-I ELMs. The grassy-ELM is less stable in these discharges than the Type-I ELM, but only by a thin margin. Both modes are proximate to each other in stability space, and the challenge is to drive sufficient transport through the grassy-ELMs or through the combination of grassy-ELMs and RMPs to prevent the onset of the more stable but much more virulent Type-I ELM. The prevalence of the mixed-ELM regime in the absence of RMPs is an indication of the feeble transport produced by the grassy-ELMs, at least in present devices. Given the marginal nature of Type-I ELM suppression with grassy-ELMs alone [37], it is likely that the addition of a small amplitude RMP kicks the pedestal into a pure grassy-ELM regime by providing an incremental increase in thermal transport sufficient to prevent the pedestal reaching the Type-I ELMs stability boundary. This enhanced transport can be a combination of particle and thermal transport associated with the RMPs, which forms the basis for ELM suppression in the ITER baseline. The major difference here is that the RMP has help from the grass-ELMs (and vice versa), enabling robust suppression of the Type-I ELMs by their combined effect.

The relationship between the grassy-ELM and the Type-I ELM is analogous to the low- n Edge Harmonic Oscillation (EHO) in the QH-mode regime. A key feature of the low- n ($n=1,2$) EHO is that it is driven by ExB shear when the pedestal is close to the low- n PBM stability boundary, but saturates at a low amplitude due to the relaxation of the drive [38,39]. The grassy-ELMs must have a dominant toroidal mode number higher than the EHO, however both modes appear to be related to the PBM by their proximity to low- n PBM stability boundary. Both modes saturate at low amplitude and both enhance pedestal transport sufficient to prevent the onset of the slightly more stable but much more explosive

Type-I ELM. Other regimes like the I-mode [40] and the wide-pedestal QH-mode [28] also depend on weak pedestal instabilities to prevent the onset of the Type-I ELMs.

A problem for all these weak-edge-mode regimes is that the pedestal can revert back to Type-I ELMs when the heating power exceeds the ability of the mode(s) in the pedestal to exhaust the input power. For the plasmas in the present study, the RMP generates additional inter-ELM (or baseline) transport that is additive to the transport produced by the grassy-ELMs. The combined effect of the RMP and the grassy-ELM is sufficient to achieve robust suppression of the Type-I ELMs, which would otherwise be marginal stable without the RMP. For the same reason, the incremental effect of the RMP on edge transport could be of assistance to other weak-edge-mode regimes such as the I-mode and wide-pedestal QH-mode to produce more robust Type-I ELM avoidance. As shown in Fig. 9(a), one effect of the RMP is to enhance the inter-ELM heat flux to the divertor. Analysis shows that the time average heat flux to the divertor from the grassy ELMs actually goes down slightly with the addition of the RMP. Therefore, the enhanced transport across the pedestal and to the divertor arises predominantly from the effect of the RMP on inter-ELM transport rather than any direct effect of the RMP on grassy-ELM dynamics.

4. Plasma response and antenna coupling

Rapid progress has been made in understanding the role of plasma response to 3D fields in ELM suppression. A key insight derived from multiple studies is that coupling to stable edge MHD modes is essential for achieving ELM suppression in high-temperature fusion plasmas [41–43]. By coupling, we mean that the spectrum of the applied 3D field overlaps with the spectrum of stable MHD modes of the plasma and results in driving those modes to finite amplitude. Coupling is important because it has been shown that resonant field penetration (i.e., a driven magnetic island at a rational surface) is more likely when the external field couples to stable MHD modes of the plasma [44]. More recently it has been discovered that in ITER baseline plasmas, which are far from MHD stability limits, the RMP couples to several highly stable modes in the plasma edge [45]. These stable modes typically have a strong peeling component (meaning they are predominantly driven by the edge current) and they exhibit significant magnetic perturbations at large poloidal angles away from the outboard midplane, including the top, bottom and inboard side of the plasma [46].

A new finding in these grassy-ELM plasmas at elevated q_{95} (> 5) and beta ($\beta_N \approx 3.0$) is the presence of one dominant marginally stable mode in the edge of the plasma that couples effectively to the $n=3$ RMP, producing an edge magnetic perturbation 2-3x the amplitude of the applied vacuum field. The measured plasma response indicates a clear outward ballooning mode structure consistent with MHD modeling and quite distinct from the response observed and calculated in the ITER baseline plasmas. Careful analysis reveals poor spectral matching of the I-coil spectrum with the least stable edge mode in these plasmas, indicating substantial scope for optimization of the coil design (and reduction of coil currents and engineering requirements) in future reactors.

A comparison of the relative strength of the plasma response to an $n=3$ RMP in an ITER baseline plasmas and RMP grassy-ELM plasma for DIII-D is shown in Fig. 16. The pair of discharges have closely matched parameters: ITER-like shape, electron density, toroidal field, and plasma stored energy ($B_T \approx 1.9$ T, $n_{e,ped} \approx 2.5 \times 10^{19} \text{ m}^{-3}$, $W_{dia} \approx 1.2$ MJ). The primary difference in engineering parameters is the plasma current and q_{95} ($\beta_N \approx 1.8$, $I_P = 1.6$ MA, $q_{95} = 3.4$ for the ITER baseline vs. $\beta_N \approx 3.1$, $I_P = 1.1$ MA, $q_{95} = 5.3$ for the grassy-ELM). The plasmas are fairly well matched in the vacuum resonant $n=3$ field at the top of the

pedestal (≈ 4 Gauss at the $q=10/3$ surface for the ITER baseline vs. ≈ 3 Gauss at the $14/3$ surface for the RMP grassy-ELM discharge). For the ITER baseline, we use $n=3$ even parity I-coils to maximize the resonant field strength at the $q=10/3$ surface, whereas we use only a single upper row of I-coils to produce the vacuum resonant field at the $14/3$ surface in the grassy-ELM plasma. Although the vacuum resonant field is 25% lower in the grassy ELM plasma, the magnetic response on the outboard midplane is considerably stronger. [Figure 16](#) shows the poloidal field produced by the plasma in response to the applied $n=3$ vacuum field measured at the outboard midplane (location 66M in [Fig. 2\(a\)](#)). The plasma response for the RMP grassy-ELM plasma (blue) is $\approx 3x$ the level for the ITER baseline (red). The vacuum field coupling to the sensors is removed from this data to reveal only the plasma response. Rapid reversal of the I-coil currents every 100 ms is used to subtract out the slow drift in the magnetic integrators [47], which is why the amplitude of the poloidal field appears like a square wave. The evolution of plasma parameters for these two discharges is shown in [Fig. 16\(b\)-\(d\)](#). The total stored energy, toroidal field and plasma shape for the two discharges are very similar ($W_{\text{dia}} \approx 1.1-1.2$ MJ, $B_T \approx 1.9-1.95$ T), so that the higher β_N and β_P comes from the lower plasma current in the grassy-ELM discharge. The electron pedestal pressure in the grassy-ELM discharge is approximately twice the pedestal pressure in the ITER baseline. This is a key factor in the amplification of the $n=3$ RMP due to the edge localization of the plasma response (Sec. 4.1). This same high edge pressure is also important for the amplification of edge-resonant intrinsic error fields.

4.1 Ideal MHD analysis

Ideal MHD calculations for RMP grassy-ELM plasmas reveals a strong edge localized response, peaking on the outer midplane. [Figure 17](#) displays the strength of the radial field perturbations calculated for a discharge similar to that in [Fig. 16](#). The plasma response is calculated using the Generalized Perturbative Equilibrium Code (GPEC) [18] based on an EFIT kinetic equilibrium with the plasma boundary and measured kinetic profiles similar to those shown in [Fig. 2](#), and using a 1 kA I-coil current in an odd-parity configuration for optimal edge coupling at $q_{95} \approx 5.2$, with $\beta_N \approx 3$ and $\beta_P \approx 1.6$. [Fig. 17\(b\)](#) shows the total radial magnetic field, i.e., the sum of the vacuum field and the plasma response. The odd parity arrangement is evident by the sign reversal in the radial field between the upper and lower coils. [Fig. 17\(a\)](#) displays the same data as in [Fig. 17\(b\)](#) but with the vacuum field removed, to show only the plasma response, which is what the sensor data shows. [Figure 17\(c\) and \(d\)](#) show the plasma response and total radial field perturbation for an even parity I-coil configuration. We see that the calculated plasma response for even parity is considerably weaker than for odd parity, which is why the odd-parity configuration is used for these plasmas.

It is interesting that the poloidal wavelength of the plasma response [Fig. 17\(a\), \(c\)](#) at the outer midplane is about equal to the poloidal width of the I-coil. This is a clear indication that the I-coils on DIII-D are poorly matched to the least stable edge mode in these plasmas. The coils are well matched for the poloidal mode number of the edge-plasma response in the ITER-baseline where $m \approx 10-11$ for $n=3$; they were not designed to match the edge plasmas response at higher q where $m \approx 14-20$ for $n=3$. [Figure 18](#) shows the $n=3$ vacuum spectrum for 1 kA of I-coil current with odd parity (blue), even parity (red) and for a single upper row (black dashed). The horizontal axis shows poloidal mode number in PEST coordinates (see [Fig. 2](#) in [48]). The edge plasma response is localized to the yellow vertical band in [Fig. 18](#). The single row spectrum (black) has been increased by 2x (equivalent to 2 kA in the upper row), to demonstrate that the amplitude spectrum of a single row represents the envelope function for any

combination of upper and lower I-coils. This result is quite general so long as each row produces a similar poloidal spectrum. The spectral range of the $n=3$ plasma response is beyond the primary lobe of the even and odd parity RMP vacuum field, underscoring the poor matching to the plasma response. On the other hand, there does appear to be a remedy. Guided by this result, we will operate future experiments with an $n=2$ RMP so that the plasma response (yellow band) will move down to the peak of the even parity response (primary red lobe). Furthermore, operating with $n=2$ RMP will allow more subtle control of the poloidal spectrum in order to more completely explore the plasma response and to assess the low I-coil current limit for Type-I ELM suppression in these plasmas.

We further validate the ideal MHD prediction of the dominant $n=3$ plasma response by performing a limited spectral scan in a single discharge. [Figure 19](#) shows the strength of the experimentally measured plasma response (blue) in a similar RMP grassy-ELM discharge. The coils were switched between all four possible I-coil configurations during the high beta phase of the discharge (from 3.2 s to 5.8 s with $\beta_N \approx 3.1$), and the currents were reversed every 100 ms to remove slow drift from the magnetic integrators. The measurements are obtained for the outer midplane. [Figure 19\(a\)](#) shows that the plasma response is relatively similar for the single row (upper or lower) and odd parity configurations. The even parity shows a weaker plasma response, qualitatively consistent with the GPEC calculation in [Fig. 17\(c\)](#). [Figure 19\(b\)](#) also shows the phase of the plasma response. Both the phase and amplitude are consistent with the GPEC calculations (red dots). While the dominant plasma response is quantitatively reproduced using GPEC for $n=3$ single upper/lower rows and odd parity, the even parity response is considerably stronger than predicted (i.e., at 4.4 s in [Fig. 17\(a\)](#)). The β_N in [Fig. 19\(c\)](#) show a small increase during the even parity phase near 4.4 s, which indicates a weaker effect on confinement relative to the other configurations.

The effect of the coil parity on Type-I ELM suppression can best be seen near threshold conditions. [Figure 20](#) shows the effect of density pumpout and ELM suppression in the transition from odd parity to even parity I-coils in a similar discharge. The suppression of Type-I ELMs and pumpout is seen in [Fig. 20\(a\)](#) with the turning on of odd-parity I-coils ([Fig. 20\(b\)](#)). A single large ELM is excited at $t=3400$ ms because the current is being reversed every 100 ms and the RMP field goes through zero during the reversal. At 3500 ms the I-coils change to even parity and the Type-I ELMs return with the increase in the plasma density. This and other data (e.g., [Fig. 11](#)) demonstrates a resonant effect of the RMP on the plasma edge.

The measured poloidal structure of the plasma response is also well reproduced by GPEC for these plasmas. [Figure 21\(a\)](#) shows the measured poloidal field amplitude for the plasma in [Fig. 19](#) for the upper, lower and odd parity I-coil configurations (symbols) vs. the DIII-D machine poloidal angle for various toroidal sensor arrays (see [Fig. 2\(a\)](#) for poloidal angles of magnetic sensors). There is excellent quantitative agreement between the GPEC calculated poloidal field distribution (solid lines) and the experimental data (symbols) for three of the coil configurations (odd, upper, lower) shown in [Fig. 21\(a\)](#). However, the GPEC calculation for the even parity configuration in [Fig. 21\(b\)](#) is not well matched to experiment, particularly at the outer midplane. The data for even parity coils suggests that some amount of coupling to the dominant mode may be occurring due to asymmetries in the coils (or the plasma) that is not included in the calculation, or to a possible contribution of sub-dominant edge modes that are not resolved by GPEC.

4.2 Error field amplification

We now address error field amplification in these plasmas because it is well known that at high beta the plasma will amplify the resonant component of low-n error fields (particularly the n=1 error field [49]) in addition to the applied n=3 RMP. While error field correction is designed to cancel the most deleterious plasma response that result in locked mode disruptions, some residual error field can still couple to the plasma edge to affect pedestal stability and transport. This understanding has been used successfully to achieve ELM suppression in the KSTAR tokamak using three rows of internal coils to preferentially drive an n=1 edge resonant response while minimizing coupling to the core kink response [50]. In ITER baseline and low beta plasmas well below the no-wall limit, the amplification of low-n modes are modest [45]. In contrast we can expect the strong amplification of residual low-n error field if they couple to the stable edge modes of the plasma.

Calibration data in the DIII-D tokamak shows that the n=1 intrinsic error field can have significant vacuum resonant fields at edge rational surfaces in these grassy-ELM plasmas. Even with good error field correction, a smaller n=1 edge resonant field can be amplified to a level comparable to the n=3 RMP. As a proxy for low-n intrinsic error fields, we calculate the n=1 and n=2 plasma response to a 1 kA current in the upper row of I-coils, corresponding to $\delta B_{vac} \approx 0.3 \times 10^{-4}$ at the q=4 rational surface for the equilibrium in [Fig. 21](#). In contrast, the n=3 field with 4.5 kA upper I-coil current has $\delta B_{vac} \approx 1.5 \times 10^{-4}$. [Figure 22](#) shows the amplification of the n=1 and n=2 error fields using the GPEC code for the kinetic equilibrium used in [Figure 21](#) and plotted on the same scale. The n=1 error field is amplified by more than 10x the n=3 field and about 5x the n=2 field. This means that any residual n=1 resonant component after error field correction can compete with the influence of the applied n=3 field in the pedestal for these high edge pressure plasmas. The implication is that, in principle, residual low-n EFs can affect pedestal stability and transport even if the most deleterious aspect of the error fields are minimized in the plasma core. The fact that n=1 resonant fields can be simultaneously optimized for ELM suppression and locked mode avoidance [50] demonstrates that intrinsic error fields in high beta plasmas can in principle exhibit strong interactions with the pedestal even if core coupling is minimized.

5. Pedestal oscillations and grassy-ELM mitigation

The RMP grassy-ELM plasmas exhibit large cyclic oscillations in the pedestal at low $q_{95} \approx 5.3$. These pulsations have a strong effect on the pedestal stability and nonlinear saturation of the grassy ELMs. Specifically, large variations of the pedestal toroidal rotation synchronous with n=1, 2, 3 magnetic oscillations are observed, consistent with a recently proposed model of magnetic island pulsation arising from a competition between island induced braking and flow-induced screening [15,16]. Single fluid linear MHD analysis using the M3D-C¹ code [19] reveals a correlation between oscillating resonant field penetration and oscillations in the pedestal rotation. These oscillations are fortuitous as they convey important information on the stability of the grassy-ELMs and on the role of edge resonant fields in pedestal transport. In addition, the pedestal oscillations shed new light on the effects of 3D fields on pedestal transport, which needs to be better understood in order to develop improved control of pedestal transport and ELM mitigation.

[Figure 23](#) reveals cyclic variations in the edge plasma parameters under the influence of a static n=3 RMP and intrinsic error fields for a discharge with plasma and machine parameters indicated in the figure caption. The n=3 RMP is generated using 4.5 kA of current in the upper row of I-coils. [Figure 23\(a\)](#) shows the D_e signal from the inner strike point for the duration of the discharge, revealing rapid suppression of the Type-I ELMs with the activation of the n=3 RMP. There are many pulsations in the D_e

light during Type-I ELM suppression. Expansion of a 200 ms time window in Fig. 23(b-e) reveals some of these pulsations in the pedestal and divertor. The D_α signal in Fig. 23(b) reveals slow modulations in the at the divertor with a period of ≈ 40 ms, compared to the plasma energy confinement time of 70-80 ms. Figure 23(c) reveals similar oscillations in the peak heat flux to the inner strike point from the IR camera. The grassy-ELMs seen at the ISP are largest when the inter-ELM heat flux is smallest and vice versa, as indicated by the blue and red bands in Fig. 23. The edge toroidal rotation at $\psi_N \approx 0.92$ (Fig. 23(e)) increases in the co- I_p (positive) direction when the pedestal enters into a period of mitigated grassy-ELMs, and decreases when the pedestal reverts back to regular (large) grassy-ELMs. The slow oscillations in the plasma beta, shown in Fig. 23(d), are anti-correlated with the edge toroidal rotation. Importantly, the decrease in β_N is strongest during the grassy-ELM mitigation phase, indicating that an additional transport mechanism is affecting the pedestal profiles, resulting in the mitigation and suppression of the grassy-ELMs. This additional transport mechanism is most consistent with oscillating resonant field penetration and screening where resonant field penetration in the pedestal is accompanied by an increase in toroidal rotation in the co- I_p direction and enhanced pedestal transport [9].

A closer look at these pulsations reveals that the grassy ELMs increase in frequency as they decrease in amplitude during the intervals of enhanced inter-ELM transport. In fact, during the periods when the grassy-ELMs are weakest, they cannot be seen on the D_α signal at the inner strike point and are only observable on the IR camera data. Figure 24 shows two such pulsations from the longer interval in Fig. 23. The grassy-ELM induced peak heat flux to the inner strike point (P_{ISP} in Fig. 24(a) in the yellow bands) is at least an order of magnitude smaller (≈ 0.1 MW/m²) than during the peak of the grassy-ELM activity (≈ 1 MW/m²). The grassy-ELM frequency can reach 800 Hz during mitigation, compared to ≈ 200 Hz at their largest amplitude. While IR data is not generally available at the outer strike point (OSP) due to shadowing of the camera view by the lower shelf, Langmuir probe measurements are available and show a similar trend to the inner strike data. The Langmuir probe current at the OSP (Fig. 24(c)) and at the ISP (Fig. 24(d)) is rapidly varying due to voltage scans used to infer the ion saturation current and the electron temperature at the probe. The envelope of the probe current can be discerned. The simultaneous increase in the ion saturation current to the OSP and ISP during the mitigation phase can be inferred from the upper envelope of the probe current in Fig. 24(c), (d). The increase of the electron temperature at the probe during mitigation can be inferred qualitatively from the lower envelope of the probe current during the voltage sweep. Analysis of the I-V characteristic of the Langmuir probe data reveals a three-fold increase in the ion saturation current at the ISP and a two-fold increase at the OSP during grassy-ELM mitigation. The electron temperature at the ISP increases from 8 to 10 eV while at the OSP the temperature increases from 30 to 50 eV, so that both the particle and thermal heat flux are enhanced during the period when the grassy-ELMs are at their weakest. This again points to the role of an additional transport mechanism associated with the RMP that controls the stability of the grassy-ELMs.

5.1 Pedestal stability

The modulation of the grassy-ELM amplitude and frequency suggests large changes in the pedestal profiles. Figure 25 shows pedestal profiles during grassy-ELM mitigation (red) and strong grassy-ELM activity (blue) in the blue ($t \approx 3620$ ms) and red ($t \approx 3635$ ms) bands in Fig. 23. The profiles are obtained using Thomson scattering and charge exchange measurements of fully stripped carbon in a 10 ms interval. The most significant change in the pedestal during the pulsations is an outward movement of the steep gradient region of the pedestal during mitigation of the grassy-ELMs along with an increase in the edge

toroidal rotation velocity in the co-Ip direction. Importantly, the ExB rotation frequency ω_{ExB} goes to zero near the top of the pedestal during the period of grassy-ELM mitigation (Fig. 25(f)). The red vertical dashed line in Fig. 25 indicates the top of the pedestal during grassy-ELM mitigation while the blue vertical dashed line indicates the top of the pedestal during strong grassy-ELM activity. The electron perpendicular flow frequency $\omega_{\perp e} = \omega_{*e} + \omega_{\text{ExB}}$ shows less modulation than ω_{ExB} during the pulsations and does not intercept zero near the top of the pedestal. The total pressure profile, pressure gradient and edge current profile are shown in Fig. 26 based on a kinetic EFIT calculation of the equilibrium from profile and magnetic measurements and using the Sauter model for the plasma current, which is valid at low electron collisionality. The interval of grassy-ELM mitigation has reduced pedestal pressure and pedestal width (red curves in Fig. 26) compared to the intervals with the strong grassy-ELM activity.

Both these profiles are in the stable region for peeling-ballooning modes (PBMs), as shown in the stability diagram obtained using the ELITE code in Fig. 27. However, the interval with strong grassy-ELMs is closest to the low- n ($n=5-10$) PBM stability boundary indicated by the blue upper contour in Fig. 27. The period of ELM mitigation (red) is furthest from the stability boundary. Thus, the weakening or sometimes the complete elimination of the grassy-ELMs during the pulsations is associated with the pedestal moving further into the stable region for PBMs. In actuality, the modulations have two effects. They modify the average pedestal pressure and edge gradient, and they modify the location of the stability boundary. The movement of the pedestal deeper into the PBM stable region is consistent with ELITE calculations of the pedestal stability in the ITER baseline [5]. The effect of the $n=3$ RMP on the grassy-ELMs seems to be analogous to the effect of the RMP on Type-I ELMs in the ITER baseline. The periodic mitigation of the grassy-ELMs as the pedestal moves away from the low- n PBM boundary reinforces the observation made from stability analysis in Fig. 15 that the grassy-ELMs must be excited close to the low- n PBM stability boundary.

5.2 Resonant field penetration

The linear single fluid M3D-C¹ code [19] is used to calculate the $n=1, 2$ and 3 resonant field components on low order rational surfaces in the pedestal region for the two profiles in Fig. 27 corresponding to the strong and mitigated grassy-ELM intervals. In the experiment we applied an $n=3$ RMP with 4.5 kA current in the upper row, however there are also less well characterized $n=1$ and $n=2$ intrinsic error fields in DIII-D that may play a role in the pedestal dynamics, particularly at beta due to plasma amplification (Sec. 4.2). Using M3D-C¹, we calculate the $n=1$ and $n=2$ resonant field produced by a 1 kA current in the upper row of I-coils as a qualitative indicator of the plasma resonant response to the intrinsic error fields.

Figure 28 shows the M3D-C¹ calculation of the resonant (radial) field component for the $n=1, 2,$ and 3 fields for the two equilibria in Fig. 27. Figure 28(d) shows the relevant plasma flow frequencies for the two times of interest, the ExB frequency ω_{ExB} and the electron perpendicular flow frequency $\omega_{\perp e}$. During the strong grassy-ELM interval (blue), $\omega_{\text{ExB}} \approx 0$ at the top of the inward shifted pedestal near the $q=4$ rational surface. The alignment of $\omega_{\text{ExB}} \approx 0$ to the $q=4$ surface suggests that the $n=1, n=2$ and $n=3$ fields can drive magnetic islands near the top of the pedestal during strong grassy-ELMs. During grassy-ELM mitigation, the top of the pedestal is displaced outward in radius near the $q=14/3$ rational surface (red). The alignment of $\omega_{\text{ExB}} \approx 0$ to the $q=14/3$ rational surface during grassy-ELM mitigation suggests that $n=3$ RMP penetrates near the top of the pedestal and is involved in the narrowing of the pedestal width during ELM mitigation. This contraction of the pedestal width with resonant field penetration is again analogous to the effect of RMPs in ELM mitigation in the ITER baseline plasmas. Figure 28(a), (b) show

M3D-C¹ single fluid calculations of the resonant field penetration for the n=1 and n=2 EFs, generated using 1kA current in the upper row of I-coils. The calculations show that the peak of the resonant field penetration occurs at the q=4 surface during strong grassy-ELM activity (blue). Figure 28(c) shows the M3D-C¹ calculation of the resonant field penetration for the n=3 RMP, generated using 4.5 kA current in the upper row of I-coils. The figure shows that the peak in the n=3 resonant field occurs at the q=14/3 rational surface during grassy-ELM mitigation.

From these calculations we infer that grassy-ELMs are mitigated and/or suppressed when the n=3 RMP penetrates at the 14/3 rational surface. The effect of such penetration is to enhance thermal and particle transport and flatten the pressure profile at the q=14/3 surface, leading to a narrowing of the pedestal width as seen in the data. The mitigating effect of the n=3 penetration on the grassy-ELMs is entirely analogous to the mitigating effect of RMPs on ELMs in the ITER baseline [8].

From the single fluid M3D-C¹ calculations the n=1, 2 resonant field amplitude at the q=4 surface is comparable to the n=3 resonant field at the q=14/3 surface, despite the fact that the n=3 RMP is generated using 4.5 kA of I-coil current vs. 1 kA for the n=1 and n=2 fields. We have seen in Sec. 4 that the n=1 and n=2 field can be amplified relative to the n=3 field in these plasmas, so it should be no surprise that the resonant field amplitude of n=1, 2 error fields at the q=4 surface can be comparable to the n=3 resonant field amplitude.

Note that we have used only the linear single fluid M3D-C¹ analysis in Fig. 28, and ignored the two fluid linear model, for the resonant field penetration. In linear two fluid theory, resonant field penetration requires that the perpendicular electron flow $\omega_{\perp e}$ be close to zero, i.e. $\omega_{\perp e} = \omega_{\text{ExB}} + \omega_{*e} \approx 0$ where ω_{*e} is the electron diamagnetic drift frequency. However, the $\omega_{\perp e} \approx 0$ requirement is only valid in the linear regime when the magnetic island width is much less than the linear layer width. In the case of islands much larger than the linear layer width we expect the island to propagate in the ion diamagnetic drift direction, i.e., $\omega = \omega_{\text{ExB}} + x\omega_{*i} \approx 0$ where x is between 0 and 1. For intermediate islands of the order of the linear layer width ($W_{\nu} \sim 0.01-0.03$ from the resonant fields in Fig. 28), we expect the frequency to be somewhere in between the two limits, or $\omega_{\text{ExB}} \approx 0$ [16]. Therefore we have chosen to use the linear single fluid analysis where the relevant condition for resonant field to occur is $\omega_{\text{ExB}} \approx 0$.

It has recently been shown that the competition between flow screening of magnetic islands and magnetic braking of plasma flows can result in nonlinear cyclic rather than stationary island solution [15,16]. These cyclic solutions are characterized by pulsations in the island width correlated with cyclic variations in the ExB velocity at the rational surface. According to the model, the magnetic islands continue to be dragged in the direction of the ExB rotation, producing oscillating JxB torque. The effect that we should see experimentally is the toroidal rotation of magnetic perturbations, even with static applied fields, together with modulations in the toroidal rotation. Therefore we look for such evidence in the magnetic data.

Figure 29 shows the poloidal field amplitude and phase of the plasma magnetic response on the outer midplane for the same interval as in Fig. 23(b). The data presented are of the amplitude and phase of the poloidal field at the outer midplane (location 66M in Fig. 2(a)) using a 100 ms running average subtraction to remove the drift in the integrator signals. The data has been smoothed using a 20 ms running window average to remove the spikes associated with the grassy-ELMs. The vacuum field coupling to the magnetic sensors is also removed from the probe data. The observed amplitude modulations on the outboard midplane probes are quite strong (1-2 Gauss) for n=1, 2 and 3 fields. For comparison the total plasma response for the n=3 field is ≈ 6 Gauss (blue curve in Fig. 16(a)) so that the pedestal pulsations are modulating the n=3 plasma response by up to 30%. These pulsations are also seen on the radial field

probes at the same outer midplane location and they are observed for a range of averaging and background subtraction time windows applied to the data. A key feature of the data is the flow rotation of the magnetic perturbations in sync with the modulation of the toroidal rotation velocity. Figure 29(a) shows the modulation in the toroidal rotation velocity at $\psi_N \approx 0.92$. The phase of the $n=1$, 2, and 3 magnetic components are shown in Fig. 29(b), (d) and (f), respectively. The amplitudes are shown in Fig. 29(c), (e), (g). In the coordinates of DIII-D, rotation with increasing toroidal angle indicates a phase velocity in the electron diamagnetic drift direction (see Fig. 10); rotation with a decreasing phase indicates the ion diamagnetic drift direction. The $n=1$, 2 and 3 components rotate toroidally with the period of the pedestal pulsations.

An interesting feature in the magnetic data is that the $n=1$ mode rotates in the co- I_p direction (Fig. 29(b)) whereas the $n=3$ rotates in the counter- I_p direction (Fig. 29(f)). From Fig. 25(f), the $E_{\times B}$ rotation at the $q=14/3$ surface is negative so that the $n=3$ should rotate in the counter- I_p direction, consistent with the increasing phase of the $n=3$ signal. In contrast, the $E_{\times B}$ rotation at the $q=4/1$ surface is positive, indicating rotation will be in the co- I_p direction, consistent observations. While the $n=1$ and $n=3$ mode directions are consistent with islands being dragged in the direction of the local $E_{\times B}$ flow at the $q=4$ and $14/3$ surfaces, respectively, the $n=2$ component remains an anomaly. The data of Fig. 29(d) shows that the $n=2$ magnetic perturbation rotates in the counter- I_p direction. This direction suggests that the resonant surface is in the region of negative $E_{\times B}$, such as the $q=9/2$ rational surface, which is inconsistent with our linear single-fluid M3D-C¹ analysis and places the island in the region of large flow screening. This inconsistency should be addressed in a future experiment where the $q=9/2$ rational surface is scanned radially during pulsations, from the negative E_r to the positive E_r region, in order to identify a reversal in the direction of rotation of the $n=2$ signal.

In our experiment we observe multiple helicity modes whereas the nonlinear model of pulsating islands only refers to a single helicity. It is possible that different helicity islands can affect the dynamics of the pulsations. For example, in Fig. 28 the penetration of the $n=1$ and $n=3$ modes are out of phase. If the rotation profile simply moves up and down without flattening, (as shown in Fig. 25(d)) then as $|\omega_{E_{\times B}}|$ decreases at the $q=4$ surface ($n=1$ penetration) it will simultaneously increase at the $q=14/3$ surface ($n=3$ screening). This means that the penetration of the $n=1$ at the $q=4$ may lead to the screening of the $n=3$ at the $q=14/3$ and vice versa. At present we do not have the data to address the combined effects of the different helicity components of the magnetic perturbations on the pedestal pulsations. This question can be addressed by performing experiments in which the intrinsic $n=1$ and $n=2$ error fields are systematically reduced and enhanced using the I-coils, in order to determine the effect(s) of multiple and single helicity fields on the pedestal dynamics.

We should point out that the magnetic data alone does not prove that island dynamics (penetration and screening) contribute to the pulsating behavior of the pedestal. The pulsations could in principle be due to the intermittency of the grassy-ELMs and the magnetic response could simply be an indicator of pedestal transport changes rather than a cause of the pedestal change. The key evidence against such a hypothesis is that the inter-ELM heat flux is highest when the grassy-ELMs are mitigated (see yellow band in Fig. 24(a)), so that some other mechanism must be producing the enhanced transport during the intervals where the grassy-ELMs are mitigated. But, it may still be argued that the mitigated grassy-ELMs merge into one big heat pulse that makes it difficult to differentiate the inter-ELM from the grassy-ELM heat flux. The key evidence against this hypothesis is that the grassy-ELM frequency peaks at ≈ 800 Hz during the mitigation phase compared to 12 kHz for the IR camera sample rate. A close inspection of the heat flux trace in Fig. 24(a) at the time indicated by the vertical arrow shows that the inter-ELM heat flux

in the grassy-ELM mitigated phase can indeed be resolved and is significantly higher than the inter-ELM heat flux during strong grassy-ELMs. Thus, the evidence from the heat flux data indicates that the pedestal pulsations are not a consequence of the intermittent behavior of the grassy-ELMs. Instead, some other mechanism is raising the heat flux during the period of grassy-ELM mitigation. The fact that the resonant field penetration of the $n=3$ RMP at the $14/3$ rational surface is predicted to be strongest at the time of grassy-ELM mitigation is consistent with the known effects of resonant fields. These effects include the flattening of the pressure profile near the $q=14/3$ rational surface, the consequent constriction of the pedestal width, the increase in pedestal transport and the increase of the toroidal velocity in the co- I_p direction due to magnetic braking (i.e., reduction of $|\omega_{\text{ExB}}|$). The mitigation of the grassy-ELMs follows from the stabilizing effect of the increased transport (and heat flux) induced by $n=3$ RMP, as shown in the ELITE analysis in Fig. 27.

A further support for grassy-ELM mitigation by $n=3$ resonant field penetration is that the toroidal rotation increases across the edge of the plasma when the flux of heat and particles to the divertor is increasing. By comparing the toroidal rotation (Fig. 25(d)) and density (Fig. 25(b)) profiles during ELM mitigation (red curves) at the top of the pedestal, the edge momentum is clearly increasing as the thermal and particle transport is increasing. Normally we would expect enhanced momentum transport to accompany enhanced particle and thermal transport. However, the edge momentum increase is consistent with the co- I_p torque due to resonant field penetration in a region where the radial electric field is negative before penetration [9]. An alternative hypothesis to explain the increase in momentum is that the grassy-ELMs are very efficient in transporting momentum, so that the mitigation of the grassy-ELMs leads to a strong increase in the edge momentum. The difficulty of this hypothesis is immediately seen by looking again at the data in Fig. 23(c), (e) in the time window between the red and blue bands. In that interval, there is a precipitous drop in the toroidal rotation at $\psi_N \approx 0.92$ before the appearance of significant grassy-ELM activity. This drop in the toroidal rotation before the onset of grassy-ELMs is more easily seen in the preceding pulse at around 3580 ms. Thus, while the grassy-ELMs must have an effect on momentum transport, it is clear that a large fraction of the velocity reduction near the pedestal top is unrelated to the grassy-ELMs. In contrast, the reduction in the rotation velocity at the top of the pedestal is entirely consistent with the screening (loss of penetration) of the $n=3$ resonant field.

An important question is whether the trend of the heat flux at the inner strike point during the pulsations is representative of the heat flux at the outer divertor. As discussed earlier, reliable IR measurements at the outer strike point are not generally available. However, there are intervals in these discharges when the outer strike does become visible to the IR camera. While we are cautious not to interpret such measurements quantitatively, the data from the outer strike point is in good qualitative agreement with the behavior of the heat flux at the inner strike. Figure 30 shows an interval in a similar discharge (#171178) to that in Fig. 23 where the outer strike becomes visible for a period of ≈ 400 ms. Figure 30(a) and (b) shows the peak heat flux to the ISP and OSP, respectively. The overall heat flux is higher at the OSP as expected, but the trend is similar to the ISP data; the grassy ELM amplitude is mitigated as the inter-ELM heat flux increases. In the interval shown in Fig. 30, the grassy-ELMs are completely suppressed in the $n=3$ penetration interval, not just mitigated. The phenomenology of the magnetic response and pedestal oscillations in this discharge are identical to the data shown in Fig. 23-28. The complete stabilization of the grassy-ELMs reinforces the hypothesis that cyclic $n=3$ resonant field penetration is the cause of the grassy-ELM mitigation.

5.3 Grassy-ELMs and low- n peeling-ballooning mode stability

Stability studies of the pedestal suggest that the grassy-ELM is associated with the destabilization of high-n ballooning modes [10,12], in contrast to Type-I ELMs that are associated with more of a low-n peeling-ballooning response [17]. Here we present the hypothesis that the grassy-ELMs are instead a different nonlinear manifestation of the low-n PBMs that are considered responsible for the large amplitude Type-I ELMs. We take this view because for our discharges the pedestal collisionality is in an ITER relevant range $\nu_e^* \approx 0.05 - 0.15$ where low-n ($n < 20$) global PBMs should dominate the ELM dynamics [51].

In order to resolve with high accuracy the profile change during the pedestal pulsations for a high resolution stability analysis, an ensemble average is performed over ten pedestal pulsations for the discharge in Fig. 30 at the maximum and minimum of the grassy-ELM activity. Figure 31 shows an overlay of the two profiles after ensemble averaging, where red is associated with grassy-ELM mitigation and blue is taken during strong grassy-ELM activity. The profiles with strong grassy-ELMs (blue) show an inward radial shift relative to the stable (red) profiles. Also seen is a clear flattening in the middle of the pedestal density profile during grassy-ELMs ($\psi_N \approx 0.95$ in Fig. 31(c)). The flattened region coincides with low ExB shear in Fig. 31(e); the ExB shearing rate γ_{ExB} exhibits a substantial reduction over an extended region in the middle of the pedestal during the grassy-ELM phase of the discharge. The flattening in the density profile and inward shift of the pedestal could be due to magnetic island formation, but the difficulty of this hypothesis is that the ω_{ExB} is very large in this region, which should produce strong screening (Fig. 31(f)).

The ideal MHD ELITE analysis is used to assess the PBM stability of the pedestal for the two sets of profiles in Fig. 31. Figure 32 shows the stability contours plotted against edge current and average edge pressure gradient for the grassy-ELM phase (Fig. 32(a)) and for the suppressed phase (Fig. 32(b)). The shaded oval regions indicate the edge current and pressure gradient within experimental uncertainties. Several features stand out from this analysis. First, during the grassy-ELM phase (Fig. 32(a)), the average pedestal gradient and edge current is lower compared to the mitigated phase in Fig. 32(b). Second, the pedestal in the grassy-ELM phase is closer to the low-n PBM stability boundary than in the mitigated phase, as can be seen by the overlap of the blue oval with the unstable boundary. Third, the stable region opens up in the direction of the dashed black arrow in Fig. 32(a), revealing possibility to access stable high-pressure operation in the grassy-ELM regime.

The key take away from this stability analysis is that the grassy-ELM pedestal is closer to the low-n PBM stability boundary than the suppressed profile, consistent with the ELITE analysis in Fig. 27. From the ELITE analysis the least stable modes for both cases are in the range of low toroidal mode number, peaking in the range $n=5-10$. Figure 33 shows the linear growth rate from ELITE for the grassy-ELM phase of the discharge up to $n=50$. The dashed curve is the stability analysis for the actual experimental profile and the solid curve is for an unstable profile at the top end of the blue oval region in Fig. 32(a). The dominant radial eigenmodes are in the range $n=5-10$ and the radial structure of the $n=10$ and $n=6$ modes are shown in Fig. 33(b), (c). The eigenmodes have some localization to the region of weak magnetic shear near the top of the pedestal. Both in Fig. 27 and in Fig. 32 the main result is that grassy-ELMs appear as the pedestal approaches the low-n PBM stability boundary. This is analogous to the identification of the low-n Edge Harmonic Oscillation (EHO) as a nonlinear manifestation of low-n PBMs driven and regulated by ExB shear [52].

The ELITE analysis of PBM stability shows a monotonically decreasing growth rate up to $n=50$ and calculations have been performed up to $n=90$. Thus we are confident that for these DIII-D plasmas there is no basis within the context of ideal-MHD to claim that high-n ballooning modes play an important

role in these instabilities. Of course, at high- n the ideal MHD treatment is no longer valid. Extensive work has been done showing that an important instability limiting the pedestal pressure gradient is the kinetic ballooning mode (KBM) [53]. Therefore it should be necessary to use global kinetic models to assess the any role of high- n ballooning modes in ELM dynamics [35,54].

Finally, we address the flattening of the density profile in the middle of the pedestal during grassy-ELMs in Fig. 31. From the ELITE analysis we claim that unstable low- n PBMs are most likely the cause of grassy-ELMs and that the real difference between Type-I and grassy-ELMs is the nonlinear dynamics of the same underlying instability. If this claim is correct then from the radial eigenmode structure in Fig. 33 it is difficult to see how such a localized region of density flattening in Fig. 31(b) can occur. On the other hand, at high- n we know that weak ExB shear is destabilizing to electrostatic instabilities. It has recently been speculated that in the case of wide H-mode pedestals, the ExB shearing rate may not be sufficient to suppress electrostatic instabilities [55]. Based on the EPED model, the pedestal width is predicted to increase as $\sqrt{\beta_{p,ped}}$ where $\beta_{p,ped}$ is the poloidal beta at the top of the pedestal. As the poloidal beta increases, the pedestal width will continue to increase, creating conditions where the width of the region near zero ExB shear becomes large enough to allow long wavelength electrostatic instabilities to occur. This could lead to flattening of profiles in the middle of the pedestal where the ExB shearing rate goes through zero, and possibly explain the flattening observed in our data. If so then the enhanced transport in the middle of the pedestal may play an important role in further expanding the width of the pedestal and creating the conditions for grassy-ELMs to dominate over the Type-I ELMs. The beneficial effects of a wide pedestal have been discussed in the literature within the context of the EPED model [14] and also in the identification of new plasma regimes that clearly exceed the pedestal width predicted by EPED [28,56]. Our observations in the RMP grassy-ELM regime add to the growing body of data on wide pedestal regimes in fusion plasmas.

It is important to point out that the grassy-ELMs may also be relevant to the ITER baseline. Till now we have referred to the grassy-ELMs in the context of high beta poloidal plasmas in DIII-D relevant to the ITER steady-state mission. However, if the two-step pedestal is the result of the breakdown of ExB shear suppression of long wavelength electrostatic turbulence in the middle of the pedestal then it should be interesting to determine whether such a breakdown can occur in the center of the pedestal in ITER $Q_{DT}=10$ plasmas. Such a breakdown of shear suppression may occur at low ρ^* [55] and may not require high beta poloidal conditions. Such a two-step pedestal may create the conditions where the Type-I ELMs are less dominant than the grassy-ELMs, as observed in DIII-D. Together with the addition of RMPs, there is a possibility that the ITER $Q_{DT}=10$ plasmas could operate in a robust grassy-ELM regime. An important next step calculation will be to perform nonlinear gyrokinetic simulations using EPED model predictions of the ITER pedestal profile to predict the characteristics of electrostatic turbulence in the middle of the pedestal.

6. Plasma rotation and the RMP grassy ELM regime

The torque scan data from Sec. 2, Fig. 7 shows that the decrease of the toroidal rotation does not adversely affect the grassy-ELM behavior of the plasma. The insensitivity of the radial electric field to rotation in the pedestal is unlike the ITER baseline plasmas where rotation can significantly affect ELM suppression [6]. Figure 34(a), (b) and (c) display the edge electron pressure, total plasma pressure and toroidal rotation velocity, respectively, during the interval from 2400 ms to 2700 ms for the plasma in Fig. 7. The toroidal rotation velocity shows a large, order unity, variation in the edge region when the neutral beam torque is

reduced from ≈ 3 Nm to ≈ 0.7 Nm. The effect of the rotation change is not particularly noticeable in ω_{ExB} , and $\omega_{e,i}$ where $\omega_{e,i} = \omega_{*e,i} + \omega_{\text{ExB}}$. It is interesting that the ion perpendicular flow is close to zero near the top of the pedestal throughout the torque ramp, but the ExB flow and the electron perpendicular flow are quite far from zero. At the top of the pedestal (vertical dashed line near $\sqrt{\psi_s} \approx 0.9$), there is barely a noticeable effect of the change in rotation on the key parameters associated with magnetic island formation, consistent with the much larger contribution of the pressure gradient to the ω_{ExB} , and $\omega_{e,i}$ in these plasmas. [Figure 35](#) underscores this point by showing some key profiles at the start and end of the torque ramp. The ExB frequency does intercept zero near $\rho \approx 0.84$ before the torque ramp but by the end of the torque ramp $\omega_{\text{ExB}} = 0$ moves further away from the pedestal. The profiles for the ion and electron diamagnetic frequency show their dominant contributions to $\omega_{e,i}$ relative to the ExB rotation.

The main conclusion we can draw from the torque scan data is that rotation is not a significant contributor to the key frequencies associated with the presence of driven islands at the top of the pedestal, due to the weak $V \times B$ contribution to the ion and electron perpendicular flows. This is quite different from the ITER-baseline where the $V \times B$ contribution to the electric field and ion/electron flow at the top of the pedestal is comparable to the pressure gradient term. However, we should be cautious to conclude that there can be no islands at the top of the pedestal because of the negative value of the $\omega_{e,i}$ or ω_{ExB} in the torque ramp data. The difficulty of inferring the presence of islands solely from estimates of the plasma flows is that driven magnetic islands can occur over a range of plasma flow frequencies depending on the nonlinear balance between magnetic braking and flow screening, as noted earlier. While linear MHD theory is useful for gaining insight, it is rapidly reaching the end of its usefulness in the study of RMP field effects in the pedestal. Validated fully nonlinear treatments of resonant field penetration are now required to properly address the competition between flow screening and resonant field penetration in realistic plasma conditions.

7. Discussion

Small ELMs have been observed in many disparate conditions in tokamaks. The first evidence for the suppression of Type-I ELMs was achieved in a high collisionality low beta discharge with small ELM-like bursts in low- δ DIII-D [4] and later in AUG [57] plasmas. More recently, a small ELM regime with $n=2$ RMPs was achieved at ITER-relevant low collisionality in AUG ([Fig. 2\(a\)](#) in [24]). Grassy-ELMs were first identified and named on DIII-D to denote small ELMs in high beta poloidal plasmas [10] and they were subsequently explored in great detail in JT60-U where they have been attributed to high- n ballooning modes in the pedestal [11,12]. Other small ELM regimes have been identified and given various labels such as Type-II through to Type-V ELMs in a variety of pedestal conditions [58]. Regardless of beta or collisionality, all of these regimes have a striking similarity in the phenomenology of these small ELMs. This similarity raises the possibility that all these regimes are manifestations of the same underlying instability. However, we should be careful not to associate phenomenological similarity with actual equivalence of the underlying physics because in higher density (and, hence, collisionality) scenarios these small ELMs are less likely to be linked with peeling mode activity. Nonetheless, the proximity of the large and small ELMs to the low- n PBM stability boundary in our plasmas suggests that the peeling instability is linked to both phenomena. A key question then is why such modes sometimes saturate at low amplitude producing grassy-ELMs and other times produce the large Type-I ELMs under very similar pedestal conditions.

The Edge-Harmonic-Oscillation (EHO) in low collisionality Quiescent H-mode plasmas is qualitatively different from the small ELMs studied here, however the pedestal in the QH-mode also resides near to the low- n PBM stability boundary [52] and theoretical analysis suggests that the EHO is a low- n PBM [38]. On occasions the Type-I ELMs and the EHO can even coexist. In the same manner, the pedestal in the grassy-ELM regime resides close to the low- n peeling-ballooning stability boundary and, in the absence of the RMP, both types of ELMs also coexist. This may indicate that the difference between the large and small ELMs is due to a secondary instability producing explosive growth of the former and weak saturation of the latter rather than any fundamental difference in the underlying linear instability [59]. While significant progress has been made in characterizing pedestal linear stability [54], much work remains in understanding the nonlinear dynamics of MHD pedestal instabilities, particularly at low collisionality.

Given that the low collisionality boundary of the peeling-ballooning mode also coincides with the most virulent form of edge instability, the Type-I ELM, the great challenge is to find some way to select the less stable weakly saturated mode in a reliable and reproducible manner. In this paper we have shown that the addition of small amplitude RMPs in the ITER shape and collisionality can be effective in creating robust access to pure grassy-ELM behavior in high beta poloidal plasmas. To be clear, grassy-ELM conditions have been achieved on DIII-D and elsewhere without RMPs, however the robust access to this mitigated grassy-ELM regime, absent of Type-I ELMs in reactor relevant conditions of ITER shape, rotation, collisionality, and steady-state reactor-relevant q_{95} , is a key quality of the plasmas explored in our present study.

Another interesting attribute of the RMP grassy-ELM regime in DIII-D is the onset of pedestal pulsations observed at the lowest range of q_{95} (≈ 5.3). The pulsations are characterized by periodic (≈ 40 ms) oscillations in the pedestal rotation, pressure and width and are correlated with cyclic variations in the grassy-ELM mitigation. We have no clear understanding of the precise conditions for these pulsations to occur, however there is strong evidence that their presence is associated with the cyclic penetration and screening of resonant fields. These pulsations have been beneficial in developing new insights on the stability of the grassy-ELMs and on understanding the role of resonant fields in affecting pedestal transport and grassy-ELM mitigation. The grassy ELMs are strongest during the phase of the pedestal cycle that is closest to the low- n ($n = 5-10$) low collisionality PBM stability boundary calculated using the ELITE code, which occurs when the pedestal is widest. The grassy-ELMs are weakest in the phase of the cycle when the pedestal is most stable to the low- n PBMs, which occurs when the pedestal is narrowest. On occasions the grassy-ELMs are fully suppressed in the most stable phase of the pedestal cycle. The naturally occurring dynamical variation of the pedestal provides useful insight into the stability properties of the grassy-ELMs that is not available from the analysis of stationary pedestal conditions. However, for the robust control of Type-I and grassy-ELMs we need to better understand the dynamics of the pedestal pulsations and develop methods for their avoidance.

By careful analysis of the edge profiles, a flat spot was identified in the density profile in the middle of the pedestal during the grassy-ELMs, near the zero in the ExB shear. We consider it unlikely that low- n PBMs are responsible for the narrow region of density flattening due to the large radial extent of the theoretical mode structure. Understanding this flattening will be important because it contributes to the widening (perhaps most of the widening) of the pedestal relative to EPED model predictions. We proposed that the flattened region could be due to electrostatic instabilities destabilized near the region where the ExB shear goes through zero. The grassy-ELMs could be a consequence rather than a cause of this flattening. This could be good news for ITER $Q_{DT}=10$ plasmas because the flattening of the profile in

the middle of the pedestal will move the top of the pedestal inward, which can be stabilizing for the Type-I ELMs and destabilizing for the grassy-ELMs. Such a breakdown of ExB shear suppression of long wavelength turbulence may occur at low ρ^* as suggested elsewhere [55] and may therefore not require high beta poloidal conditions in ITER.

Finally, we observed that these plasmas strongly amplify edge resonant magnetic perturbations. The natural amplification of the external field by the plasma appears beneficial for ELM suppression/mitigation and presents an opportunity for further optimization of 3D fields for high beta steady-state tokamaks. Based on the validation of the plasma response model (GPEC), the next step can be taken to design optimized 3D field coils that couple most effectively to these high poloidal mode number perturbations.

8. Summary

Resonant magnetic perturbations ($n=3$ RMPs) have been used to eliminate large amplitude ELMs and mitigate grassy-ELMs in wide-pedestal DIII-D plasmas relevant to the ITER steady-state mission. Fully non-inductive discharges with the ITER shape and collisionality ($\nu_e^* \approx 0.05-0.15$) are routinely achieved in DIII-D with $n=3$ RMPs. The residual grassy-ELMs are mitigated relative to grassy-ELMs without the RMP and deliver a peak heat flux to the divertor that can be as low as 1.2x the inter-ELM heat flux in plasmas with sustained high H-factor ($H_{98y2} \approx 1.1-1.3$). The RMP grassy-ELM regime is associated with wide a staircase pedestal; the pedestal density exhibits a flat region near the zero in the ExB shear that contributes to the wide pedestal observed in these plasmas. The mitigated grassy-ELMs can reduce the peak heat flux to the divertor relative to unmitigated grassy-ELMs, which is beneficial for divertor operation in ITER and future reactors. The operating window for the RMP grassy-ELM regime is in the range required for a steady-state tokamak reactor, such as q_{95} between 5.3 and 7.1, and for co- I_p neutral beam torque below 1 Nm. Only small amplitude RMPs ($\delta B_{\text{vac}}/B \approx 1 \times 10^{-4}$) are necessary to access this regime, consistent with the large amplification of the RMP by the plasma, detected using magnetic sensors. Ideal MHD modeling is in quantitative agreement with the amplitude and poloidal structure of the plasma response to the $n=3$ RMP and reveals that the existing internal coil (I-coil) design is inefficient for coupling to the relevant stable edge modes in these plasmas. This suggests that the coil design can be substantially improved in order to couple more effectively to higher edge poloidal mode numbers in future steady-state reactors. Naturally occurring slow (≈ 40 ms) cyclic changes in the width, height and toroidal rotation velocity in the pedestal are observed in plasmas with static $n=3$ RMPs. Correlated changes are observed in the plasma magnetic response during these pulsations, indicative of a dynamic competition between resonant field penetration and flow screening of resonant fields, based on resonant field calculations using single fluid extended MHD model (M3D-C¹). The level of grassy-ELM mitigation is highly variable during these pulsations whereas it is important to mitigate the grassy-ELMs in a reliable and predictable way. Stability analysis during the pedestal cycles reveal that the grassy-ELMs are strongest during the phase when the pedestal is closest to the low- n (and low-collisionality) side of the PBM stability boundary. In contrast, the grassy-ELMs are strongly mitigated, and sometimes completely suppressed, during the phase when the pedestal is deeper in the stable region for PBMs. This correlation suggests that grassy-ELM stability is linked to low- n PBM stability and there is no evidence for the role of high- n instabilities in grassy-ELMs based on ELITE code calculations. While the pulsation are useful for gaining insight on the stability of the grassy-ELMs, understanding and controlling the pulsations will be essential for achieving reliable and robust control of pedestal transport and ELM amplitude. The use of low amplitude edge-resonant magnetic perturbations to achieve mitigated grassy-ELM operation in fully noninductive plasmas relevant to the ITER steady-state mission suggests that further improvements can be made to the steady-state tokamak concept by optimizing the design of 3D fields in high beta

poloidal plasmas. In addition, if a two-step pedestal structure naturally forms in ITER $Q_{DT}=10$ plasmas near where the ExB shear crosses zero, then it may be possible to access a similar RMP grassy-ELM regime in high current ITER DT plasmas where strong ELM mitigation is essential.

Acknowledgements

The first author thanks Richard Fitzpatrick for valuable discussions. This work is supported by the U.S. Department of Energy, Office of Fusion Energy Science, under DOE contract # DE-AC02-09CH11466, # DE-FC02-04ER54698, DE-AC52-07NA27344, DE-FG02-07ER54917, DE-FG02-04ER54761, DE-FC02-04ER54698 and the General Atomics Postdoctoral Research Participation Program administered by ORAU. The experiments described herein were performed on the DIII-D National User Facility operated by General Atomics in San Diego, CA for the U.S. Department of Energy. The DIII-D data shown in this paper can be obtained in digital form by following the links at <https://fusion.gat.com/global/D3D-DMP>.

Disclaimer

This report was prepared as an account of work sponsored by an agency of the United States Government. Neither the United States Government nor any agency thereof, nor any of their employees, makes any warranty, express or implied, or assumes any legal liability or responsibility for the accuracy, completeness, or usefulness of any information, apparatus, product, or process disclosed, or represents that its use would not infringe privately owned rights. Reference herein to any specific commercial product, process, or service by trade name, trademark, manufacturer, or otherwise, does not necessarily constitute or imply its endorsement, recommendation, or favoring by the United States Government or any agency thereof. The views and opinions of authors expressed herein do not necessarily state or reflect those of the United States Government or any agency thereof.

References

- [1] Loarte A, Lipschultz B, Kukushkin A S, Matthews G F, Stangeby P C, Asakura N, Counsell G F, Federici G, Kallenbach A, Krieger K, Mahdavi A, Philipps V, Reiter D, Roth J, Strachan J, Whyte D, Doerner R, Eich T, Fundamenski W, Herrmann A, Fenstermacher M, Ghendrih P, Groth M, Kirschner A, Konoshima S, Labombard B, Lang P, Leonard A W, Monier-Garbet P, Neu R, Pacher H, Pegourie B, Pitts R A, Takamura S, Terry J and Tsitroni E 2007 Chapter 4: Power and particle control *Nucl. Fusion* **47** S203–63
- [2] Gormezano C, Sips A C C, Luce T C, Ide S, Becoulet A, Litaudon X, Isayama A, Hobirk J, Wade M R, Oikawa T, Prater R, Zvonkov A, Lloyd B, Suzuki T, Barbato E, Bonoli P, Phillips C K, Vdovin V, Joffrin E, Casper T, Ferron J, Mazon D, Moreau D, Bundy R, Kessel C, Fukuyama A, Hayashi N, Imbeaux F, Murakami M, Polevoi A R and St. John H E 2007 Chapter 6: Steady state operation *Nucl. Fusion* **47**:S285-S336
- [3] Brezinsek S, Wiesen S, Harting D, Guillemaut C, Webster A J, Heinola K, Meigs A G, Rack M, Gao Y, Sergienko G, Philipps V, Stamp M F and Jachmich S 2016 Characterisation of the deuterium recycling at the W divertor target plates in JET during steady-state plasma conditions and ELMs *Phys. Scr.* **T167**:014076
- [4] Evans T E, Moyer R A, Thomas P R, Watkins J G, Osborne T H, Boedo J A, Doyle E J, Fenstermacher M E, Finken K H, Groebner R J, Groth M, Harris J H, La Haye R J, Lasnier C J, Masuzaki S, Ohya N, Pretty D G, Rhodes T L, Reimerdes H, Rudakov D L, Schaffer M J, Wang G and Zeng L 2004 Suppression of large edge-localized modes in high-confinement DIII-D plasmas with a stochastic magnetic boundary *Phys. Rev. Lett.* **92** 235003

- [5] Evans T E, Moyer R A, Burrell K H, Fenstermacher M E, Joseph I, Leonard A W, Osborne T H, Porter G D, Schaffer M J, Snyder P B, Thomas P R, Watkins J G and West W P 2006 Edge stability and transport control with resonant magnetic perturbations in collisionless tokamak plasmas *Nat. Phys.* **2** 419–23
- [6] Moyer R A, Paz-Soldan C, Nazikian R, Orlov D M, Ferraro N M, Grierson B A, Knölker M, Lyons B C, McKee G R, Osborne T H, Rhodes T L, Meneghini O, Smith S, Evans T E, Fenstermacher M E, Groebner R J, Hanson J M, La Haye R J, Luce T C, Mordijck S, Solomon W M, Turco F, Yan Z and Zeng L 2017 Validation of the model for ELM suppression with 3D magnetic fields using low torque ITER baseline scenario discharges in DIII-D *Phys. Plasmas* **24**:102501
- [7] Evans T E, Loarte A, Orlov D M, Grierson B A, Knölker M M, Lyons B C, Cui L, Gohil P, Groebner R J, Moyer R A, Nazikian R, Osborne T H and Unterberg E A 2017 ELM suppression in helium plasmas with 3D magnetic fields *Nucl. Fusion* **57** 86016
- [8] Wade M R, Nazikian R, S J, Evans T E, Ferraro N M, Moyer R A, Orlov D M, Buttery R J, Fenstermacher M E, Garofalo A M, Lanctot M A, Mckee G R, Osborne T H, Shafer M A, Solomon W M, Snyder P B, Suttrop W, Wingen A, Unterberg E A and Zeng L 2015 Advances in the physics understanding of ELM suppression using resonant magnetic perturbations in DIII-D *Nucl. Fusion* **55**:023002
- [9] Nazikian R, Paz-Soldan C, Callen J D, Degrossie J S, Eldon D, Evans T E, Ferraro N M, Grierson B A, Groebner R J, Haskey S R, Hegna C C, King J D, Logan N C, McKee G R, Moyer R A, Okabayashi M, Orlov D M, Osborne T H, Park J K, Rhodes T L, Shafer M W, Snyder P B, Solomon W M, Strait E J and Wade M R 2015 Pedestal bifurcation and resonant field penetration at the threshold of edge-localized mode suppression in the DIII-D tokamak *Phys. Rev. Lett.* **114**:105002
- [10] Ozeki T, Chu M S, Lao L L, Taylor T S, Chance M S, Kinoshita S, Burrell K H and Stambaugh R D 1990 Plasma Shaping, Edge Ballooning Stability And ELM Behaviour In DIII-D *Nucl. Fusion* **30** 1425–32
- [11] Kamada Y, Oikawa T, Lao L, Takizuka T, Hatae T, Isayama A, Manickam J, Okabayashi M, Fukuda T and Tsuchiya K 2000 Disappearance of giant ELMs and appearance of minute grassy ELMs in JT-60U high-triangularity discharges *Plasma Phys. Control. Fusion* **42** A247–53
- [12] N. Oyama, Kojima A, Aiba N, Horton L D, Isayama A, Kamiya K, Urano H, Sakamoto Y and Kamada Y 2010 Effects of edge collisionality on ELM characteristics in the grassy ELM regime *Nucl. Fusion* **50**:064014
- [13] Paz-Soldan C, Nazikian R, Haskey S R, Logan N C, Strait E J, Ferraro N M, Hanson J M, King J D, Lanctot M J, Moyer R A, Okabayashi M, Park J K, Shafer M W and Tobias B J 2015 Observation of a multimode plasma response and its relationship to density pumpout and edge-localized mode suppression *Phys. Rev. Lett.* **114**:105001
- [14] Snyder P B, Solomon W M, Burrell K H, Garofalo A M, Grierson B A, Groebner R J, Leonard A W, Nazikian R, Osborne T H, Belli E A, Candy J and Wilson H R 2015 Super H-mode: Theoretical prediction and initial observations of a new high performance regime for tokamak operation *Nucl. Fusion* **55** 83026
- [15] Fitzpatrick R 2012 Nonlinear error-field penetration in low density ohmically heated tokamak plasmas *Plasma Phys. Control. Fusion* **54** 94002
- [16] Fitzpatrick R 2014 Linear and nonlinear response of a rotating tokamak plasma to a resonant error-field *Phys. Plasmas* **21** 92513
- [17] Snyder P B, Wilson H R, Ferron J R, Lao L L, Leonard A W, Mossessian D, Murakami M, Osborne T H, Turnbull A D and Xu X Q 2004 ELMs and constraints on the H-mode pedestal: Peeling-ballooning stability calculation and comparison with experiment *Nucl. Fusion* **44** 320–8
- [18] Park J-K and Logan N C 2017 Self-consistent optimization of neoclassical toroidal torque with anisotropic perturbed equilibrium in tokamaks *Phys. Plasmas* **24**:032505
- [19] Ferraro N M 2012 Calculations of two-fluid linear response to non-axisymmetric fields in

- tokamaks *Phys. Plasmas* **19**:056105
- [20] Moyer R A, Evans T E, Osborne T H, Thomas P R, Becoulet M, Harris J, Finken K H, Boedo J A, Doyle E J, Fenstermacher M E, Gohil P, Groebner R J, Groth M, Jackson G L, La Haye R J, Lasnier C J, Leonard A W, McKee G R, Reimerdes H, Rhodes T L, Rudakov D L, Schaffer M J, Snyder P B, Wade M R, Wang G, Watkins J G, West W P and Zeng L 2005 Edge localized mode control with an edge resonant magnetic perturbation *Phys. Plasmas* **12**:056119
- [21] Evans T E, Burrell K H, Fenstermacher M E, Moyer R A, Osborne T H, Schaffer M J, West W P, Yan L W, Boedo J A, Doyle E J, Jackson G L, Joseph I, Lasnier C J, Leonard A W, Rhodes T L, Thomas P R, Watkins J G and Zeng L 2006 The physics of edge resonant magnetic perturbations in hot tokamak plasmas *Phys. Plasmas* **13**:056121
- [22] Petty C C, Nazikian R, Park J M, Turco F, Chen X, Cui L, Evans T E, Ferraro N, Ferron J R, Garofalo A M, Grierson B A, Holcomb C T, Hyatt A W, Kolemen E, Haye R J La, Lasnier C, Logan N, Luce T C, McKee G R, Orlov D M, Osborne T H, Pace D C, Paz-Soldan C, Petrie T W, Snyder P B, Solomon W M, Taylor N Z, Thome K E, Zeeland M A Van and Zhu Y 2017 Advances in the steady-state hybrid regime in DIII-D – a fully non-inductive, ELM-suppressed scenario for ITER *Nucl. Fusion* **57**:116057
- [23] Snyder P B, Groebner R J, Leonard A W, Osborne T H and Wilson H R 2009 Development and validation of a predictive model for the pedestal height *Phys. Plasmas* **16**:056118
- [24] Suttrop W, Kirk A, Nazikian R, Leuthold N, Strumberger E, Willensdorfer M, Cavedon M, Dunne M, Fischer R, Fietz S, Fuchs J C, Liu Y Q, McDermott R M, Orain F, Ryan D A and Viezzer E 2017 Experimental studies of high-confinement mode plasma response to non-axisymmetric magnetic perturbations in ASDEX Upgrade *Plasma Phys. Control. Fusion* **59**:014049
- [25] Grierson B A, Burrell K H, Nazikian R M, Solomon W M, Garofalo A M, Belli E A, Staebler G M, Fenstermacher M E, McKee G R, Evans T E, Orlov D M, Smith S P, Chrobak C and Chrystal C 2015 Impurity confinement and transport in high confinement regimes without edge localized modes on DIII-D *Phys. Plasmas* **22**:055901
- [26] Solomon W M 2017 DIII-D research advancing the scientific basis for burning plasmas and fusion energy *Nucl. Fusion* **57**:102018
- [27] Fenstermacher M E, Evans T E, Osborne T H, Schaffer M J, Aldan M P, Degrossie J S, Gohil P, Joseph I, Moyer R A, Snyder P B, Groebner R J, Jakubowski M, Leonard A W and Schmitz O 2008 Effect of island overlap on edge localized mode suppression by resonant magnetic perturbations in DIII-D *Phys. Plasmas* **15**:056122
- [28] Chen X, Burrell K H, Osborne T H, Barada K, Ferraro N M, Garofalo A M, Groebner R J, McKee G R, Petty C C, Porkolab M, Rhodes T L, Rost J C, Snyder P B, Solomon W M and Yan Z 2017 Bifurcation of quiescent H-mode to a wide pedestal regime in DIII-D and advances in the understanding of edge harmonic oscillations *Nucl. Fusion* **57** 86008
- [29] Loarte A, Huijsmans G, Futatani S, Baylor L R R, Evans T E E, Orlov D M, Schmitz O, Becoulet M, Cahyna P, Gribov Y, Kavin A, Sashala Naik A, Campbell D J J, Casper T, Daly E, Frerichs H, Kischner A, Laengner R, Lisgo S, Pitts R a. a., Saibene G and Wingen A 2014 Progress on the application of ELM control schemes to ITER scenarios from the non-active phase to DT operation *Nucl. Fusion* **54** 33007
- [30] Xi P W, Xu X Q and Diamond P H 2014 Phase dynamics criterion for fast relaxation of high-confinement-mode plasmas *Phys. Rev. Lett.* **112** 85001
- [31] Huijsmans G T A and Loarte A 2013 Non-linear MHD simulation of ELM energy deposition *Nucl. Fusion* **53**:123023
- [32] Bécoulet M, Orain F, Huijsmans G T A, Pamela S, Cahyna P, Hoelzl M, Garbet X, Franck E, Sonnendrücker E, Dif-Pradalier G, Passeron C, Latu G, Morales J, Nardon E, Fil A, Nkonga B, Ratnani A and Grandgirard V 2014 Mechanism of edge localized mode mitigation by resonant magnetic perturbations *Phys. Rev. Lett.* **113** 8–12
- [33] Orain F, Bécoulet M, Morales J, Huijsmans G T A, Dif-Pradalier G, Hoelzl M, Garbet X, Pamela S, Nardon E, Passeron C, Latu G, Fil A and Cahyna P 2015 Non-linear MHD modeling of edge

- localized mode cycles and mitigation by resonant magnetic perturbations *Plasma Phys. Control. Fusion* **57**
- [34] Willensdorfer M, Cote T B, Hegna C C, Suttrop W, Zohm H, Dunne M, Strumberger E, Birkenmeier G, Denk S S, Mink F, Vanovac B and Luhmann L C 2017 Field-Line Localized Destabilization of Ballooning Modes in Three-Dimensional Tokamaks *Phys. Rev. Lett.* **119** 85002
- [35] Holod I, Lin Z, Taimourzadeh S, Nazikian R, Spong D and Wingen A 2017 Effect of resonant magnetic perturbations on microturbulence in DIII-D pedestal *Nucl. Fusion* **57**:016005
- [36] Xiao W W, Evans T E, Tynan G R and Eldon D 2016 Location of the first plasma response to resonant magnetic perturbations in DIII-D H-mode plasmas *Nucl. Fusion* **56**:064001
- [37] Kamada Y, Takenaga H, Isayama A, Hatae T, Urano H, Kubo H, Takizuka T and Miura Y 2002 Pedestal characteristics and extended high- β p ELMy H-mode regime in JT-60U *Plasma Phys. Control. Fusion* **44** 279–86
- [38] Xu G S, Wan B N, Wang Y F, Wu X Q, Chen X, Martin Peng Y K, Guo H Y, Burrell K H, Garofalo A M, Osborne T H, Groebner R J, Wang H Q, Chen R, Yan N, Wang L, Ding S Y, Shao L M, Hu G H, Li Y L, Lan H, Yang Q Q, Chen L, Ye Y, Xu J C and Li J 2017 $E \times B$ flow shear drive of the linear low-n modes of EHO in the QH-mode regime *Nucl. Fusion* **57** 86047
- [39] Liu F, Huijsmans G T A, Loarte A, Garofalo A M, Solomon W M, Hoelzl M, Nkonga B, Pamela S, Becoulet M, Orain F and Van Vugt D 2018 Non-linear MHD simulations of QH-mode and Type I ELMy H-mode DIII-D plasmas and implications for ITER high Q scenarios *Plasma Phys. Control. Fusion* **60** 14039
- [40] Hubbard A E, Baek S G, Brunner D, Creely A J, Cziegler I, Edlund E, Hughes J W, Labombard B, Lin Y, Liu Z, Marmor E S, Reinke M L, Rice J E, Sorbom B, Sung C, Terry J, Theiler C, Tolman E A, Walk J R, White A E, Whyte D, Wolfe S M, Wukitch S and Xu X Q 2017 Physics and performance of the I-mode regime over an expanded operating space on Alcator C-Mod *Nucl. Fusion* **57** 126039
- [41] Kirk A, Suttrop W, Chapman I T, Liu Y, Scannell R, Thornton A J, Orte L B, Cahyna P, Eich T, Fischer R, Fuchs C, Ham C, Harrison J R, Jakubowski M W, Kurzan B, Pamela S, Peterka M, Ryan D, Saarelma S, Sieglin B, Valovic M and Willensdorfer M 2015 Effect of resonant magnetic perturbations on low collisionality discharges in MAST and a comparison with ASDEX Upgrade *Nucl. Fusion* **55** 43011
- [42] Paz-Soldan C, Nazikian R, Haskey S R, Logan N C, Strait E J, Ferraro N M, Hanson J M, King J D, Lanctot M J, Moyer R A, Okabayashi M, Park J K, Shafer M W and Tobias B J 2015 Observation of a multimode plasma response and its relationship to density pumpout and edge-localized mode suppression *Phys. Rev. Lett.* **114**:105001
- [43] Liu Y, Kirk A and Nardon E 2010 Full toroidal plasma response to externally applied nonaxisymmetric magnetic fields Full toroidal plasma response to externally applied nonaxisymmetric magnetic fields *Phys. Plasmas* **17**:122502
- [44] Park J K, Schaffer M J, Menard J E and Boozer A H 2007 Control of asymmetric magnetic perturbations in tokamaks *Phys. Rev. Lett.* **99**:195003
- [45] Logan N C, Paz-Soldan C, Park J K and Nazikian R 2016 Identification of multi-modal plasma responses to applied magnetic perturbations using the plasma reluctance *Phys. Plasmas* **23**:056110
- [46] Liu Y, Kirk A and Nardon E 2010 Full toroidal plasma response to externally applied nonaxisymmetric magnetic fields *Phys. Plasmas* **17** 1–17
- [47] Paz-Soldan C, Logan N C, Haskey S R, Nazikian R, Strait E J, Chen X, Ferraro N M, King J D, Lyons B C and Park J K 2016 Equilibrium drives of the low and high field side $n = 2$ plasma response and impact on global confinement *Nucl. Fusion* **56**:056001
- [48] Grimm R C, Dewar R L and Manickam J 1983 Ideal MHD stability calculations in axisymmetric toroidal coordinate systems *J. Comput. Phys.* **49** 94–117
- [49] Reimerdes H, Hender T C, Sabbagh S A, Bialek J M, Chu M S, Garofalo A M, Gryaznevich M P, Howell D F, Jackson G L, La Haye R J, Liu Y Q, Menard J E, Navratil G A, Okabayashi M, Pinches S D, Sontag A C, Strait E J, Zhu W, Bigi M, De Baar M, De Vries P, Gates D A, Gohil P,

- Groebner R J, Mueller D, Raman R, Scoville J T and Solomon W M 2006 Cross-machine comparison of resonant field amplification and resistive wall mode stabilization by plasma rotation *Phys. Plasmas* **13**:056107
- [50] In Y, Park J, Jeon Y M, Kim J, Park G Y, Ahn J, Loarte A, Ko W H, Lee H H, Yoo J W, Juhn J W, Yoon S W and Park H 2017 Enhanced understanding of non-axisymmetric intrinsic and controlled field impacts in tokamaks *Nucl. Fusion* **57**:116054
- [51] Snyder P B, Osborne T H, Burrell K H, Groebner R J, Leonard A W, Nazikian R, Orlov D M, Schmitz O, Wade M R and Wilson H R 2012 The EPED pedestal model and edge localized mode-suppressed regimes: Studies of quiescent H-mode and development of a model for edge localized mode suppression via resonant magnetic perturbations *Phys. Plasmas* **19**:056115
- [52] Chen X, Burrell K H, Ferraro N M, Osborne T H, Austin M E, Garofalo A M, Groebner R J, Kramer G J, Luhmann N C, McKee G R, Muscatello C M, Nazikian R, Ren X, Snyder P B, Solomon W M, Tobias B J and Yan Z 2016 Rotational shear effects on edge harmonic oscillations in DIII-D quiescent H-mode discharges *Nucl. Fusion* **56**:076011
- [53] Snyder P B, Groebner R J, Hughes J W, Osborne T H, Beurskens M, Leonard A W, Wilson H R and Xu X Q 2011 A first-principles predictive model of the pedestal height and width: Development, testing and ITER optimization with the EPED model *Nucl. Fusion* **51**:103016
- [54] Hatch D R, Told D, Jenko F, Doerk H, Dunne M G, Wolfrum E, Viezzer E and Pueschel M J 2015 Gyrokinetic study of ASDEX Upgrade inter-ELM pedestal profile evolution *Nucl. Fusion* **55**:063028
- [55] Kotschenreuther M, Hatch D R, Mahajan S, Valanju P, Zheng L and Liu X 2017 Pedestal transport in H-mode plasmas for fusion gain *Nucl. Fusion* **57**:064001
- [56] Osborne T H, Jackson G L, Yan Z, Maingi R, Mansfield D K, Grierson B A, Chrobak C P, McLean A G, Allen S L, Battaglia D J, Briesemeister A R, Fenstermacher M E, McKee G R and Snyder P B 2015 Enhanced H-mode pedestals with lithium injection in DIII-D *Nucl. Fusion* **55**:063018
- [57] Suttrop W, Eich T, Fuchs J C, Günter S, Janzer A, Herrmann A, Kallenbach A, Lang P T, Lunt T, Maraschek M, McDermott R M, Mlynek A, Pütterich T, Rott M, Vierle T, Wolfrum E, Yu Q, Zammuto I and Zohm H 2011 First observation of edge localized modes mitigation with resonant and nonresonant magnetic perturbations in ASDEX upgrade *Phys. Rev. Lett.* **106** 225004
- [58] Leonard A W 2014 Edge-localized-modes in tokamaks *Phys. Plasmas* **21** 1–24
- [59] Cowley S C, Wilson H, Hurricane O and Fong B 2003 Explosive instabilities: from solar flares to edge localized modes in tokamaks *Plasma Phys. Control. Fusion* **45** A31–8

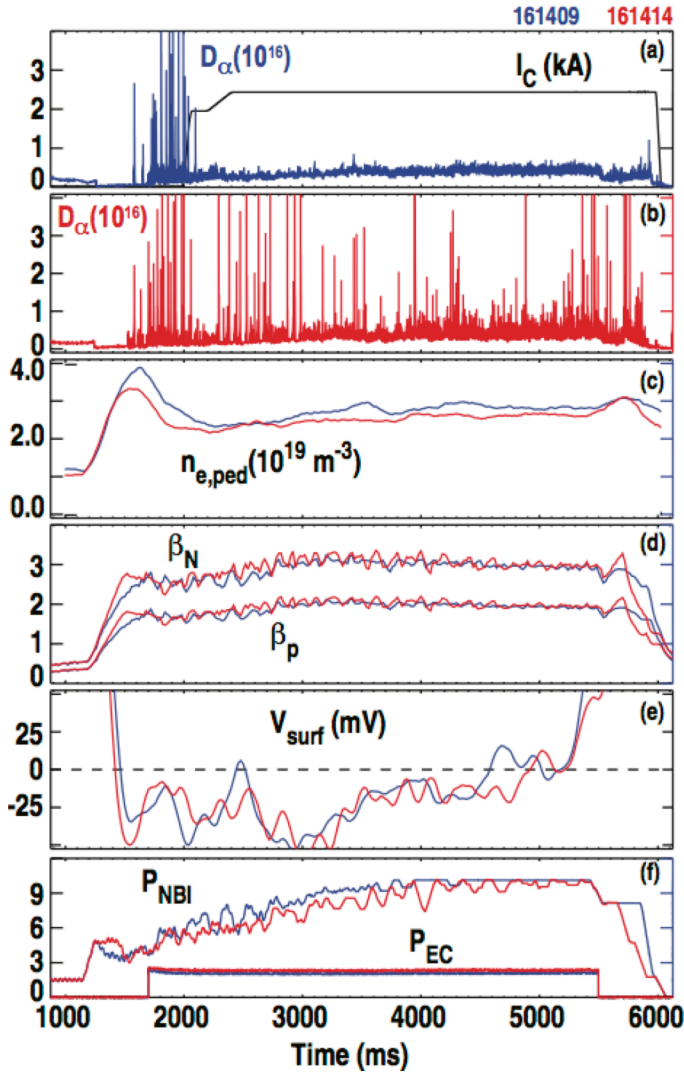


Figure 1. For two fully noninductive plasmas, with (shot #161409) and without (shot #161414) the applied $n=3$ RMP: (a) D_α signal from the inner-strike-point showing controlled grassy-ELMs for the $n=3$ RMP case (blue) with 2.5 kA odd-parity I-coil current (black), (b) D_α signal for the no-RMP case (red) showing mixed ELM activity, (c) pedestal electron density $n_{e,ped}$ for the RMP (blue) and no-RMP (red) plasmas, (d) β_N and β_p , (e) surface voltage V_{surf} , and (f) beam power P_{NBI} and electron cyclotron heating power P_{ECH} . Relevant discharge parameters are: plasma current $I_p=0.95$ MA, toroidal field $B_T=1.7$ T, average triangularity $\delta=0.55$, noninductive fraction $f_{NI}\approx 100\%$, pedestal collisionality $\nu_{e,ped}^*\approx 0.1$, $\beta_N\approx 3$, $\beta_p\approx 2$, $P_{NBI}\approx 6.0$ MW, $P_{ECH}\approx 3$ MW, $H_{98y2}\approx 1.2-1.3$.

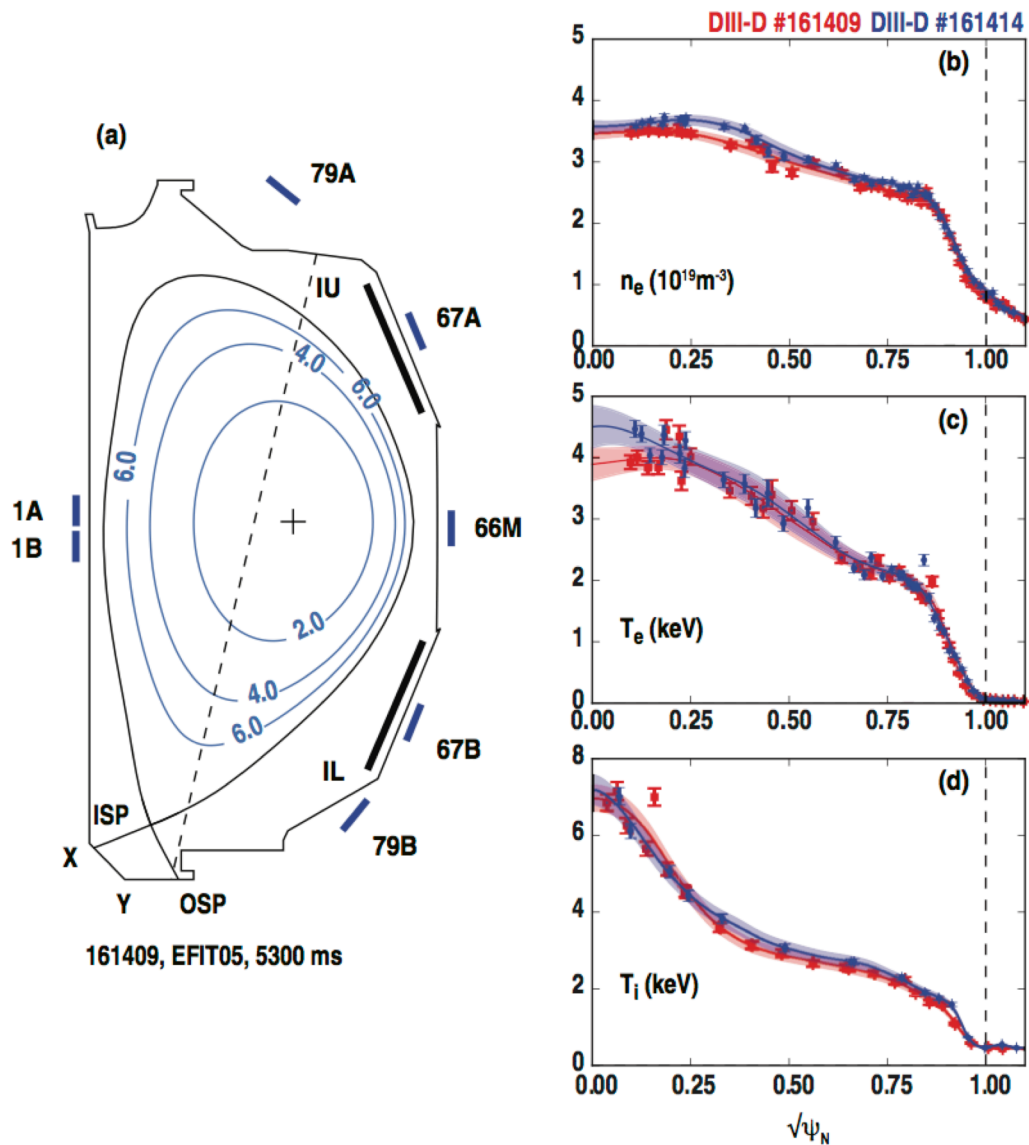


Figure 2. Equilibrium and profiles for plasmas in Figure 1: (a) Plasma boundary shape (black), rational surfaces (blue), location of upper I-coils (IU) and lower I-coils (IL), location of toroidal arrays of magnetic probes including outer midplane array (66M) and center post arrays (1A, 1B), (b) density profile at 4000 ms for no-RMP (red) and RMP grassy-ELM (blue) vs. minor radius ρ , (c) electron temperature, (d) ion temperature. In (a) inner corners of the vacuum vessel are labeled X and Y and the inner/outer strike points of the separatrix in the divertor are labeled ISP and OSP, respectively. The dashed line in (a) is the inner most sightline for the IR camera.

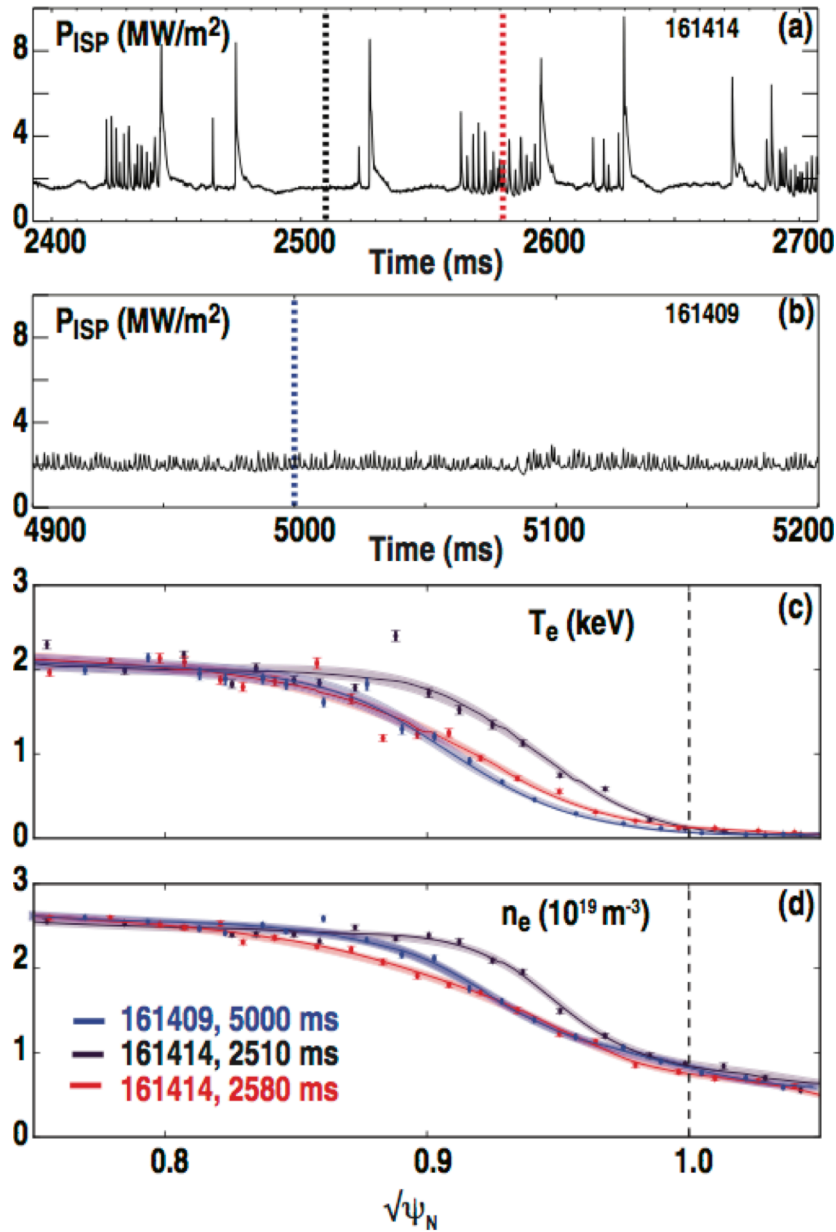


Figure 3. For the plasmas in Fig. 1: (a) IR measured peak heat flux P_{ISP} at inner strike point (ISP), (b) P_{ISP} for RMP grassy-ELM plasma, (c) electron temperature during ELM free phase for no-RMP case at ≈ 2510 ms (black), no RMP grassy-ELM time at ≈ 2580 ms (red) and RMP-grassy phase at ≈ 5000 ms, (d) same as in (c) for electron density profile.

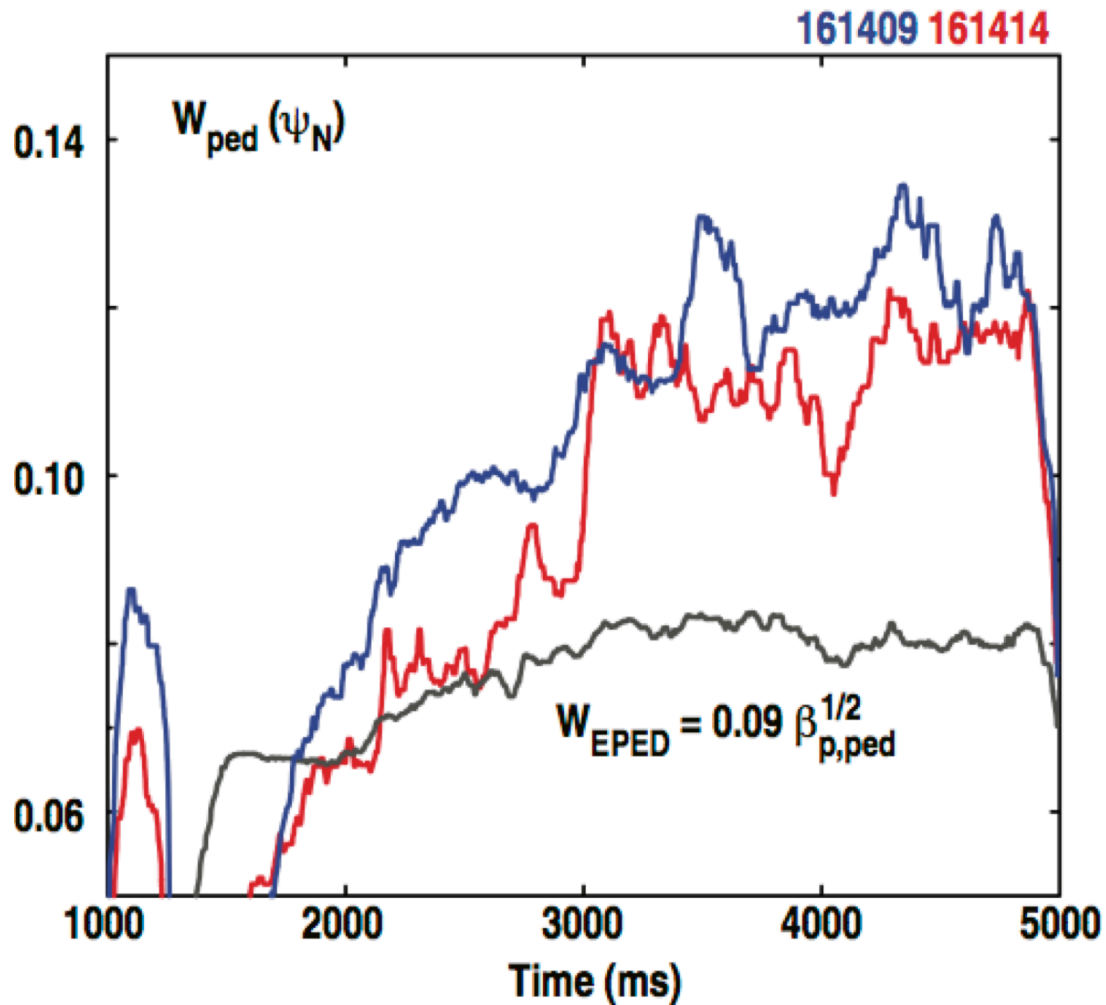


Figure 4. Comparison of pedestal width W_{ped} in normalized poloidal radius (ψ_N) vs. EPED model prediction based on measured pedestal pressure ($W_{EPED}=0.09 \sqrt{\beta_{p,ped}}$) for the two discharges in Fig. 1, one with RMP (blue curve #161409) and without RMP (red curve #161414). The measured width is based on a Tanh fit of the edge electron temperature and density profile measured using Thomson scattering.

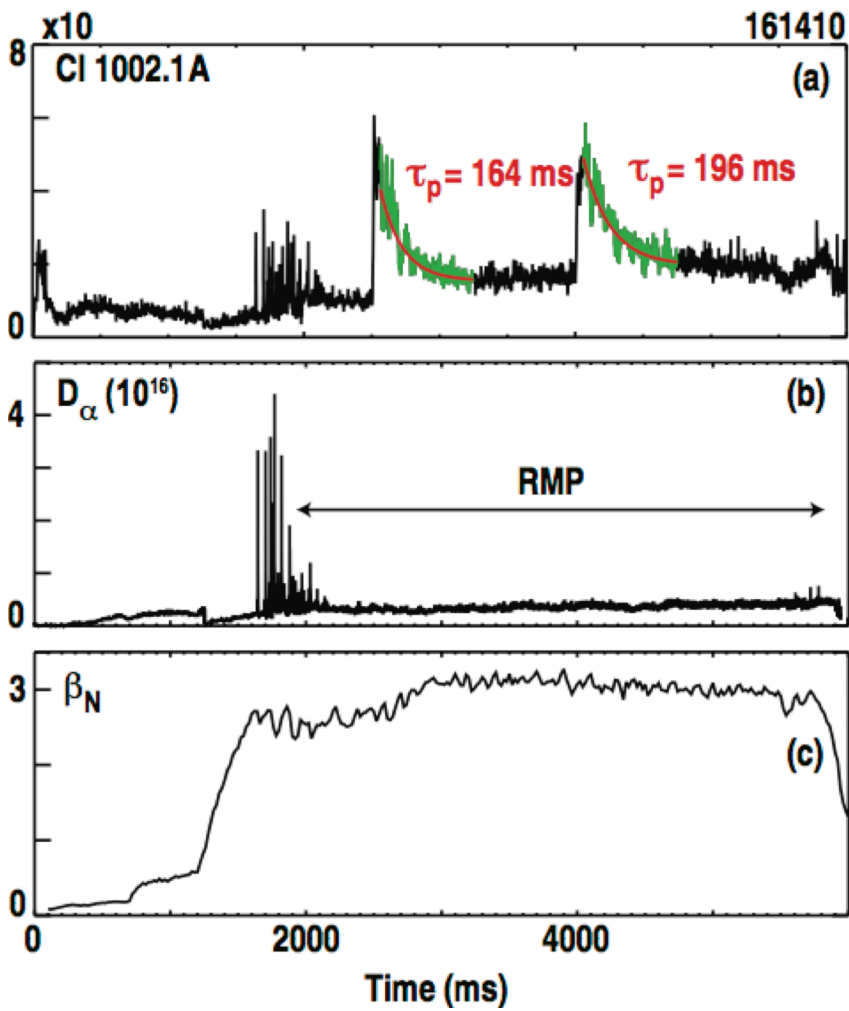


Figure 5. RMP grassy ELM plasma similar to #161409 in Fig. 1: (a) spectroscopic intensity of chlorine 1002.1A line from plasma core with chlorine gas puff (red) showing particle confinement time $\tau_p \approx 180$ ms, (b) D_α signal from ISP showing RMP grassy-ELM phase, (c) β_N .

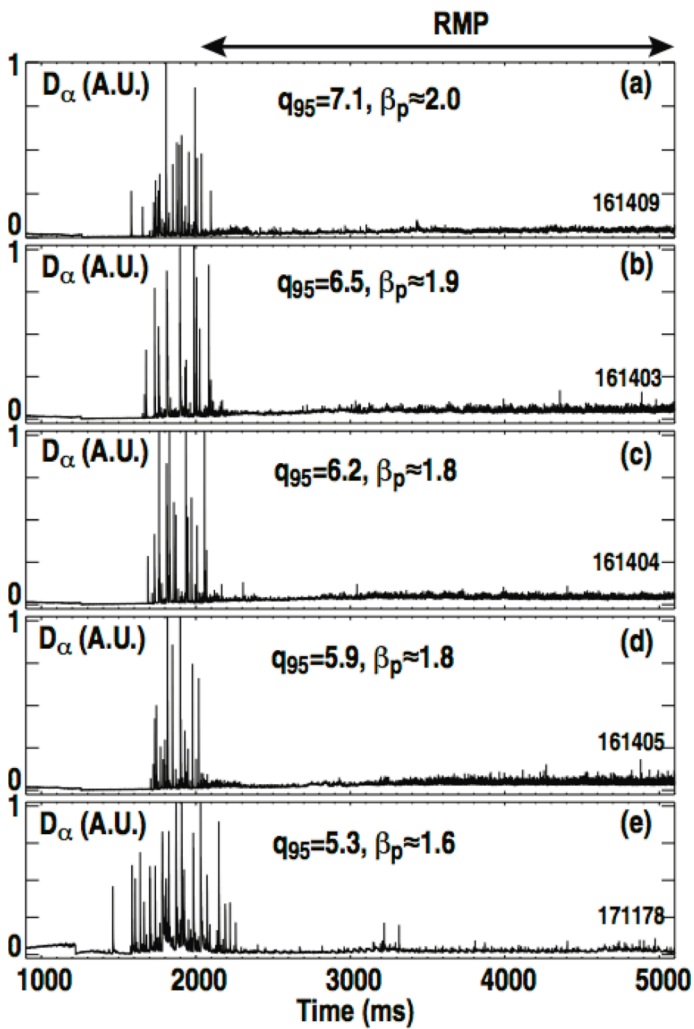


Figure 6. D_α signals for a range of q_{95} with constant I-coil current (2.5 kA odd-parity) showing access to RMP grassy-ELM regime with similar $\beta_N \approx 3$ and (a) $q_{95}=7.1$, (b) $q_{95}=6.5$, (c) $q_{95}=6.2$, (d) $q_{95}=5.9$, (e) $q_{95}=5.3$.

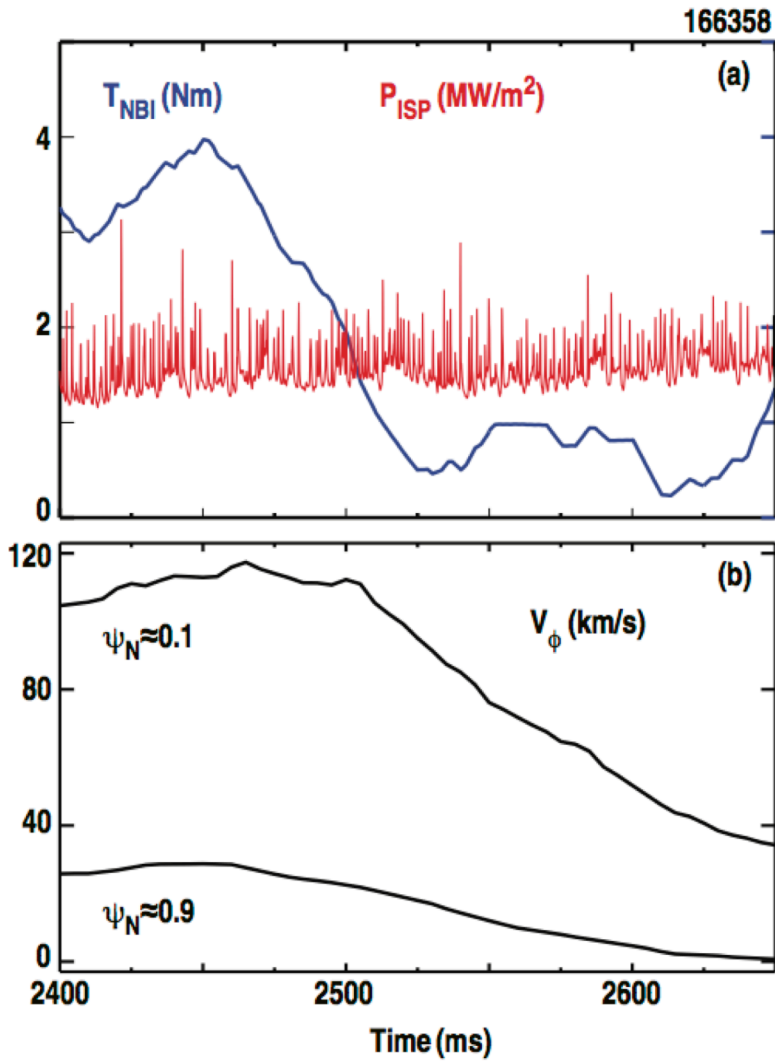


Figure 7: Plasma with 2.5 kA odd-parity RMP. Shown is (a) the peak heat flux at the inner strike point P_{ISP} (red) and injected neutral beam torque T_{NBI} (blue) averaged over 20 ms, and (b) the central and top of pedestal toroidal rotation velocity. Plasma parameters for discharge #166358 are: $q_{95} \approx 6.1$, $\beta_{\text{N}} \approx 2.5$, $\beta_{\text{p}} \approx 1.5$, $R \approx 1.69$ m, $a \approx 0.6$ m, $B_{\text{T}} \approx 1.95$ T, $I_{\text{p}} \approx 0.95$ MA, $P_{\text{NBI}} \approx 6.2$ MW, $P_{\text{ECH}} \approx 2.2$ MW, $T_{\text{e,ped}} \approx 1.2$ keV.

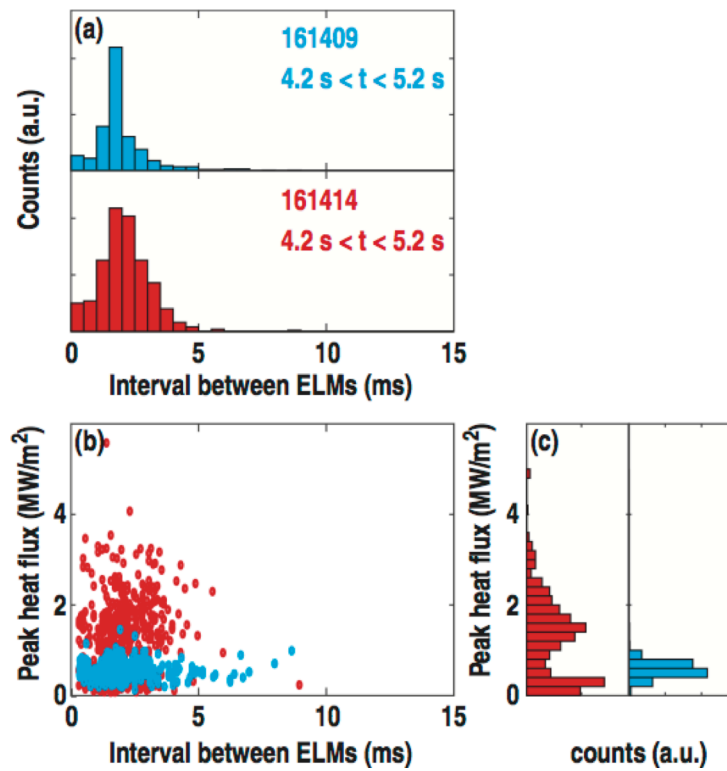


Figure 8. Distribution of ELM peak heat flux on ISP in the RMP grassy-ELM (blue) and no RMP mixed ELM (red) plasmas in Fig. 1: (a) number of ELMs vs. ELM interval, (b) ELM amplitude vs. ELM interval, and (c) number of ELMs vs. ELM amplitude.

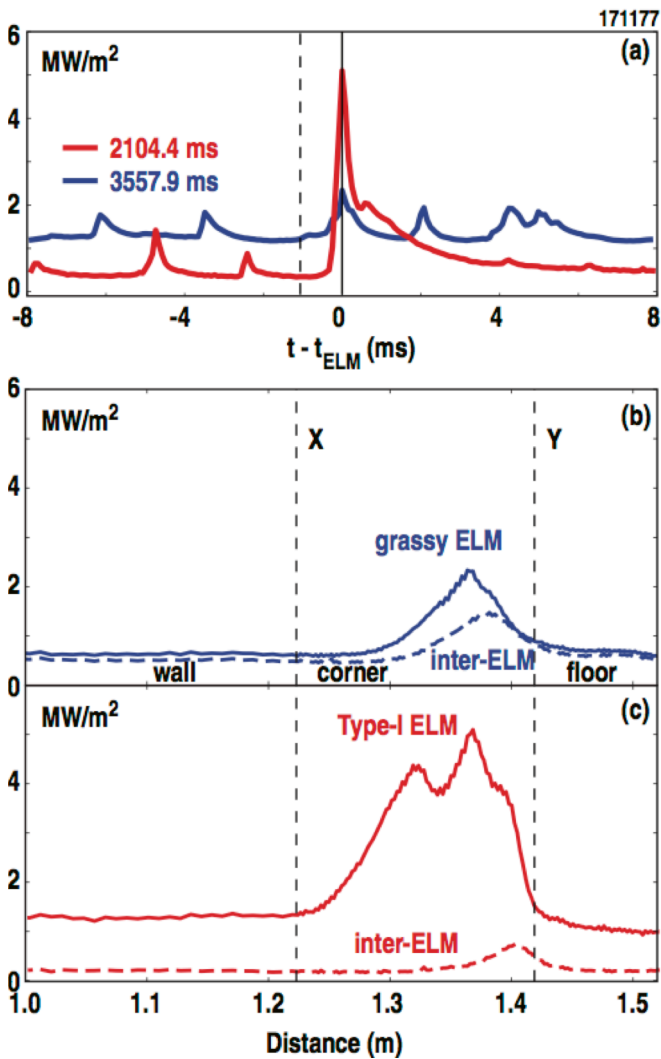


Figure 9. Heat flux at ISP before RMP is applied (red) and during RMP phase (blue): (a) P_{ISP} vs. time, (b) in RMP grassy-ELM phase, heat flux vs. distance along the inner wall 1 ms before ELM (dashed) and during ELM at $\Delta t=0$, (c) in no RMP phase, heat flux vs. distance along the inner wall 1 ms before ELM (dashed) and during ELM at $\Delta t=0$. The locations X and Y correspond to the two lower inner corners of the vacuum vessel in Fig. 2(a). Plasma parameters are the same as for the plasma in Fig. 1 but with $I_p=1.25$ MA, $q_{95}\approx 5.2$, and $\beta_p\approx 1.6$.

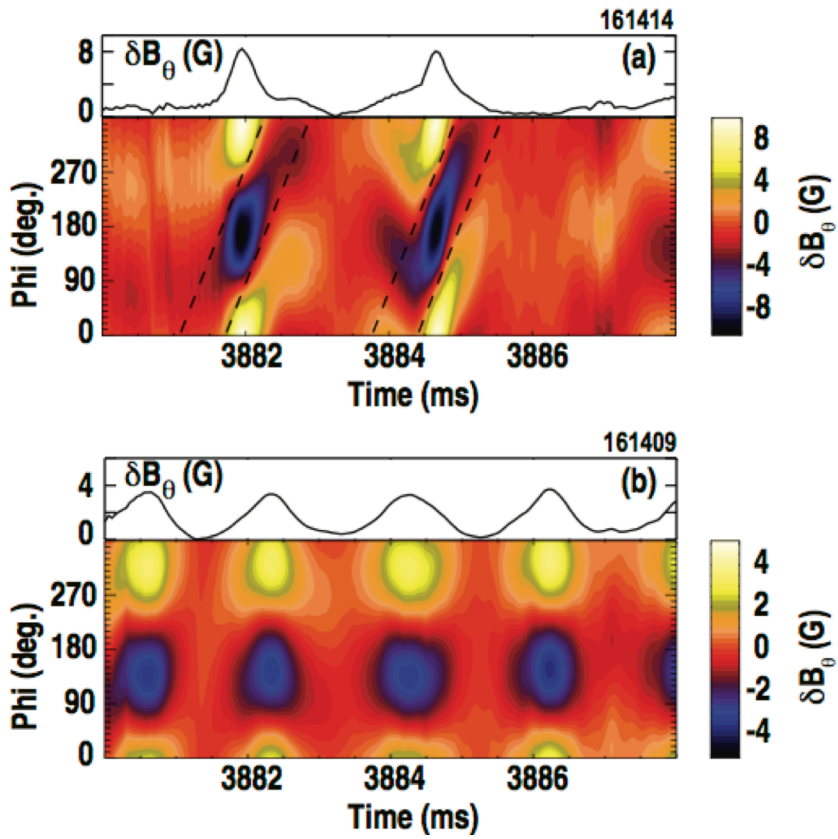


Figure 10. Poloidal magnetic field perturbation for the toroidal mode number $n=1$ measured on the outboard midplane for the plasmas in Fig. 1 with (a) no-RMP and (b) even parity $n=3$ RMP. The dashed lines in (a) indicate mode rotation in the electron diamagnetic drift direction.

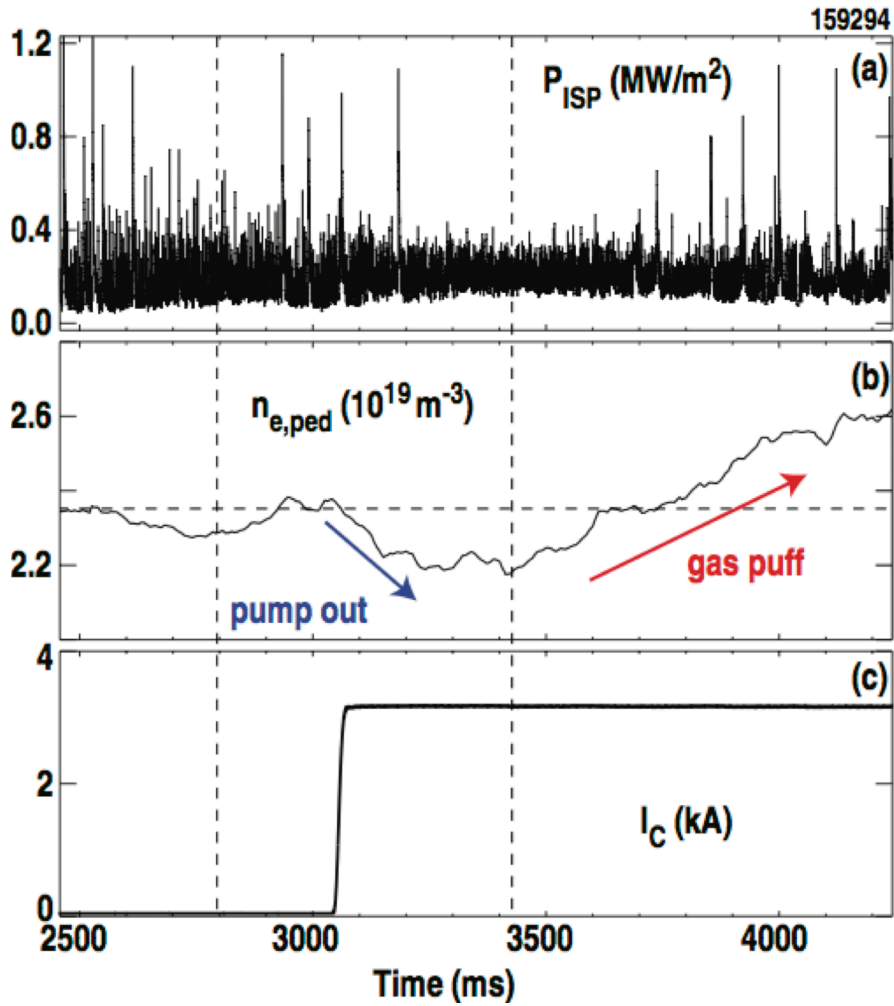


Figure 11. The correlation of pedestal density change with the change in ELM activity for a 3.1 kA $n=3$ upper row RMP: (a) peak heat flux to inner strike point, (b) pedestal density, and (c) I-coil current. Vertical dashed lines show periods of ELM mitigation aligned with minima in $n_{e,ped}$. Plasma parameters for discharge #159294 are: $q_{95} \approx 6.0$, $\beta_N \approx 2.5$, $\beta_p \approx 1.5$, $R \approx 1.69$ m, $a \approx 0.6$ m, $B_T \approx 1.95$ T, $I_p \approx 1.0$ MA, $P_{NBI} \approx 6.2$ MW, $P_{ECH} \approx 2.2$ MW, $T_{e,ped} \approx 1.2$ keV.

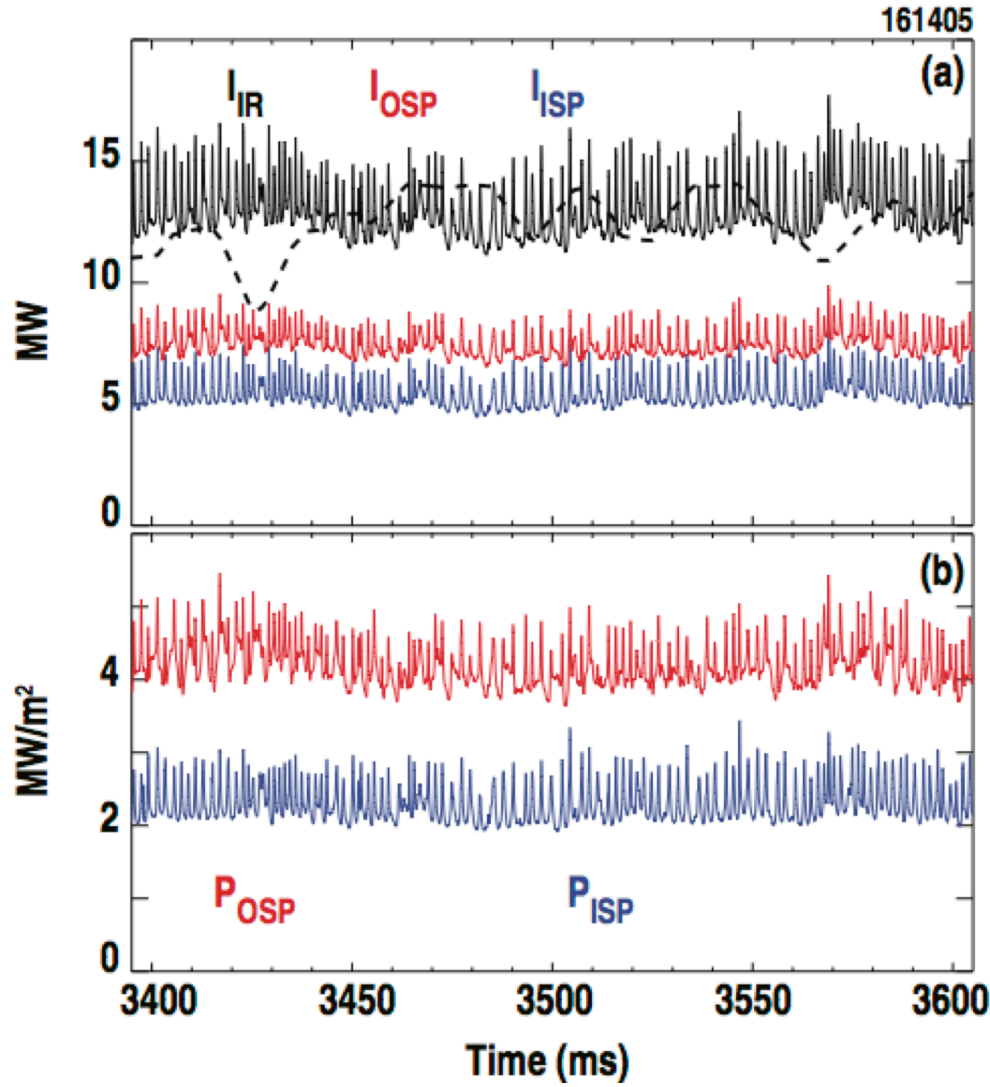


Figure 12. Fully noninductive discharge (#161405) in the ITER shape with 2.5 kA $n=3$ odd-parity RMP. In (a) the IR camera measured thermal intensity at the inner strike point I_{ISP} (blue), outer strike point I_{OSP} (red), the sum of the two I_{IR} (black) and the sum of the neutral beam and ECH power (black dashed); (b) the peak heat flux at the inner strike point P_{ISP} (blue) and outer strike point P_{OSP} (red). Plasma parameters: $q_{95} \approx 6.0$, $\beta_N \approx 3.1$, $\beta_P \approx 1.75$, $R \approx 1.68$ m, $a \approx 0.6$ m, $B_T \approx -1.95$ T, $I_p \approx 1.05$ MA, $P_{NBI} \approx 10$ MW, $P_{ECH} \approx 3.4$ MW.

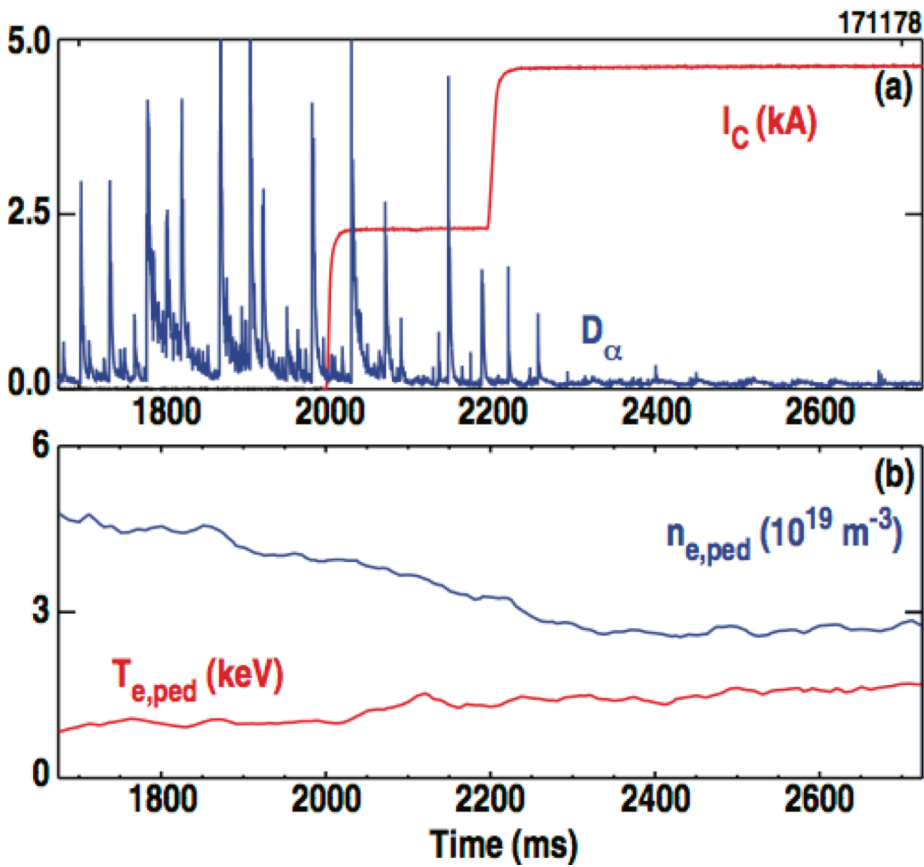


Figure 13. The transition to large-amplitude ELM suppression during the early phase of the discharge (#171178) using a 4.5 kA $n=3$ single upper row of I-coils: (a) $D\alpha$ signal from ISP (blue) and I-coil current (red), (b) electron pedestal density $n_{e,ped}$ (blue) and pedestal temperature $T_{e,ped}$ (red). Plasma parameters in the window of interest: $q_{95} \approx 5.2$, $\beta_N \approx 2.5$, $\beta_p \approx 1.3$, $R \approx 1.67$ m, $a \approx 0.6$ m, $B_T \approx 1.90$ T, $I_p \approx 1.12$ MA, $P_{NBI} \approx 5$ MW, $P_{ECH} \approx 3.4$ MW.

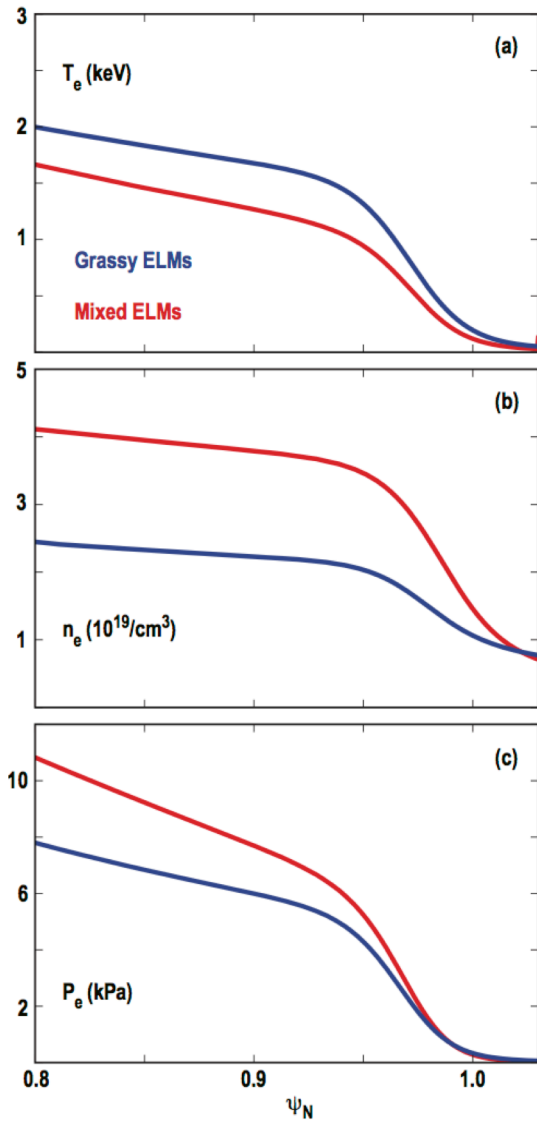


Figure 14. Pedestal profiles during the large amplitude ELMs near 1800 ms (red) and in the large ELM suppressed phase near 2400 ms (blue): (a) electron temperature, (b) electron density, and (c) electron pressure).

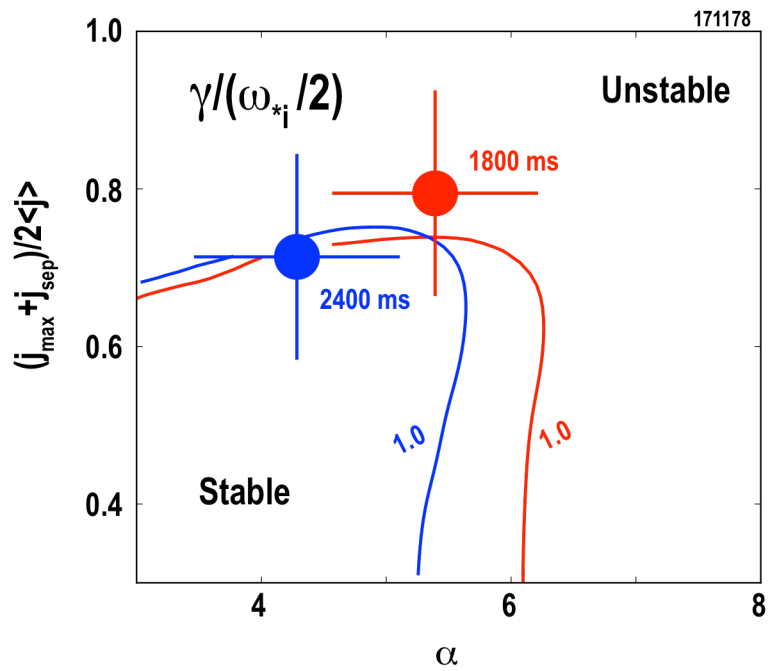


Figure 15. Peeling-Ballooning stability analysis using the ELITE code for the two times in Fig. 14 before the RMP during large amplitude ELMs (red) and the RMP grassy-ELM phase (blue). Solid line is the stability boundary.

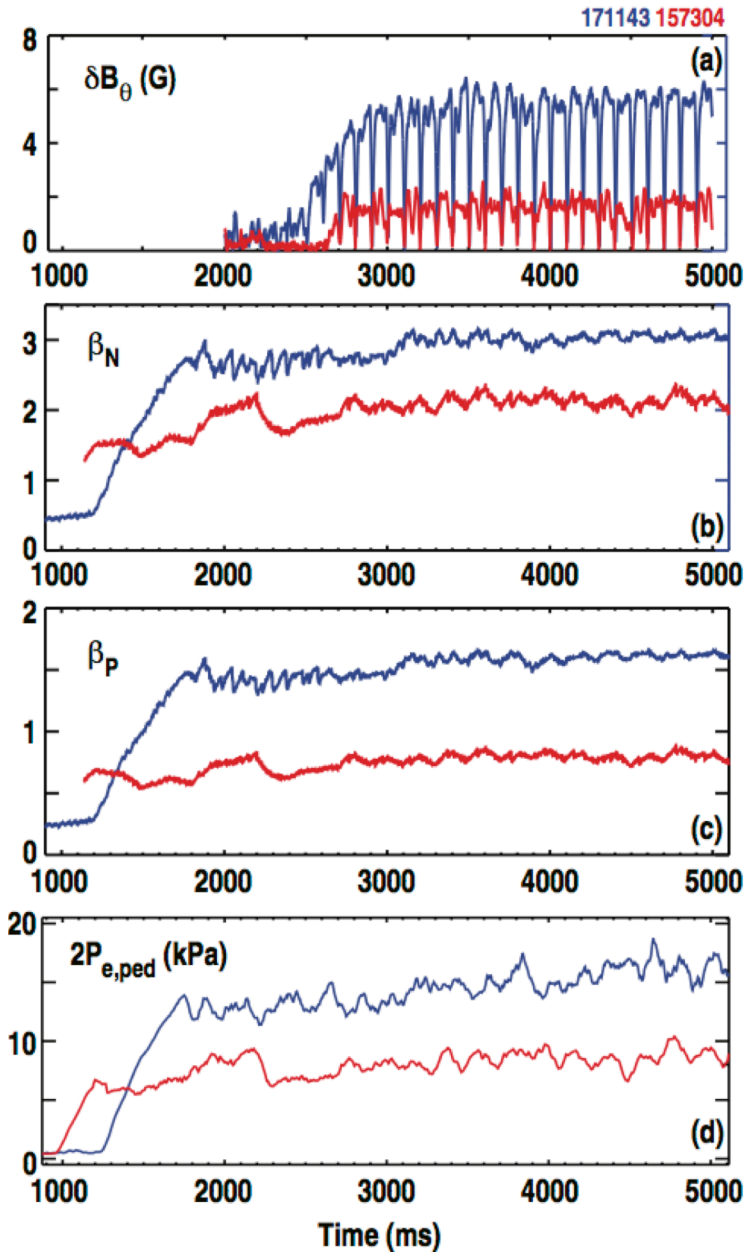


Figure 16. Plasma response for an RMP grassy-ELM plasma (#171143, blue) and ELM suppressed ITER baseline plasma on DIII-D (#157304, red): (a) Poloidal field amplitude measured on outer midplane probes, (b) normalized beta β_N , (c) poloidal beta β_P , and (d) twice the electron pedestal pressure $2P_{e,ped}$. Plasma parameters at flattop for #171143 (#157304) are: $R \approx 1.69$ m (1.69 m), $a \approx 0.59$ m (0.59 m), $B_T \approx -1.95$ T (-1.90 T), $I_p \approx 1.13$ MA (1.55 MA), $P_{NBI} \approx 9$ MW (6 MW), $P_{ECH} \approx 3.4$ MW (0 MW), $q_{95} \approx 5.3$ (3.5), $\beta_N \approx 2.95$ (2.12), $\beta_P \approx 1.53$ (0.78), $n_{e,ped} = 2.8 \times 10^{19}/\text{m}^3$ ($2.5 \times 10^{19}/\text{m}^3$), $T_{e,ped} = 1.8$ keV, (1.1 keV).

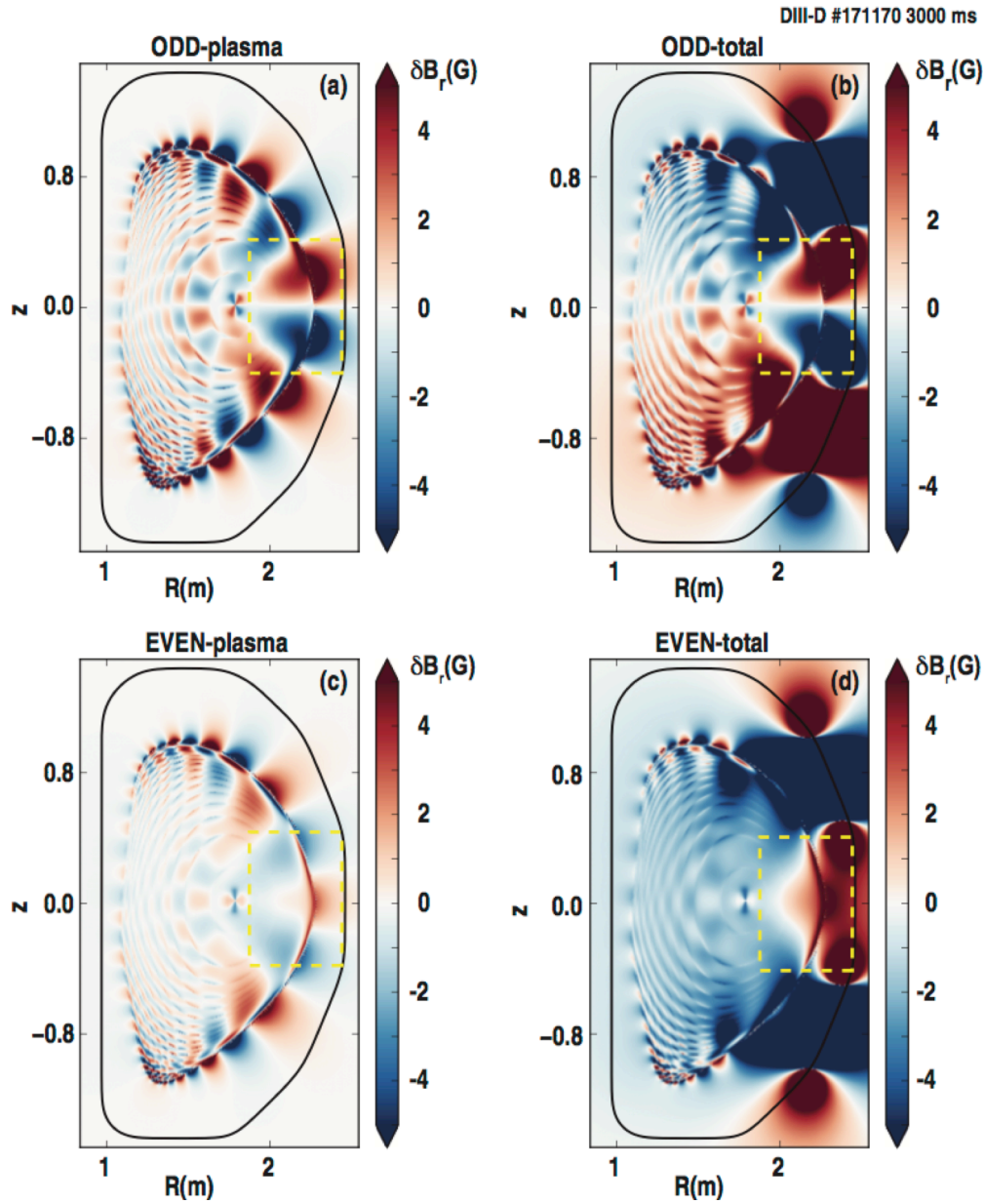


Figure 17. Radial magnetic perturbation calculated using GPEC for discharge #171170 at 3000 ms and using 1 kA I-coil current. (a) Plasma response for odd-parity $n=3$ RMP, (b) total radial field including plasma response and vacuum field for odd-parity, (c) even-parity plasma response, and (d) total field for even parity. The fringe field of the I-coils is indicated in the yellow dashed box in (b) and (d). The plasma parameters are similar to those for discharge #171143 in Fig. 16.

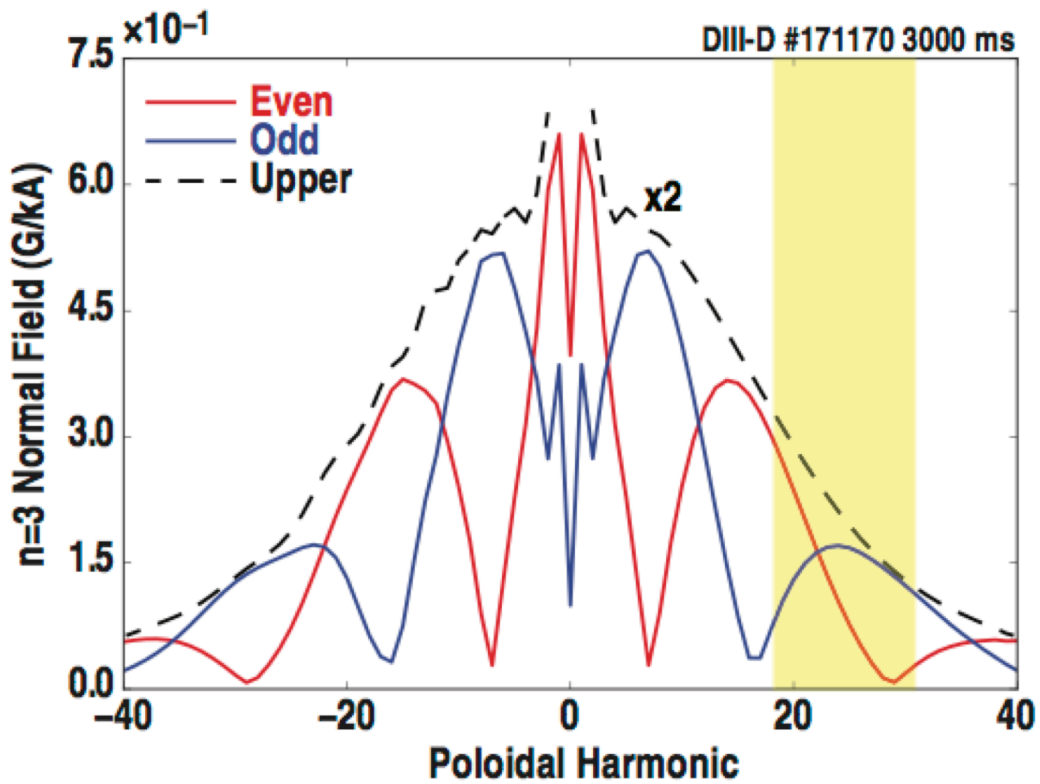


Figure 18. Poloidal spectrum of the radial vacuum field on the plasma surface using PEST angle coordinates for $n=3$ with 1 kA even-parity (red), 1 kA odd-parity (blue) and 2 kA in the upper row of I-coils (black dashed). The poloidal spectrum of the plasma response resides in the yellow shaded region.

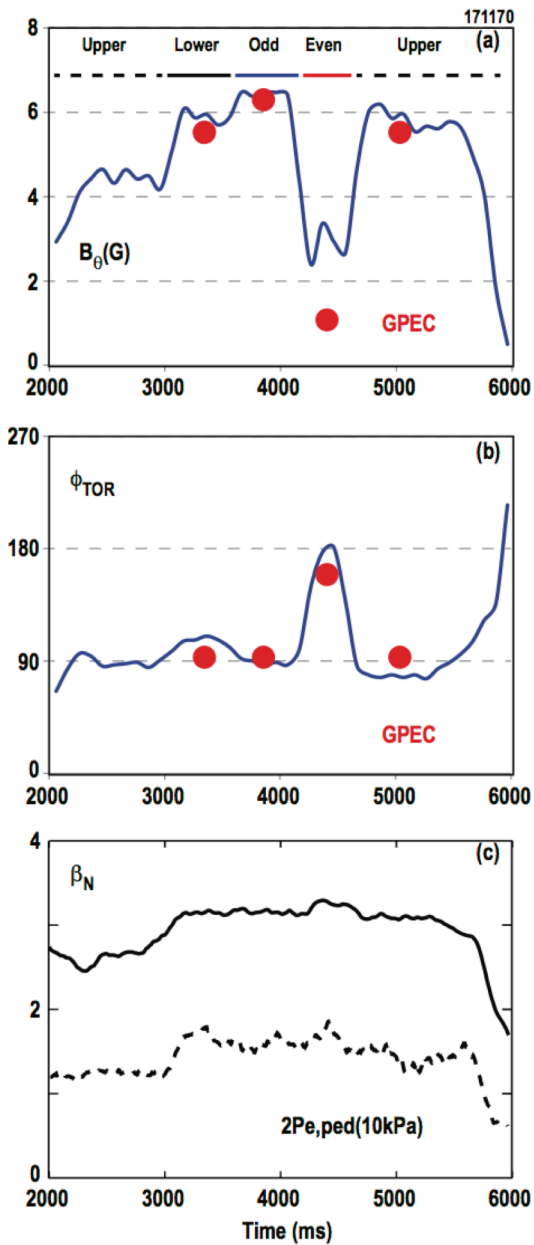


Figure 19. Plasma response vs. time measured on the outboard midplane sensors: (a) poloidal field amplitude (blue) for different coil configurations (upper only, lower only, odd parity and even parity) and the calculated GPEC response (red circles), (b) toroidal phase of the measured plasma response (blue) and GPEC phase (red), and (c) normalized beta (blue) and pedestal electron pressure (red). The GPEC calculations are based on one kinetic EFIT equilibrium evaluated from the profile data at $t=3400$ ms. Plasma parameters for #171170 are similar to discharge #171143 in Fig. 16.

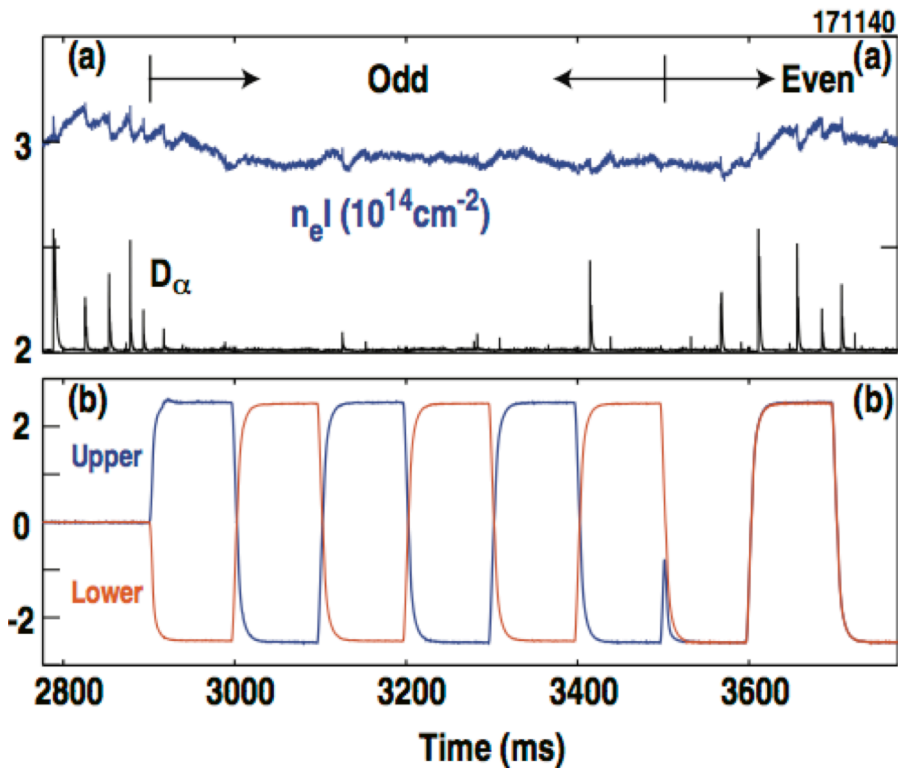


Figure 20. Plasma response to I-coil parity for discharge #171140: (a) line density (blue) and D_α (black), (b) upper and lower I-coil current. Odd parity is on from 2900 – 3500 ms. Even parity is from 3500 ms. The plasma parameters are similar to discharge #171143 in Fig. 16.

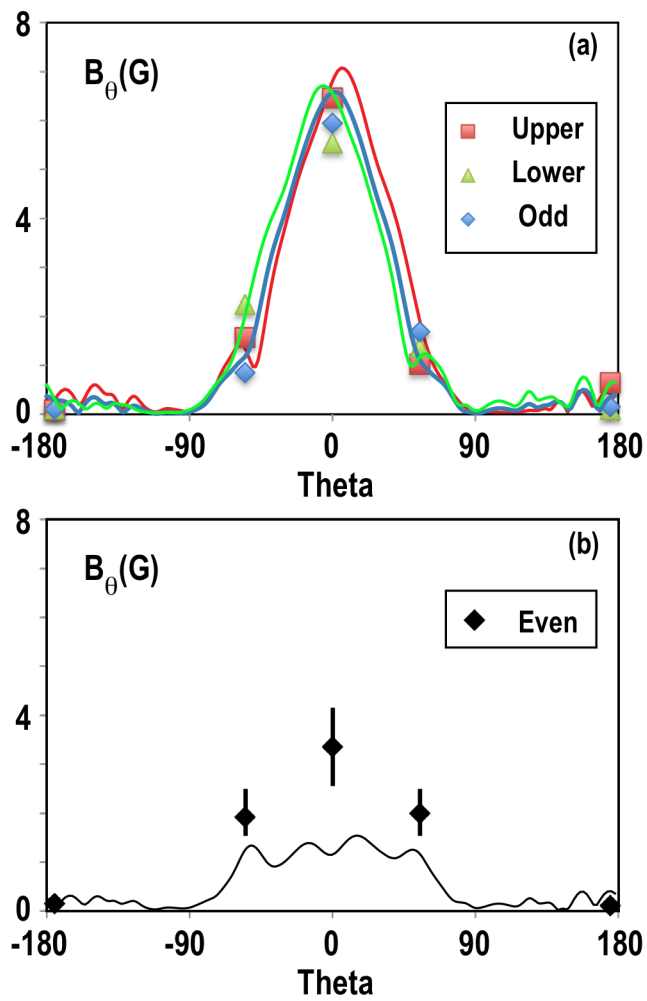


Figure 21. Poloidal field amplitude for applied $n=3$ field measured on five toroidal magnetic coil arrays distributed poloidally as shown in Fig. 2. The GPEC calculated plasma response is shown in solid lines for (a) the $n=3$ upper row (4.5 kA), the $n=3$ lower row (4.5 kA), odd-parity (2.5 kA), and (b) even parity (2.5 kA).

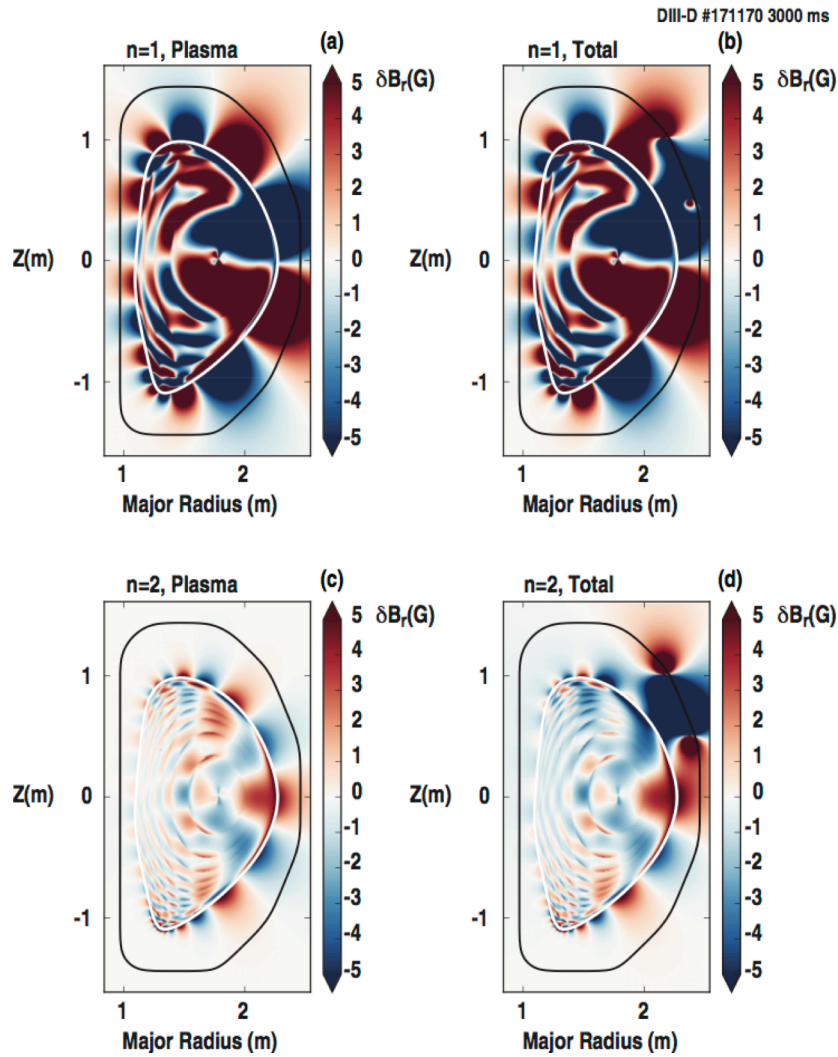


Figure 22. A 1 kA current in the upper row of I-coils used as a proxy for $n=1$ and $n=2$ error field using the same equilibrium in Fig. 17. The plasma response (a) and total field (b) for an $n=1$ perturbation, and the plasma response (c) and total response (d) for an $n=2$ perturbation. The amplification of the $n=1$ proxy for the error field is 10x higher than for the $n=2$ field for the same I-coil current.

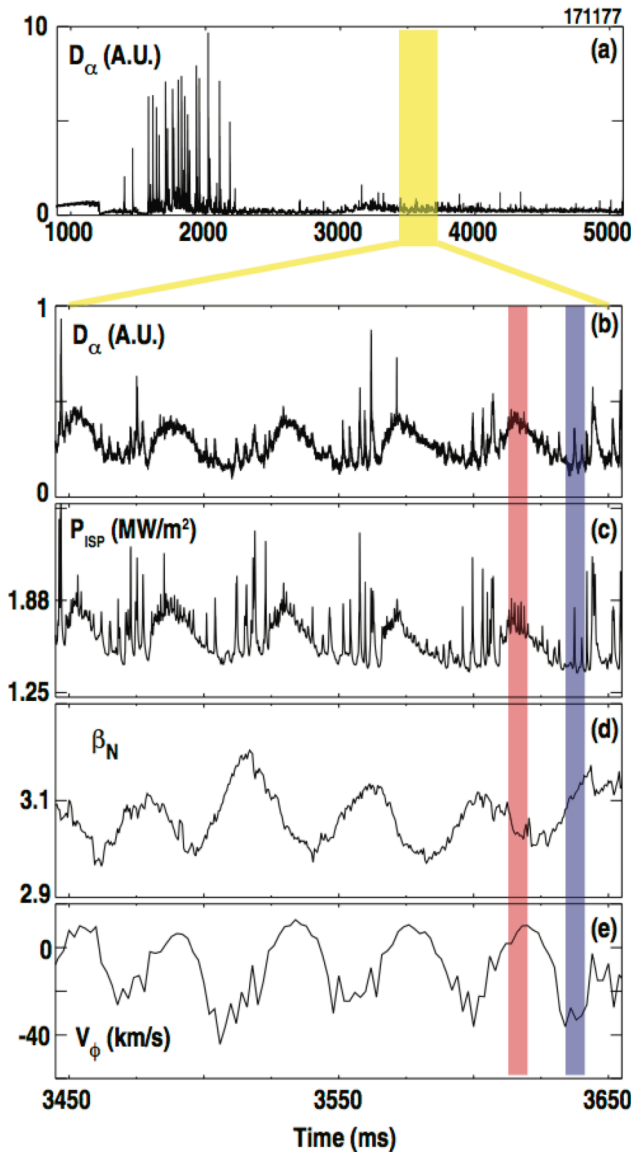


Figure 23. Pulsations in the plasma edge for shot #171177 with $n=3$ 4.5 kA current in the upper I-coils. The blue band corresponds to the peak of the grassy-ELM phase and red band corresponds to the mitigated grassy-ELM phase: (a) Balmer alpha (D_α) emission from the inner strike point, and a zoom view of (b) D_α , (c) P_{ISP} , (d) β_N , and (e) toroidal rotation velocity at $\psi_N \approx 0.92$. Plasma parameters at the time of interest are: $q_{95} \approx 5.3$, $\beta_N \approx 3.1$, $\beta_p \approx 1.60$, $R \approx 1.68$ m, $a \approx 0.6$ m, $B_T \approx -1.90$ T, $I_p \approx 1.15$ MA, $P_{NBI} \approx 10$ MW, $P_{ECH} \approx 3.4$ MW, stored energy $W_{dia} \approx 1.2$ MJ, pedestal pressure $P_{ped} \approx 18$ kPa, pedestal density $n_{e,ped} \approx 3.1 \times 10^{19} \text{ m}^{-3}$ and pedestal temperature $T_{e,ped} \approx 1.6$ keV.

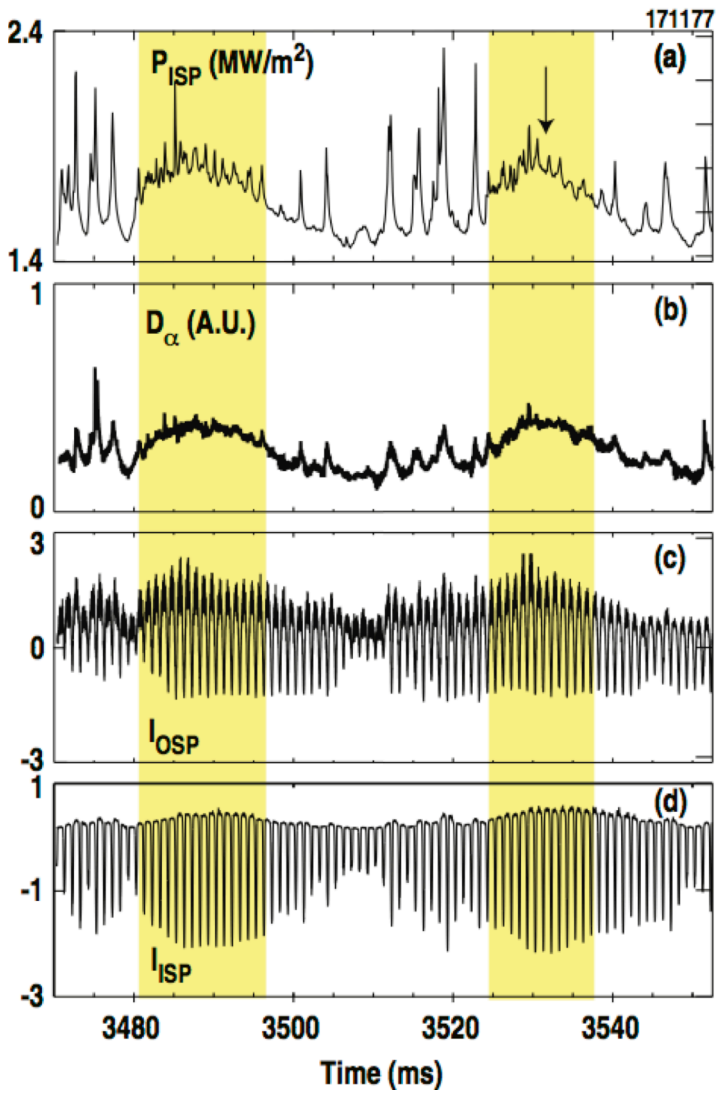


Figure 24. Pulsations in the plasma edge for shot #171177 with $n=3$ 4.5 kA current in the upper I-coils: (a) peak heat flux to the inner strike region, (b) Balmer light from the inner strike, (c) Langmuir probe current during voltage sweep near outer strike point, and (d) Langmuir probe current near inner strike point. Yellow bands indicate periods of mitigated grassy-ELMs.

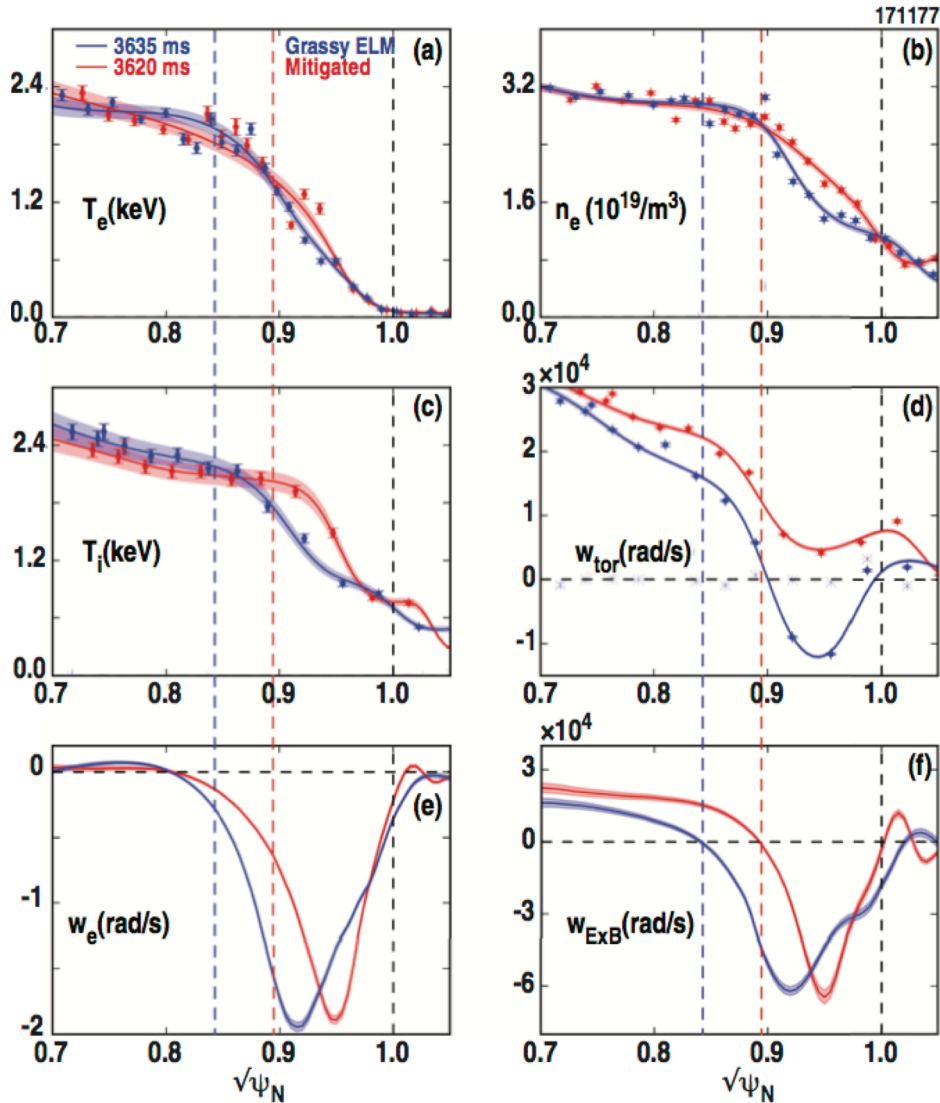


Figure 25. Plasma edge profiles for the pulsations in Fig. 23. The profiles are taken at $t=3620$ ms during the maximum of the edge toroidal rotation (blue) and at $t=3635$ ms at the minimum of the edge rotation during the grassy-ELMs. Shown are (a) electron temperature, (b) electron density, (c) ion temperature, (d) toroidal rotation velocity, (e) electron perpendicular frequency, and (f) ExB frequency. The blue/red/black dashed lines correspond to the $q=4$, $14/3$ and separatrix locations, respectively.

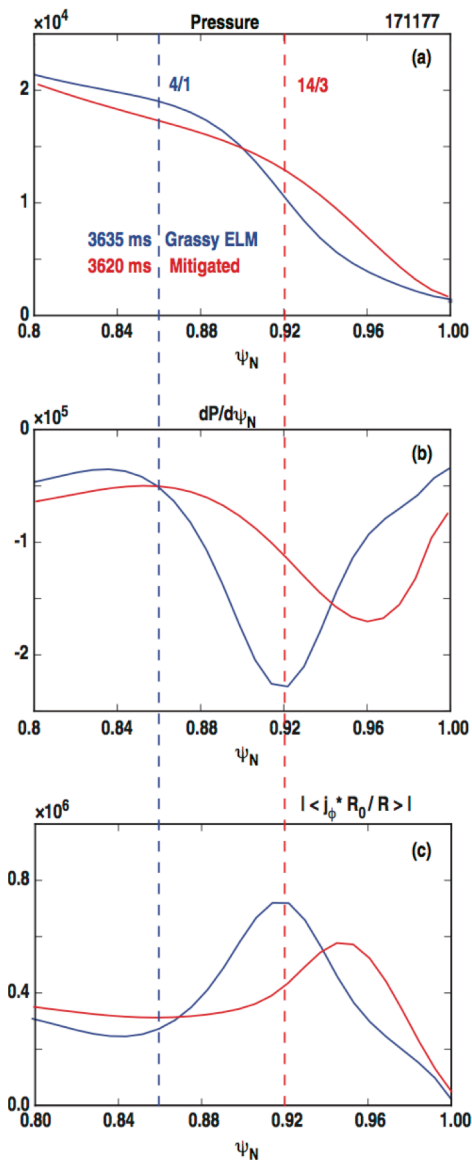


Figure 26. Kinetic equilibrium profiles vs. ψ_N for the pulsating pedestal at 3620 ms (red for the grassy-ELM mitigated phase) and 3635 ms (blue at the peak of the grassy-ELM activity). The blue/red dashed lines indicate the location of the $q=4$ and $q=14/3$ rational surfaces respectively. Shown are (a) the total plasma pressure, (b) the total pressure gradient, and (c) the edge current using the Sauter model.

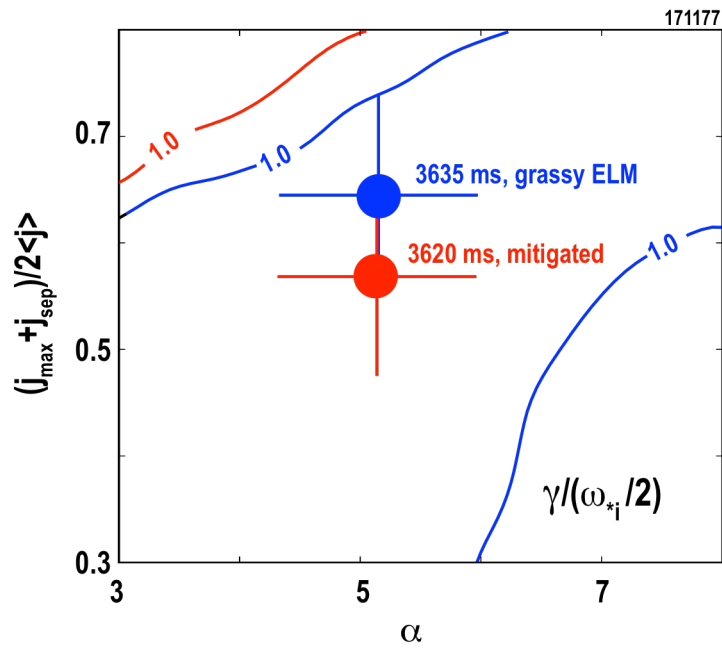


Figure 27. Peeling-Ballooning stability using the ELITE code for the grassy-ELM mitigated phase at 3620 ms (red) and the strong grassy-ELM phase (blue) at 3635 ms. The stability boundary for the grassy-ELM mitigated phase is indicated by the red line and the stability boundary for the strong grassy-ELM phase by the blue line. The strong grassy-ELM phase is closer to the low- n peeling ballooning stability boundary than the mitigated phase.

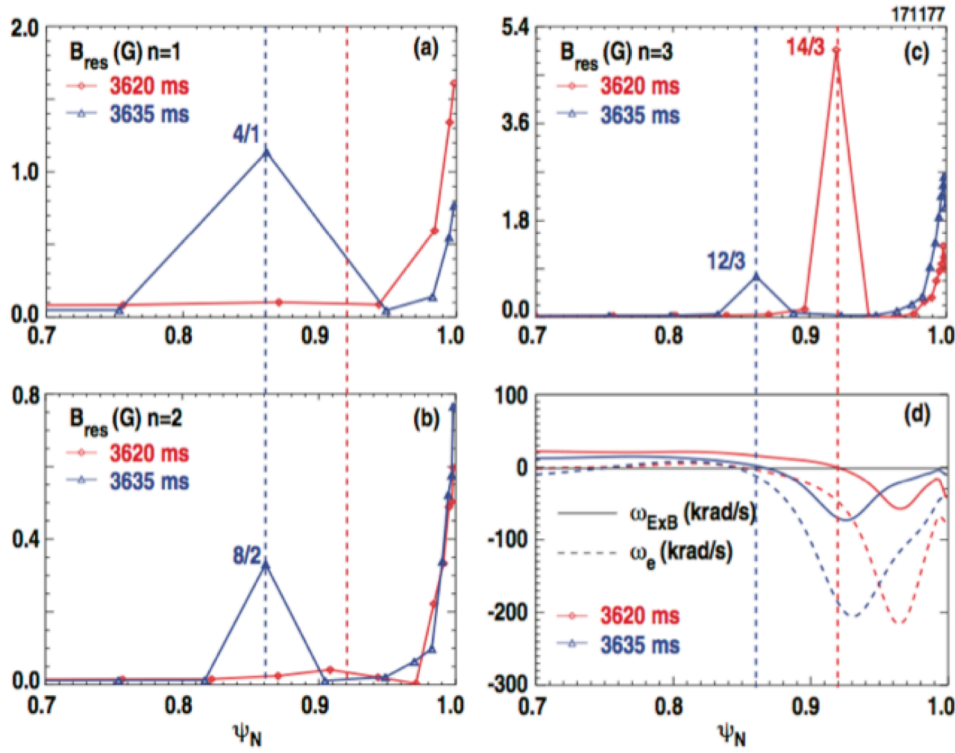


Figure 28. Linear single fluid M3D-C¹ calculation of the resonant radial field during the strong grassy-ELM phase at 3635ms (blue) and the grassy-ELM mitigated phase at 3620 ms (red): (a) $n=1$ with 1 kA in the upper I-coil, (b) $n=2$ with 1 kA in the upper I-coil, (c) $n=3$ with 4.5 kA in the upper I-coil, and (d) the ExB frequency ω_{ExB} and the electron perpendicular rotation frequency ω_e . Vertical dashed lines correspond to the $q=4$ rational surface (blue) and the $q=14/3$ rational surface (red).

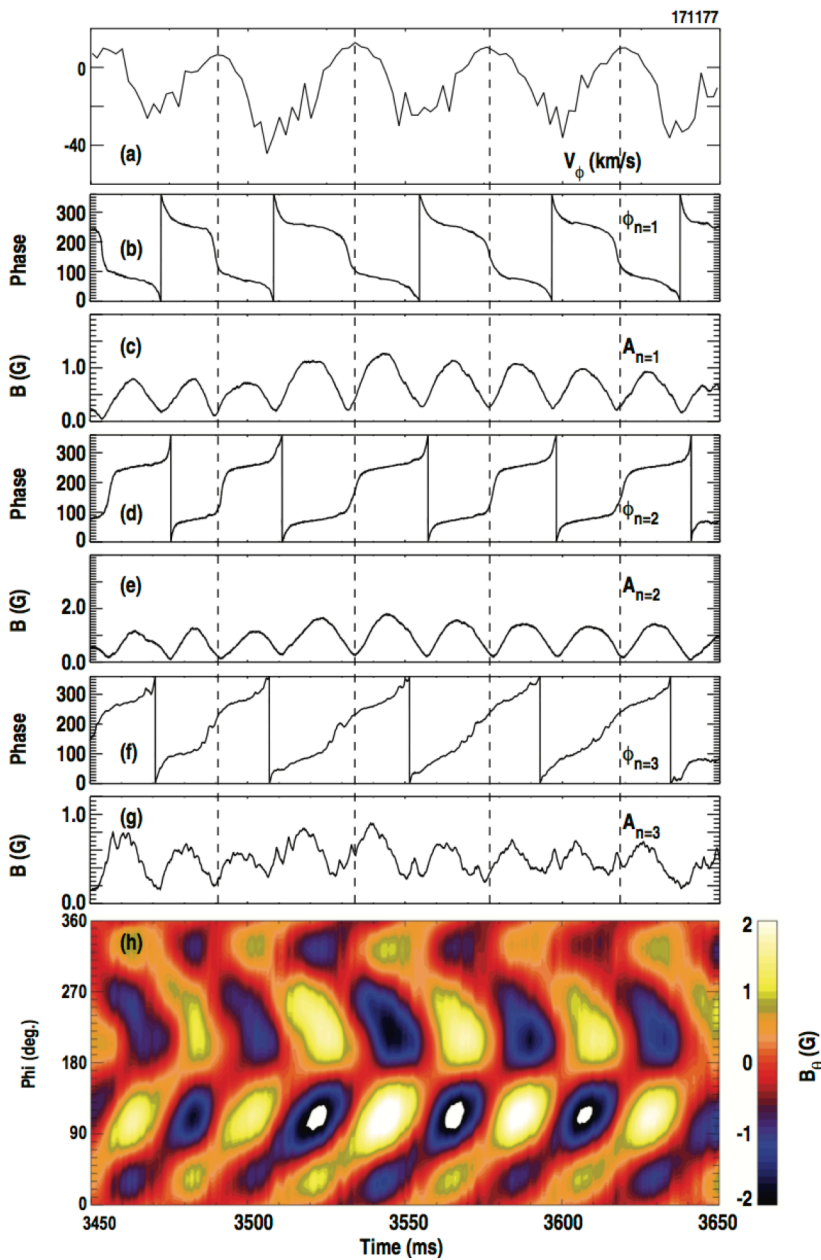


Figure 29. Poloidal magnetic field pulsations measured on the outer midplane: (a) Toroidal rotation velocity at $\psi_N \approx 0.92$ with dashed lines indicating times during mitigated grassy-ELMs, (b) phase and (c) amplitude of the $n=1$ response, (d) phase and (e) amplitude of the $n=2$ response, (f) phase and (g) amplitude of the $n=3$ response, and (h) the poloidal field vs. toroidal angle and time. A 100 ms moving average subtraction is applied to the magnetic signals. Thus the static $n=3$ plasma response has been removed.

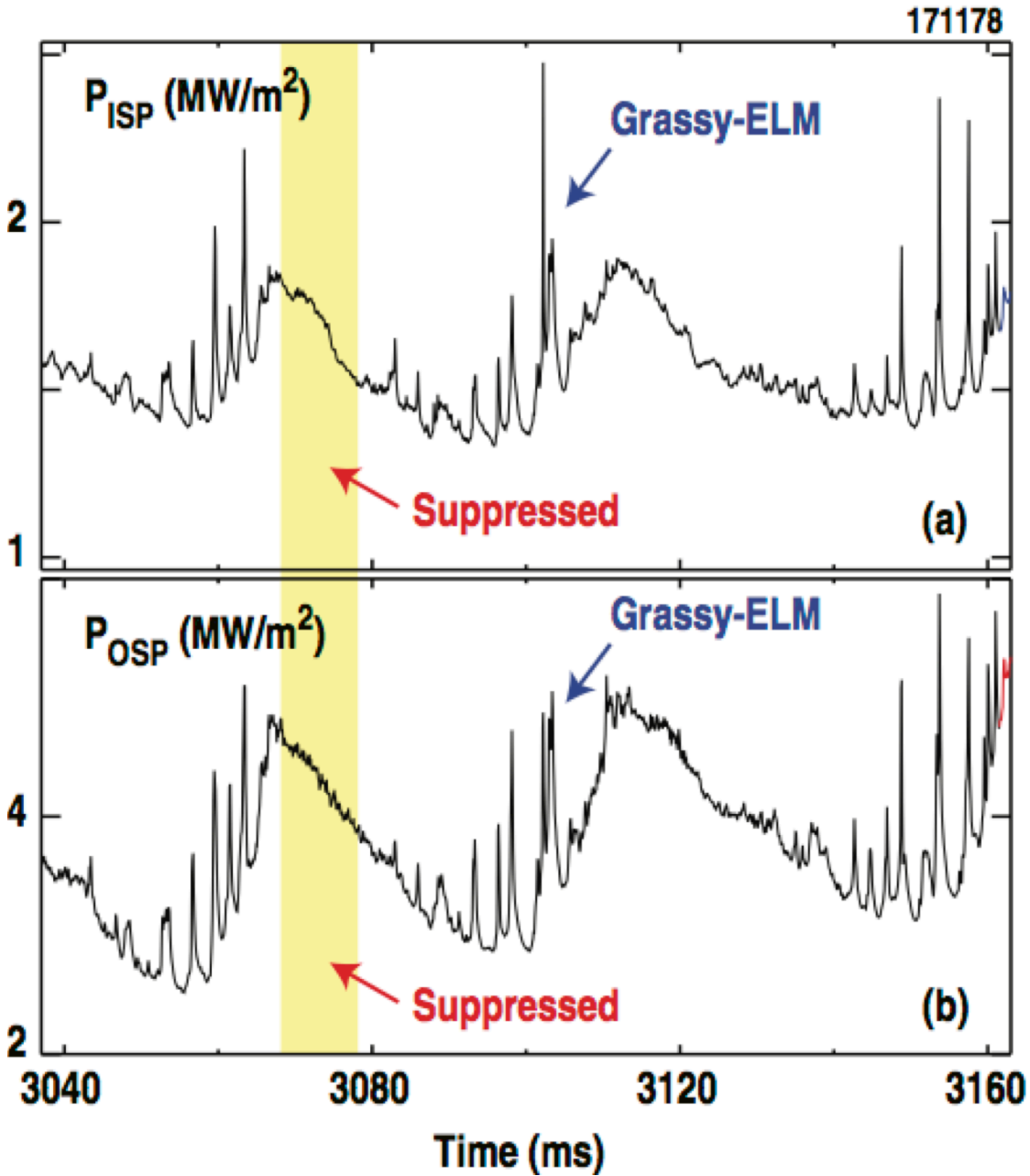


Figure 30. A pulsating grassy-ELM discharge with 2.5 kA $n=3$ odd-parity RMP. IR camera measurements of the peak heat flux at (a) inner strike location, and (b) the outer strike location. The grassy-ELMs are suppressed in the period identified by the yellow band. Plasma parameters at the time of interest are: $q_{95} \approx 5.3$, $\beta_N \approx 3.0$, $\beta_p \approx 1.55$, $R \approx 1.68$ m, $a \approx 0.6$ m, $B_T \approx -1.90$ T, $I_p \approx 1.15$ MA, $P_{\text{NBI}} \approx 10$ MW, $P_{\text{ECH}} \approx 3.4$ MW, stored energy $W_{\text{dia}} \approx 1.2$ MJ, pedestal pressure $P_{\text{ped}} \approx 15$ kPa, and pedestal density $n_{e,\text{ped}} \approx 3.1 \times 10^{19} \text{ m}^{-3}$.

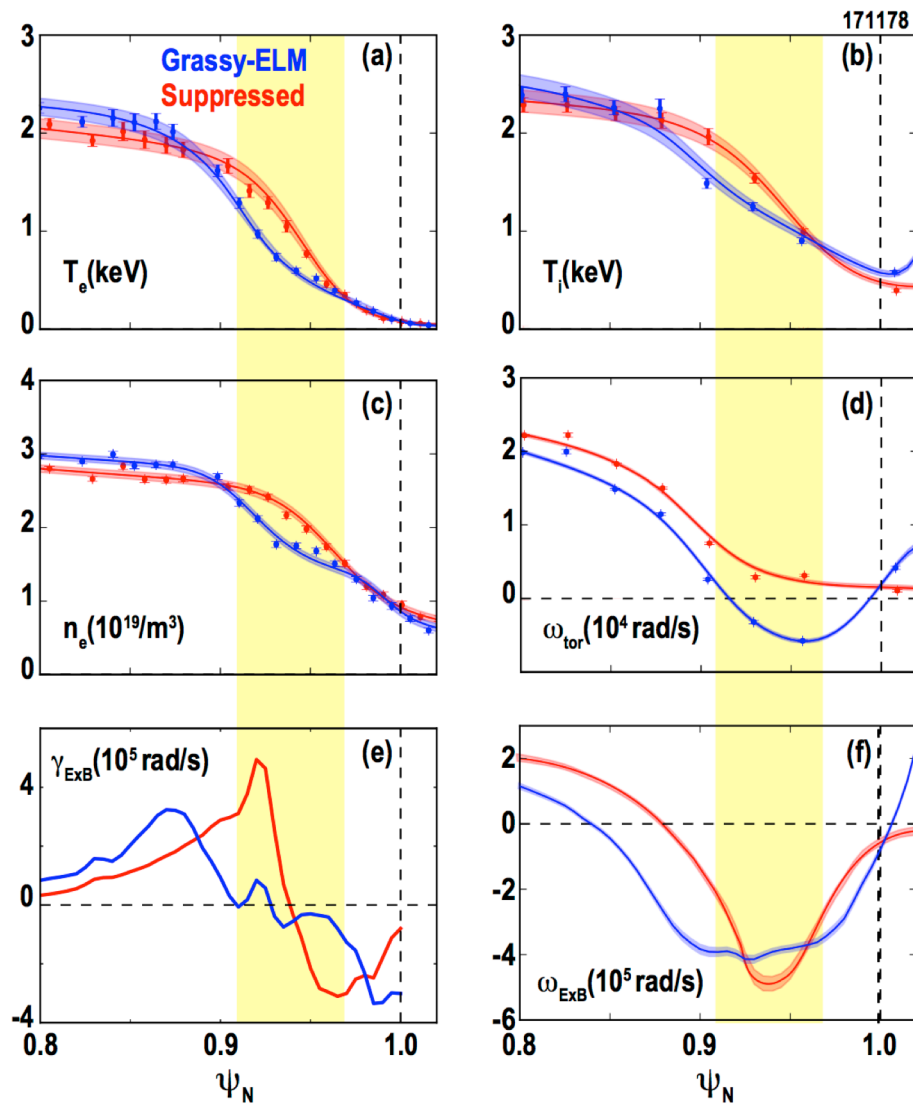


Figure 31. Ensemble average of Thomson and CER measurements over ten consecutive pedestal pulsations from 3590 – 4310 ms during grassy-ELM mitigation (red) and regular grassy-ELMs (blue) in discharge #171178 with 4.5 kA $n=3$ upper I-coils: (a) electron temperature T_e , (b) ion temperature T_i , (c) electron density n_e , (d) toroidal rotation frequency ω_{tor} , (e) ExB shearing rate γ_{ExB} , (f) ExB frequency ω_{ExB} .

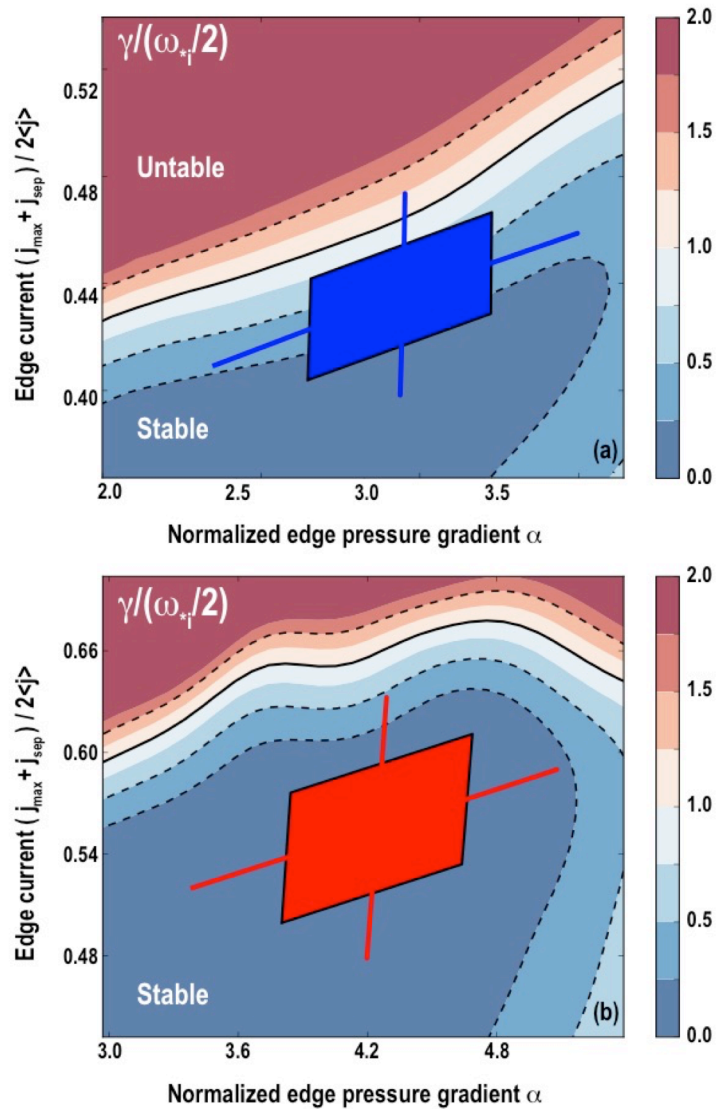


Figure 32. Peeling-ballooning mode stability analysis with the ELITE code for the profiles in Fig. 31: (a) grassy-ELM phase (blue profiles in Fig. 31), and (b) grassy-ELM suppressed phase (red profiles in Fig. 31). Solid contour correspond to the threshold for PBM onset, rectangle region and cross hairs correspond to a 10% and 20% uncertainty in the experimentally inferred average edge pressure gradient and edge current.

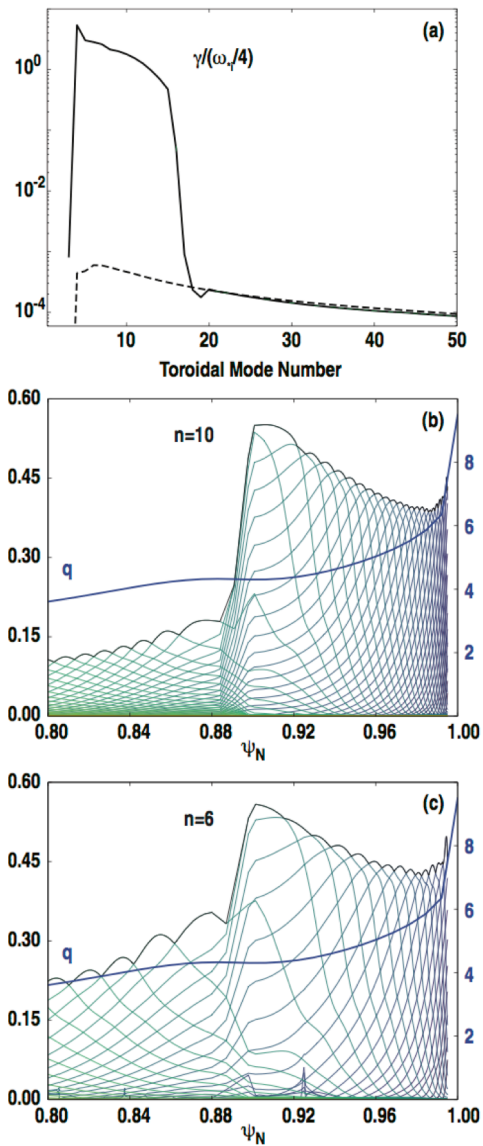


Figure 33. ELITE calculation of the peeling-ballooning-mode spectrum for the grassy-ELM phase of the discharge in Fig. 31: (a) Linear growth rate vs. toroidal mode number for the experimental profile (dashed curve corresponding to the blue profile in Fig. 31) and for a near by unstable profile (solid line), (b) radial eigenmode on the $n=10$ unstable mode and q -profile showing shear reversal, and (c) radial eigenmode of the $n=6$ unstable mode and q -profile.

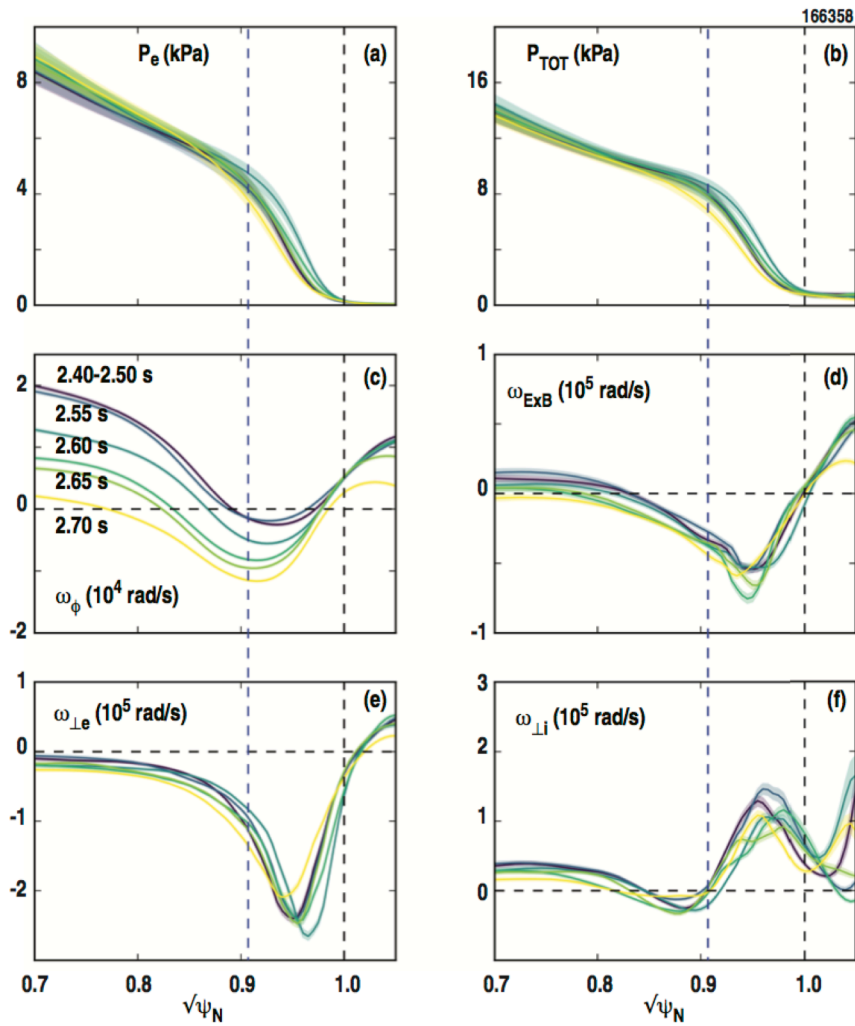


Figure 34. Edge profiles in discharge #166358 taken during the beam torque ramp from 2.4 – 2.7 s in Fig. 6: (a) electron pressure P_e , (b) total pressure P_{TOT} , (c) toroidal rotation frequency ω_ϕ , (d) ExB frequency ω_{ExB} , (e) electron perpendicular flow frequency $\omega_{\perp e}$, and (f) ion perpendicular flow frequency $\omega_{\perp i}$. Vertical dashed lines indicate top of pedestal and separatrix location.

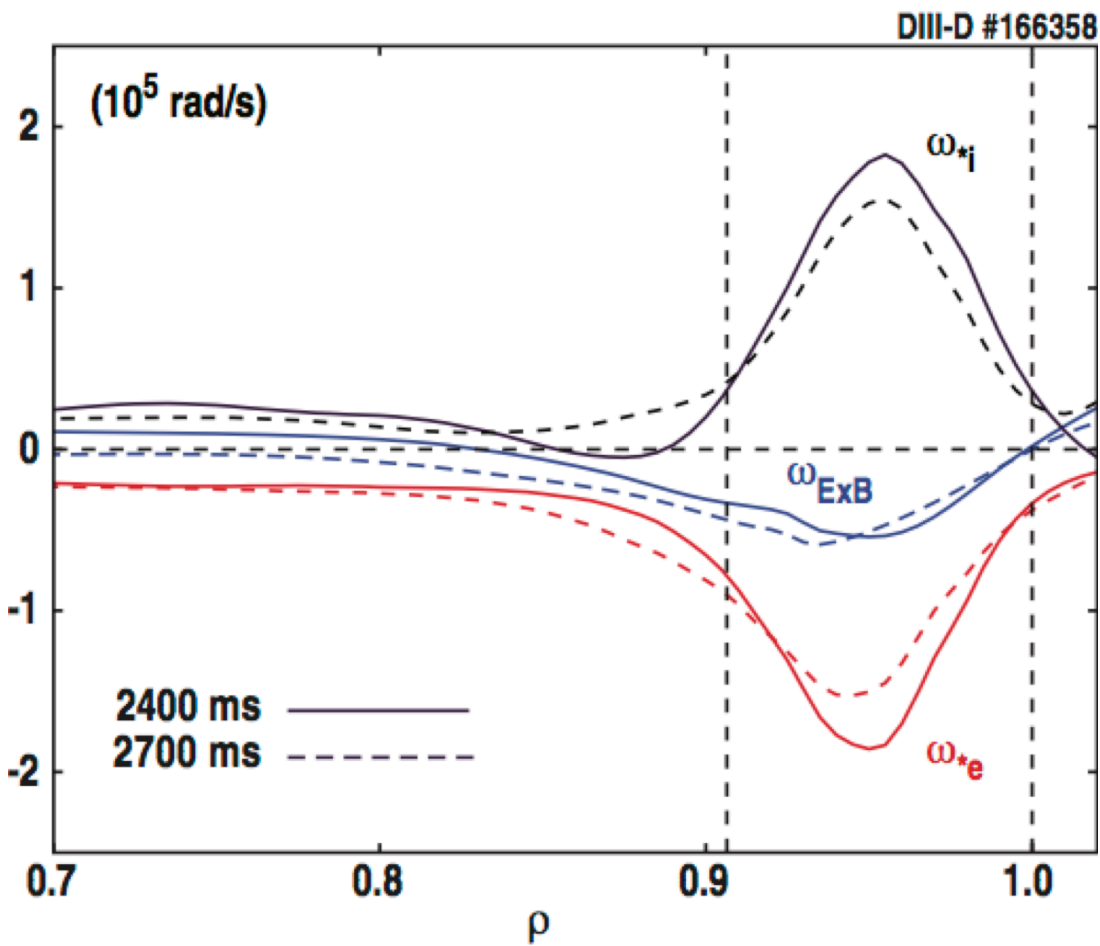


Figure 35. Electron flow, ion flow and ExB flow frequency for discharge #166358 taken before the torque step down at ≈ 2400 ms (solid lines) and after the step down at ≈ 2700 ms (dashed). Shown are the ion diamagnetic frequency (black), the electron diamagnetic frequency (red) and the ExB frequency (blue) in radians/sec. Top of pedestal location is indicated by vertical dashed line near $\sqrt{\psi_N} = 0.9$.